MINIMALIST THEORY FOR MESOSCALE REACTION DYNAMICS

A Thesis
Presented to
The Academic Faculty

by

Galen Thomas Craven

In Partial Fulfillment
of the Requirements for the Degree
Doctor of Philosophy in the
School of Chemistry and Biochemistry

Georgia Institute of Technology
December, 2014

MINIMALIST THEORY FOR MESOSCALE REACTION DYNAMICS

Approved by:

Dr. Rigoberto Hernandez, Advisor
School of Chemistry and Biochemistry
Georgia Institute of Technology

Dr. Angelo Bongiorno
School of Chemistry and Biochemistry
Georgia Institute of Technology

Dr. Jean-Luc Brédas
Division of Physical Sciences and Engineering
King Abdullah University of Science and Technology

Dr. Thomas Orlando
School of Chemistry and Biochemistry
Georgia Institute of Technology

Dr. Turgay Uzer
School of Physics
Georgia Institute of Technology

Date Approved: November 5th, 2014

To Ginny, Mer, and Nanny

ACKNOWLEDGEMENTS

First and foremost, I would like to thank Ginny for her love and support in the process leading to this dissertation. I am also deeply grateful for the undying love of my mother and grandmother. Thank you to all my friends and family, especially my brother, Sandy. I have been fortunate to work with many scholars during this project, and I would especially like to thank my advisor, Dr. Rigoberto Hernandez, for his invaluable guidance and for allowing me to explore research areas that interested me. My thanks to Dr. Alex Popov and to Dr. Thomas Bartsch, both of whom provided key ideas leading to the results presented in this dissertation. Thank you to the members of my doctoral committee — Dr. Angelo Bongiorno, Dr. Jean-Luc Brédas, Dr. Thomas Orlando, and Dr. Turgay Uzer — for taking the time to critique my work. I owe deep gratitude to Dr. Michael Moeller, my mentor at the University of North Alabama, and to Dr. Valeriy Dolmatov, for the valuable research experience they provided me. Finally, I would like to thank my peers and colleagues in the Hernandez group at Georgia Tech.

TABLE OF CONTENTS

LIST OF FIGURES

SUMMARY

The prediction of an atomistic system's macroscopic observables from microscopic physical characteristics is often intractable, either by theory or computation, due to the intrinsic complexity of the underlying dynamical rules. This complexity can be simplified by identifying key mechanisms that drive behavior and considering the system in a reduced representation that captures these mechanisms. Through theory, this thesis examines complex relationships in structured assembly and reaction mechanisms that occur when effective interactions are applied to mesoscale structures. In the first part of this thesis, the structure and assembly of soft matter systems are characterized while varying the interpenetrability of the constituent particles. The nature of the underlying softness allows these systems to be packed at ever higher density, albeit with an increasing penalty in energy. Stochastic equations of motion are developed in which mesoscopic structures are mapped to single degrees of freedom through a coarse-graining procedure. The effective interactions between these coarse-grained sites are modeled using stochastic potentials that capture the spatial behavior observed in systems governed by deterministic bounded potentials. The second part of this thesis presents advancements in time-dependent transition state theory, focusing on chemical reactions that are induced by oscillatory external forces. The optimal dividing surface for a model driven reaction is constructed over a transition state trajectory. The stability of the transition state trajectory is found to directly dictate the reaction rate, and it is thus the fundamental and singular object needed to predict barrier-crossing rates in periodically driven chemical reactions. This thesis demonstrates that using minimalist models to examine these complex systems can provide valuable insight into the dynamical mechanisms that drive behavior.

CHAPTER I

INTRODUCTION

1.1 Motivation & Objectives

The phase and spatial behavior observed in the assembly of a monomeric species into oligomeric clusters [174, 38, 165, 57, 91, 153, 1] drives the design of materials with unique functions [58, 59, 66, 65]. At atomistic length scales, the structural complexity arising from assembly is often difficult to describe using analytical theory or to simulate on relevant time scales due to the large numbers of degrees of freedom that constitute such systems. To reduce this complexity, the atomistic degrees of freedom can be reduced to a coarse-grained (CG) description in which a group of atomic degrees of freedom is mapped onto a single CG site [125, 116, 34, 169, 142]. At mesoscopic length scales, CG macromolecules can be modeled using repulsive potentials that are finite valued at the origin, *i.e.*, bounded potentials [111, 136]. As shown in Fig. 1, the finite nature of bounded interactions allows for multiple macromolecules to overlap and occupy the same volume in configuration space [173, 110], giving rise to structural configurations that differ from those of all-atom representations. Studies of mesoscopic systems with interactions dictated by bounded potentials include colloid suspensions [61], polymer-colloid mixtures [170], star polymers [145], and block copolymers [201, 202]. The goal of the first part of this thesis is to elucidate the structural properties of soft, mesoscopic structures in order to understand and control assembly processes.

The second part of this thesis examines invariant phase space structures in driven reaction mechanisms in order to understand stimuli-responsive reactions. Materials that change shape and functionality in response to an external trigger form the constituent components of molecular machines [18, 88, 6, 130, 128]. Stimuli such as thermal variations, pH changes, electric fields, and photoinduction have been used as triggers for the conversion of chemical energy into mechanical work [49, 106, 52]. In these responsive materials, controlling the rate

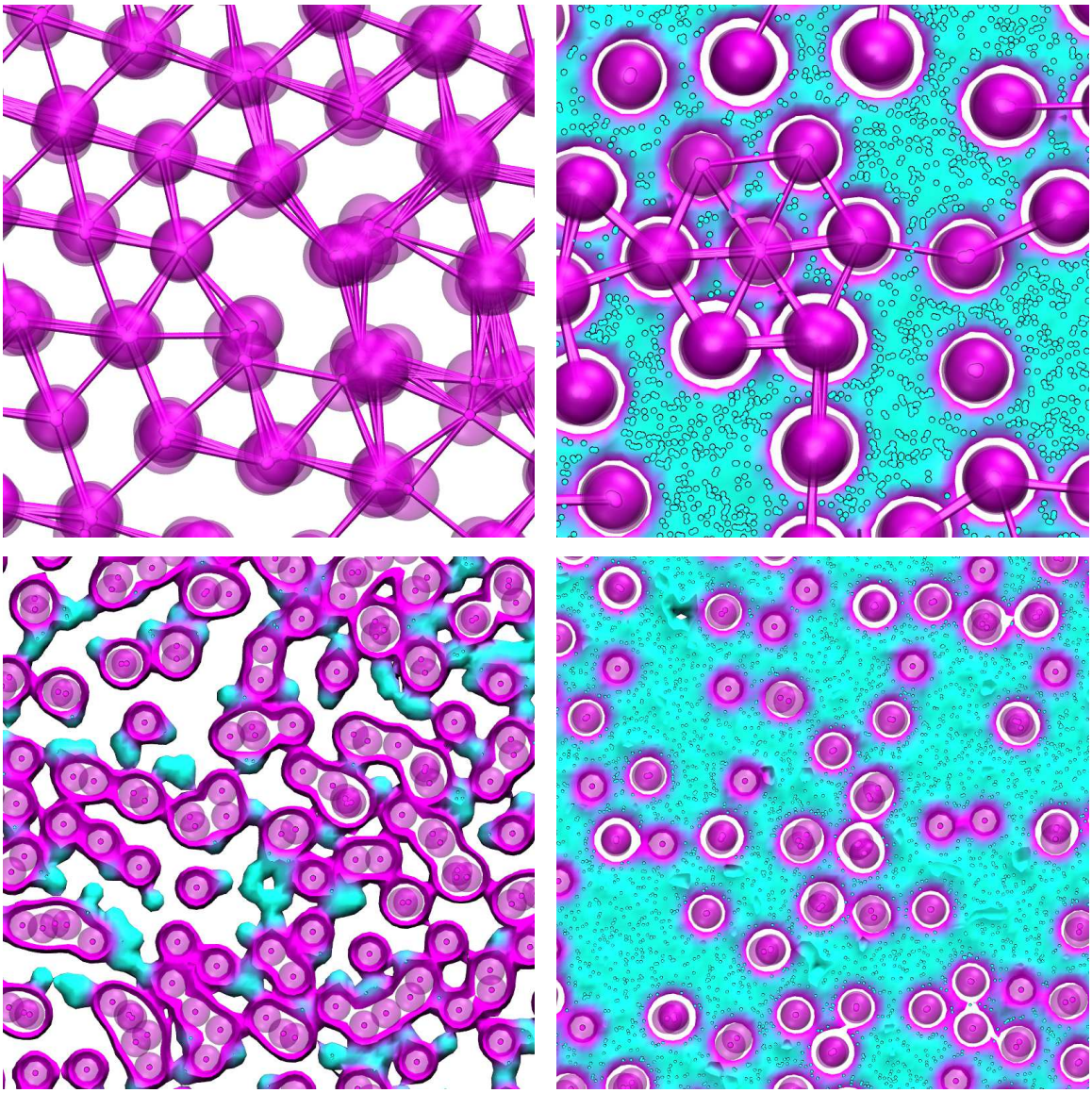

Figure 1: Selected spatial configurations of systems of particles whose dynamics are governed by soft bounded potentials. The purple structures are coarse-grained macromolecules and the surrounding solvent environment is colored in cyan. In the top panels, bonds connect the centers of mass of neighboring macromolecules.

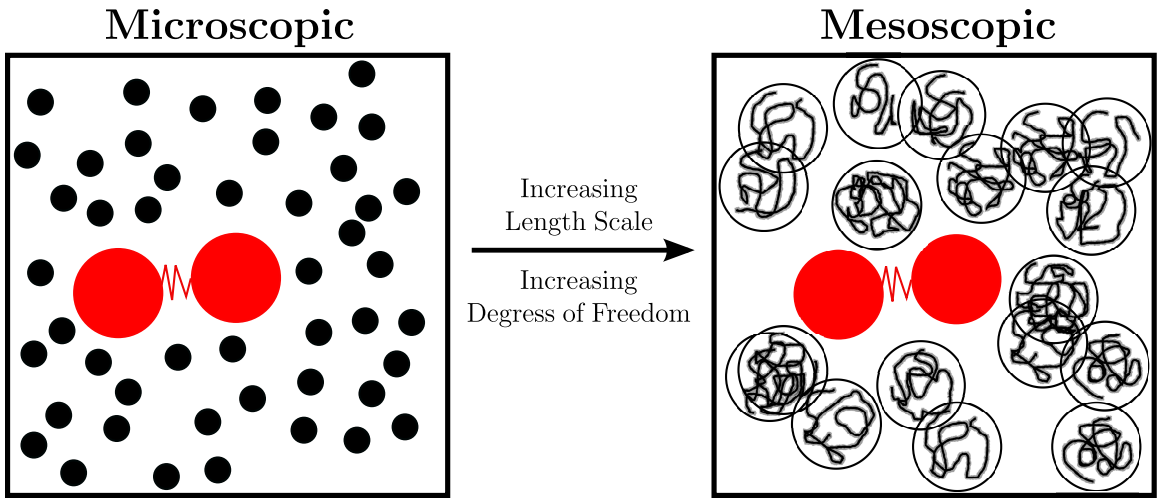

Figure 2: A molecular structure (red) undergoing a configurational change in a microscopic solvent (left) and a mesoscopic solvent (right).

at which reactants transform to products, either to accelerate a process or to bias a reaction toward a certain pathway, is fundamental to harness mechanical actions for use in nanotechnology. Such kinetic control can be achieved through forcing from an external field, leading to emergent behavior in molecular structure assembly [42, 80, 156, 117, 163, 130]. Because soft interactions allow macromolecules to overlap, the geometric properties of microscopic reaction environments differ from mesoscopic environments, as shown in Fig. 2.

Assemblies that convert chemical energy into rotational motion are perhaps the simplest conceptual examples of such devices. Unidirectional motion achieved through isomerization reactions can be induced from either light or applied electric fields [75, 93, 163, 209]. These devices encompass a class of responsive materials called molecular rotors. Thermal fluctuations are inherent in microscopic machinery [6], differentiating the atomistic length scale from the effectiveness of macroscopic machines. Immobilization of molecular rotors on surfaces [75], both in the solid state [55, 89] and through extension to mesoscale devices, have advanced molecular machines toward deterministically directed regimes [75, 197, 18, 26].

In these directed processes, reaction rates can be obtained through transition state theory (TST) [133, 191, 72]. There are two major obstacles to the implementation of TST. First, reactive trajectories must be identified, and, second, the flux of these reactive

trajectories though a dividing surface (DS) must be calculated. If this DS is recrossed by reactive trajectories, TST overestimates the rate. Only in cases in which this DS is recrossing-free is TST formally exact. However, cases in which a recrossing-free DS can be constructed are rare, and thus approximation techniques, such as variational transition state theory [188, 76, 148, 190, 152, 138], must be employed.

The development of rate theories is of particular interest to chemical physics in which the determination of rates is a central concern, and it is increasingly necessary for rates to be determined in systems that are driven far from equilibrium. Specifically, the response of a chemical constituent to the external forcing by oscillating fields can strongly influence the mechanism and rate in which a reactant is transformed to product.

In an autonomous system with two degrees of freedom, Pechukas and Pollak have shown that the optimal dividing surface is an unstable periodic orbit (PO) [150, 151, 146, 149]. Its projection into configuration space provides a dividing surface that is locally recrossing free. In systems with three or more degrees of freedom, this periodic orbit is generalized to a normally hyperbolic invariant manifold (NHIM) [35, 73, 71, 193, 72, 2, 107, 199, 78]. Attached to the NHIM are stable and unstable manifolds. These manifolds form phase space separatrices that distinguish between reactive and nonreactive trajectories and also constitute the pathways by which reactive trajectories are funneled from reactant to product through the TS [193, 2, 78]. The principal motivation for the second part of this thesis is the construction of a structure that persists even when a chemical reaction is driven by an external oscillating field, such as an electric field [86, 87].

1.2 Thesis Structure

In Chapters 2 through 4, the structural and dynamical properties of a system of isotropic penetrable particles are discussed. In Chapter 2, which is adapted from published work in Refs. [30] and [31] co-authored with Dr. Alex Popov and Dr. Rigoberto Hernandez, a method is developed to simulate soft matter systems by treating interparticle interactions as stochastic events. The treatment of such systems is of broad interest because it concerns any problem in which the nature of soft matter interactions between particles drives the

structure and dynamics of the assembly. The simplicity of our model allows us to vary the soft potential across the limits of a hard nonpenetrable potential and a noninteracting (ideal) potential. Using analytic theory and dynamical simulations, we study the spatial properties and phase behavior of stochastically penetrable spheres over varying dimensions. By treating interparticle interactions as stochastic events, we mimic the interactions of deterministic potentials used to model coarse-grained macromolecules at mesoscopic length scales. When the spheres are allowed to interpenetrate due to the stochastic nature of the governing potentials, we observe emergent structural transitions that are varied through the softness of the underlying stochastic interactions. A method is developed for determining the occupied volume fraction of penetrable soft matter systems that improves on earlier methods by several groups. Specifically, we find that the occupied volume fraction and anomalous clustering can all be accessed by a hard-particle model augmented only with a single pairwise parameter that is characteristic of the overlap probability.

A further investigation of the spatial properties of cluster-forming soft particles is presented in Chapter 3. We study the sequential adsorption of coarse-grained macromolecules binding to a solid substrate where the softness of the underlying intermolecular potential allows multiple occupancy of binding sites. Chapter 3 is adapted from published work in Ref. [32], co-authored with Dr. Alex Popov and Dr. Rigoberto Hernandez. Complex spatial arrangements are generated as the incident macromolecules adsorb on the substrate and overlap. We derive two isotherms to predict the fraction of the substrate that is covered and compare these analytical results with results generated through computer simulation. The results presented in this chapter elucidate properties of crystallization phenomena observed in macromolecular structures at mesoscopic length scales.

The dynamical properties of the stochastic soft matter system developed in Chapter 2 are described in Chapter 4. By varying density and interparticle softness, the dynamical properties of a system of penetrable rods are elucidated by theory and computer simulation. Various dynamical observables are measured from simulation, and these results are compared to developed theoretical predictions. We find that, in liquid density regimes, Enskog corrections to the predictions of Boltzmann kinetic theory for transport properties suffice

to describe observables, implying that uncorrelated collision processes dominate the decay of temporal correlation functions.

Chapter 5 contains a study of the dynamics of a model chemical reaction wherein a reactant species is induced to surmount an energy barrier that is moving under the influence of an oscillatory external field. This chapter is largely adapted from published work in Refs. [28] and [29], co-authored with Dr. Thomas Bartsch and Dr. Rigoberto Hernandez. We show that the reaction rates can be determined through stability analysis of a non-autonomous transition state (TS). This finding elucidates the geometry of a fundamental phase space structure whose stability directly dictates the rate of conversion from reactant to product. It also allows for the prediction of rates without knowledge of the dynamics or energetic distributions of the reactive population. We have identified a connection between the rates of a reaction and the relative stability of a global non-recrossing TS. The exact TS trajectories for reactions driven by waveforms consisting of sinusoidal convolutions in the frequency ratios of 1, 1:2, 1:2:3 at the harmonic limit are derived using Fourier series expansion. We calculate the reaction rate numerically and compare the results to those predicted by stability analysis of the TS. These results are in excellent agreement over all functional forms of the driving external field we have studied. Finally, in Chapter 6, concluding remarks are presented and the significant findings of Chapters 2-5 are summarized.

CHAPTER II

STRUCTURE OF A STOCHASTIC MIMIC OF SOFT PARTICLES

2.1 Introduction

The aggregation of small molecular motifs into macromolecular structures gives rise to assemblies and materials with distinct emergent behavior. For processes in which intermolecular forces drive self-assembly, such as polymerization and colloidal flocculation, a theoretical formulation is often intractable from microscopic statistical mechanics due to the complex spatial arrangements of the resulting compositions. The study of such systems is often relegated to purely computational methods, but because of the large number of atoms of which they are composed, macromolecules are difficult to simulate on relevant biological and chemical length scales. The computationally taxing procedure of simulating large systems can be accelerated by reducing the atomic degrees of freedom to a coarse-grained description [34, 169, 142]. In the coarse-grained picture, macromolecules can be treated as overlapping particles when soft interaction potentials allow them to interpenetrate relative to their radius of gyration. The complex nature of soft matter interactions is manifested in systems with rheological and structural properties that are absent in simple fluids [112, 94, 132]. Previous modeling of soft matter systems using a class of potentials that are finite valued at the origin, bounded potentials, has elucidated the phase behavior and structure of colloid suspensions [61], polymer-colloid mixtures [170], star polymers and globular micelles [145], and dendrimers [110].

The generalized exponential model of index n (GEM-n), [137, 135]

$$V^{\mathrm{GEM}}(r) = \epsilon \exp\left[-\left(\frac{r}{\sigma}\right)^n\right], \tag{1}$$

is a prototypical bounded potential. The softness of the potential is specified by the parameter n. For the exponential parameter value $n = 2$, the GEM-2 becomes the Gaussian core (GC) model [173]. The potential (1) is finite valued at $r = 0$ and this gives rise to complex phase and thermodynamic behavior [208, 95, 79]. In modeling solutions of micelles,

Marquest and Whitten introduced the penetrable sphere (PS) model [124],

$$V^{\mathrm{PS}}(r) = \begin{cases} 0, & r > \sigma \ , \\ \epsilon, & r \leq \sigma \ . \end{cases} \tag{2}$$

The PS model is the limiting form of the GEM as $n \to \infty$, where σ is the diameter of the particle and ϵ is a finite energy. Only as $\epsilon \to \infty$ does the PS model take the form of the ubiquitous hard-core (HC) potential [20, 154, 192, 167], otherwise the particles have a non-zero probability to overlap due to the finite nature of the energy barrier. For $\epsilon = 0$ the PS model represents the ideal gas. The PS model is perhaps the most well-studied bounded potential. Its simplicity allows for the prediction of observables of the system that in most cases are derivable using modified HC arguments [166, 122, 123, 175, 22, 198, 113]. As is common with the completely repulsive HC potential, the PS model has been extended to include attractive regions [168, 46, 47, 121] for the purpose of modeling complex fluids.

When particles are allowed to interpenetrate due to the bounded nature of the potentials that govern their interactions, the effective volume occupied by the particles in the system is reduced from the non-overlapping value. The spatial properties of such systems are of interest not only in macromolecular assembly, but also in modeling the structure of porous media [21, 158, 184, 157]. While the volume occupied by soft-edge potentials, like the GC model, is ill-defined due to the lack of a distinct spatial boundary, the geometric properties of systems with hard-edge boundaries are amenable to both analytic [204, 183, 60, 186] and computer studies.[176, 102, 50, 90] In order to bridge the dynamics of a system between completely hard and completely ideal behavior, Blum and Stell [15] introduced an abstraction of a bounded potential, called the permeable-sphere model (PSM). Within this model the radial distribution function $g_2(r)$ is constant in the penetrative region (PR) $0 \leq r < \sigma$ and equal to a penetration parameter δ,

$$g_2(r) = \delta. \tag{3}$$

Thus, the PSM uses one parameter to bridge the limiting behaviors.

In this Chapter, a stochastic penetration algorithm (SPA)[31] is used to model penetrative particles. In the SPA, the outcome of collisions between particles are governed

by stochastic rules. Stochastic collision rules have been used previously in, for example, Lorentz gas systems [7, 8, 36, 43]. Therein, the collision with a fixed scatterer can lead either to the reflection of the colliding particle or the transmission of the particle through the scatterer, subject to the outcome of a stochastic variable. These stochastic models have provided analytic insight that was previously unavailable from purely deterministic models.

Within the framework of the SPA, a random process—consistent with a given probability—assigns each event between a pair of particles as being entirely penetrable or hard sphere. The nature of the interaction remains the same as long as the pair remains within some distance of each other, and this continuous time interval defines a given event. Through a penetration parameter δ, a mixture of completely hard and completely soft interactions are constructed. The PSM model can be equated to the SPA model only in the limit of infinite dilution. For finite densities, the mixing of stochastic collision events in the SPA generates complex spatial configurations and non-linear behavior for $g_2(r)$ in the PR and thus Eq. (3) does not hold. The dynamics of single-particle trajectories evolved through the SPA are non-Newtonian as particles are allowed to enter classically prohibited regions subject to the outcome of a stochastic variable. However, by combining these hard and soft collision outcomes, the SPA generates ensemble averages that retain the pertinent features of analogous deterministic systems, such as the PS model.

In coarse-grained systems that are governed by imposed Hamiltonian dynamical rules, the probability of entering a repulsive potential region is dependent on the relative velocity of the two colliding particles [175]. If the relative velocity between a colliding pair is below the respective energy threshold for that region, the result is a turning point for soft-edge potentials like the GC model, or an impulsive elastic collision in hard-edge potentials such as the PS model.

In the SPA model, the kinetic energy of a colliding pair plays no role in the penetration process. A set of particles with a relative velocity of small magnitude will sometimes overlap, traversing the now penetrable core. Moreover, a set of particles with large kinetic energy can be repelled by the stochastic collision outcome. The probability of penetration is thus uniformly distributed over the entire energy distribution. The ensemble average

of these outcomes generates spatial configurations that are analogous to those found by deterministic bounded potentials such as the PS model. The effective pairwise potential is determined by δ. It replaces the detailed forces in the interaction (or collision) region when moving from the all-atom to CG representations. Thus the SPA is a HC model augmented only by a single pairwise parameter, characteristic of a particles softness, connecting deterministic systems governed by Newtonian mechanics to a stochastic system governed by non-Newtonian mechanics.

When the particles are allowed to overlap, a fundamental observable is the volume fraction ϕ occupied by the particles in the system. We find that ϕ can be predicted using probabilistic arguments and that the system's structural behavior is approximately that of deterministic soft potentials. Thus, when a system's degrees of freedom are coarse-grained, the representative equations of motion can be considered probabilistically as well as deterministically. This result has direct applications in modeling macromolecular assemblies where, previously, deterministic bounded potentials have been utilized to probe the spatial structure at the coarse-grained level.

This Chapter is outlined as follows: The numerical methods used to simulate and measure the volume occupied by a system of particles governed by a stochastic collision rule are described in Sec. 2.2. Their structure can be characterized by the radial distribution function $g_2(r)$. A mapping of $g_2(r)$ between the SPA and soft-particle systems is used in Sec. 2.3 to obtain a correspondence between an SPA model with N-body penetration parameter ζ to a soft-particle system with pairwise softness δ . Analytic theories capable of predicting the occupied volume in dimension $d \leq 3$ for SPA particles are presented in Sec. 2.4 and tested by comparison between the results measured from molecular dynamics (MD) in Sec. 2.5. Finally, in Sec. 2.6, we conclude by summarizing the extent to which the SPA model can be used to obtain structure and dynamics of corresponding soft-particle systems, and the extent to which coarse-grained models can be enhanced through the use of the SPA.

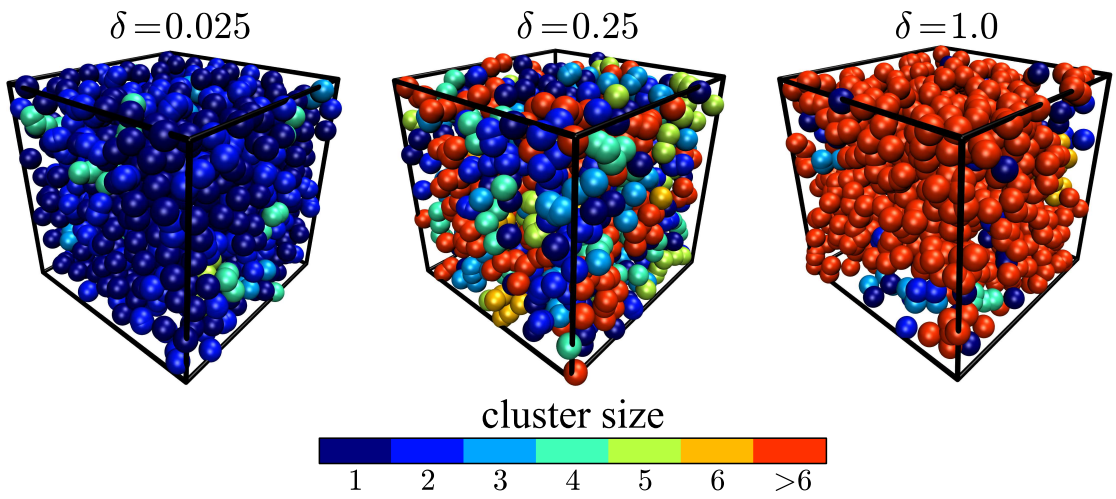

Figure 3: Selected spatial configurations of $N = 1000$ spheres at $\phi_0 = 0.4$ for $\delta = 0.025$ (left), $\delta = 0.25$ (middle), and $\delta = 1$ (right). The particles are colored according to cluster size N_c.

2.2 Numerical Methods

2.2.1 Model and Simulation Details

Dynamical simulations have been performed on a system of $N = 1000$ spheres with each sphere having a mass m and diameter σ. These simulations were performed in a d-dimensional periodic hypercube with sides of length L. The volume of a single sphere in dimension d is

$$v^{(d)} = \frac{\pi^{d/2}}{\Gamma(1+d/2)} \left(\frac{\sigma}{2}\right)^d. \tag{4}$$

The HC volume fraction ϕ_0 is the occupied volume fraction of the system when no spheres overlap. In dimension d, the HC volume fraction is

$$\phi_0^{(d)} = \frac{N v^{(d)}}{L^d}. \tag{5}$$

If the spheres are allowed to overlap due to softness in the governing potentials, ϕ_0 is an upper bound to the actual volume fraction ϕ, i.e., $\phi \leq \phi_0$. In simulation, the box volume L^d is changed to reach the target ϕ_0 value while keeping N constant. In the SPA, penetrability is realized by using a single parameter $0 \leq \delta \leq 1$. The limiting values of this parameter, $\delta = 0$ and $\delta = 1$, correspond to the HC and the ideal behavior limits, respectively.

The SPA algorithm is implemented as follows:

1. *For every MD trajectory a value of the penetration probability* $\delta \in [0,1]$ *is preassigned and maintained throughout the trajectory.*

2. *When a pair of spheres* i *and* j *collide at time* $t_{\rm col}$*, a random number* $a_{ij}\left(t_{\rm col}\right) \in [0,1]$ *is generated from a uniform distribution. This random number determines, upon its comparison to* δ*, whether or not the pair of particles will interact. If* $a_{ij}\left(t_{\rm col}\right) > \delta$*, they interact via a hard potential; otherwise the particles penetrate each other without interacting.*

3. *For the overlapping particles which do not interact, this relationship between* $a_{ij}\left(t_{\rm col}\right)$ *and* δ *is maintained until* $r_{ij} > \sigma$*, i.e. the zero interaction potential is kept until the pair breaks apart.*

4. *If the same pair of particles* (i,j) *undergoes a new collision at time* $t_{\rm col}+\tau$*, then a new random number* $a_{ij}\left(t_{\rm col}+\tau\right)$ *is generated and the acceptance algorithm is repeated.*

The SPA procedure generates the following stochastic potential between spheres i and j:

$$V_{ij}^{\rm SPA}(r) = \begin{cases} 0, & r > \sigma \ , \\ 0, & r \leq \sigma \ \text{ and } \ a_{ij}\left(t_{\rm col}\right) < \delta \ , \\ \infty, & r \leq \sigma \ \text{ and } \ a_{ij}\left(t_{\rm col}\right) > \delta \ , \end{cases} \tag{6}$$

with the random number a_{ij} giving rise to the stochastic nature of the interactions. The potential (6) is used to construct all pairwise interactions in the SPA simulations.

When the stochastic interaction variable $a_{ij}\left(t_{\rm col}\right) < \delta$ the particles penetrate each other without interacting leading to pairwise ideal behavior. For trajectories with $\delta = 1$, all pairwise interactions are ideal. In this limit, the structure and dynamics are completely ideal with no spatial correlation between particles.

For trajectories with $\delta = 0$, all pairwise interactions are governed by a HC potential and the dynamics observed are that of a d-dimensional hard sphere system. For $\delta > 0$, the particles can take on overlapping configurations. When the particles overlap, clusters are formed. The size $N_{\rm c}(i)$ of a cluster is defined by the number of spheres connected by overlaps to i other particles, self-inclusive [198]. As illustrated in Fig. 3, the distribution

of cluster sizes is strongly influenced by the value of δ. At small δ the system consists of mostly monomers and dimers. For intermediate δ, higher order oligomers are formed. For $\delta = 1$ the particles have no spatial correlation and are Poisson distributed. In this state, the structure of the system is dominated by transient high order clusters.

The interaction between all particle pairs can be represented by undirected network graphs with each node corresponding to a specific particle. For a system of N particles there are $N(N-1)/2$ possible connections associated with the pairwise interactions — HC at $\delta = 0$ or penetrative at $\delta = 1$. Fig. 4 shows representative graphs of different configurations that can be observed using the SPA. As the system evolves in time, connections can be made and broken due to the stochastic nature of the SPA allowing for a sampling of different network configurations. For both a Tonks and an ideal gas, the spatial boundaries for every particle can be calculated from knowledge of the connection network. These boundaries define the configuration integral and lead to closed form solutions of the partition functions. The equilibrium thermodynamic properties for these systems are consequently also contained in these types of connection networks. They can be extracted directly from the graphs in Fig. 4 and the corresponding adjacency matrices used to construct them.

In the SPA, the positions and velocities of each particle are updated through a time-driven hard-sphere algorithm [3]. When collisions occur ($a_{ij}(t_{\text{col}}) > \delta$), they are elastic and thus the total kinetic energy of the system is conserved. The potential energy of the system V is also constant, $V = 0$, as given by (6). For deterministic dynamical systems governed by soft potentials, such as the GEM, the kinetic energy is not conserved and the total energy of the system is varyingly partitioned into the potential and kinetic terms.

The initial positions of the particles are chosen by placing their centers at distinct points on a uniform lattice. The initial velocities are sampled from a Maxwellian distribution corresponding to $T = 300$ K, although for the athermal potential (6) the choice of temperature is arbitrary.

The simulations are partitioned into two stages: an initial spatial relaxation stage and a second sampling stage. The first stage is implemented to achieve a spatially relaxed state. After the initial velocities are assigned, these velocities are rescaled such that the total

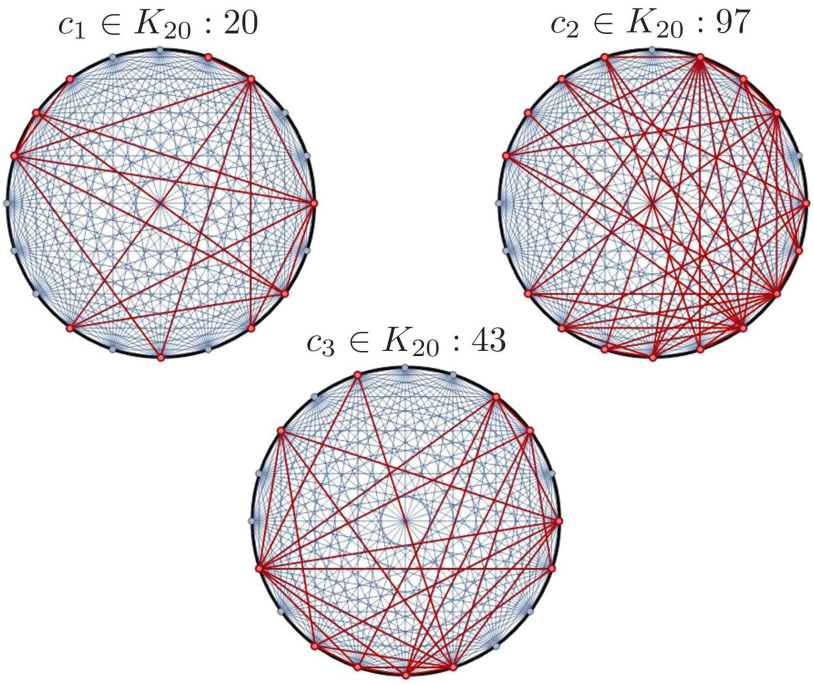

Figure 4: Representative graphs for a system consisting of $N = 20$ particles, showing different configurations of the connection network. Each graph node located on the circumference of the circle corresponds to a different particle. The lines represent the complete graph K_N — all the $N(N-1)/2$ theoretically possible connections available for a system. Lines are colored in red or blue depending on if they correspond to an activated HC connection or a non-activated connection, respectively. The network with j activated connections is denoted as $K_N : j$. The configuration c_k is an element of the possible set of permutations for a $K_N : j$ network.

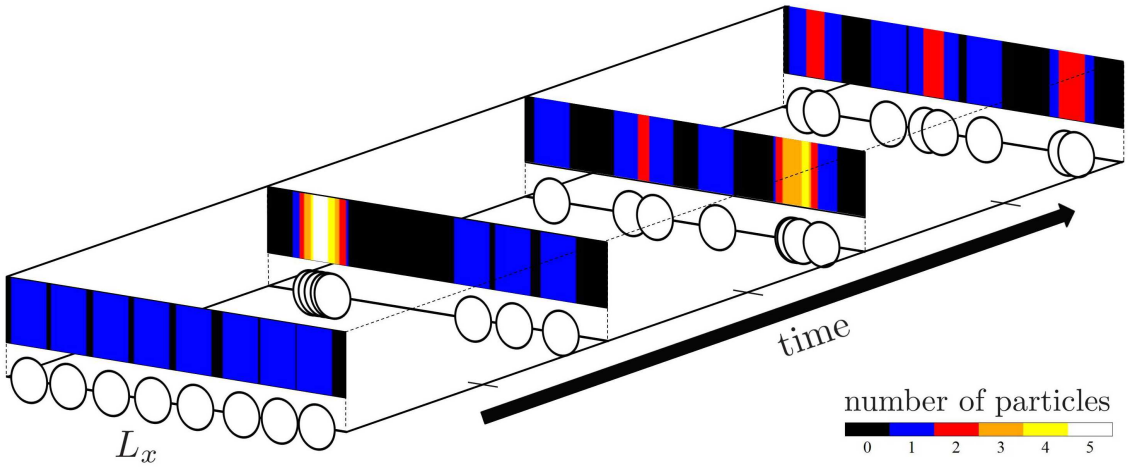

Figure 5: Several snapshots of overlapping configurations for a system of 8 particles in one dimension. The connection network of this 8 particle system can be represented by the complete graph K_8. The network evolves through different connection networks $c_1 \to c_2 \to c_3 \to c_4$, respectively, illustrating how the observed volume fraction $\phi(t)$ starts with ϕ_0 and then changes with time due to particle overlaps.

energy of the system, for every trajectory becomes $dNk_{\mathrm{B}}T/2$. The system is then aged for 5×10^5 collisions to achieve a spatially relaxed state (both hard and soft interactions are counted as collisions in this phase). As observed previously,[31] ϕ relaxes to an equilibrium value quickly during this equilibration phase. During a second sampling stage, all statistical data is generated by sampling the system at constant time intervals.

Figure 5 shows different spatial configurations of overlapping particles that can be observed for a penetrable system in one dimension. Note that the connection network $K_N : j$, presented in Fig. 4, does not specify the spatial arrangement of a set of overlapping particles as a given spatial configuration can be generated by many such networks. As illustrated in Fig. 5, the volume fraction ϕ is reduced from its initial value ϕ_0 as the rods interpenetrate. The geometry of the system, as well as the distribution of free volume cavities, can be significantly altered by this penetration. The details for the exact methods used to sample the studied observables are discussed in Sections 2.2.2 and 2.3.

The HC volume fractions chosen for the study in one dimension were in the range $\phi_0 \in [0.125, 0.968]$. A one-dimensional gas does not exhibit a phase transition [194] and therefore the system remains in the isotropic phase within this range of volume fractions.

An isotropic-solid phase transition occurs for HC systems only in dimensions greater than one.

A system of hard disks in two dimensions undergoes an isotropic-hexatic phase transition at $\phi_0 \approx 0.7$ and a hexatic-solid phase transition at $\phi_0 \approx 0.73$ [81, 120]. The HC volume fractions chosen for the study in two dimensions are ranged $\phi_0 \in [0.125, 0.75]$. In three dimensions, freezing occurs at $\phi_0 \approx 0.491$ and melting at $\phi_0 \approx 0.543$ with isotropic-solid coexistence occurring between these two volume fractions [74, 196, 143]. In three dimensions we have studied volume fractions $\phi_0 \in [0.1, 0.5]$.

In general, when $\delta \neq 0$, the observed volume fraction ϕ is much less than the HC volume fraction ϕ_0. When the particles are allowed to overlap, the phase boundaries present in HC systems cease to exist and complex phase behavior can occur as the particles form clusters [113, 135, 134, 210, 27].

2.2.2 Measurement of the Occupied Volume Fraction

For systems consisting of particles with well-defined spatial boundaries, a fundamental observable is the occupied volume fraction. Through the introduction of an indicator function [186]

$$I(\mathbf{r}) = \begin{cases} 1, & \text{if } \mathbf{r} \in \text{particle phase} , \\ 0, & \text{otherwise} , \end{cases} \tag{7}$$

a spatial coordinate $\mathbf{r}$ can be classified as belonging to the particle phase or the void phase. The occupied volume fraction is the expectation value of the indicator function,

$$\phi = \langle I(\mathbf{r}) \rangle , \tag{8}$$

over the domain of all points $\mathbf{r}$ in the simulation subspace $\mathcal{V}$.

Determination of this volume fraction for a system of overlapping particles is non-trivial and often computationally taxing to measure in simulation. Two of the most used methods to measure ϕ are Monte Carlo (MC) integration [102, 41] and the GRID method [102, 176, 175].

The MC approach involves generating a large number of random coordinates in $\mathcal{V}$, and checking if those coordinates are overlapped by any particle from the system. The ratio of

the number of sampling points that are overlapped to the total number of points generated is ϕ, as given by Eq. (8). The GRID method involves discretizing the sampling space $\mathcal{V}$ into uniform bins. These bins are then probed individually to see if any particle overlaps with the chosen bin. The ratio of the number of occupied bins to that of total bins is ϕ.

The accuracy of both the MC and GRID methods increases with an increasing number of sampling points or bins used. However, the trade-off to this increase in accuracy is an increase in computational time. Thus, the number of sampling points or bins is often chosen such that there is an acceptable balance between statistical accuracy and computational efficiency.

To overcome this computational problem, a cluster measure approach can be applied for calculating the volume fraction in one dimension. A cluster is defined as a formation consisting of $N \geq 1$ particles (thus, a single particle can be termed a cluster). For a set of N particles, there exist a maximum of N clusters, corresponding to a configuration where no particles are overlapped, and a minimum of one cluster, corresponding to the configuration where all of the particles are overlapped into a single cluster. In one dimension, it is simple to determine the beginning and end points, x^{begin} and x^{end}, of these clusters along the line segment L_x. After ordering the particles, ϕ can be found by summing the sizes of all the (nonoverlapping) clusters:

$$\phi = \frac{1}{L_x} \sum_{i=1}^{\text{all clusters}} (x_i^{\text{end}} - x_i^{\text{begin}}) \, . \tag{9}$$

This method gives no measurement error and is accurate to floating point precision. If comparably efficient algorithms can be applied in higher dimension, large increases in computational efficiency could be observed for other models where there is overlap in one phase of the media and a measure of occupied volume is computationally taxing. The simulation cost of HC systems far from the thermodynamic limit is negligible compared to the computation time of post-processing the trajectories and, thus, using the cluster measure method greatly accelerates the rate of data acquisition and analysis.

Although algorithms that give an exact measure of the occupied volume are known in one and two dimensions [17, 31], we have used the MC sampling method to maintain a uniform

methodology for all dimensions studied. We have found that MC gives an acceptable mix between ease of implementation, computational efficiency, and statistical accuracy. To measure ϕ, for each parameter set $\{\delta, \phi_0\}$, 10^4 frames were integrated using 10^6 sampling points per frame. A single trajectory was evolved to generate the configurations used for integration. Previous studies using 8000 trajectories yielded the same results, up to finite size effects [31], thus confirming the ergodicity of systems evolving through Eq. (6).

2.3 Radial Distribution Function

When a macromolecule's atomistic degrees of freedom are reduced to a coarse grained description, the effective potential between the coarse-grained structures can be modeled using bounded potentials. The bounded, i.e., finite, nature of these potentials allows for the centers of mass of the coarse-grained macromolecules to overlap relative to their radius of gyration σ. This leads a characteristic feature in $g_2(r)$ where there is a non-zero probability to find the interacting macromolecules directly on top of each other, i.e., $g_2(0) \neq 0$. This is in contrast with simple fluid interactions in which the excluded volume of the nuclei give zero probability to find the interacting molecules in a completely overlapped state. The softness of the governing coarse-grained potentials leads to cluster formation [113, 135, 134, 210, 27] and complex functional forms for $g_2(r)$ in the penetrative region (PR) defined by r such that $0 \leq r < \sigma$. For systems that evolve through the potential (6), the functional form of $g_2(r)$ depends on the pairwise penetration probability δ and therefore it must be included as a parameter, $g_2 = g_2(r; \delta)$.

In the dilute limit, when three and higher order interactions can be neglected, $g_2(r; \delta)$ is constant in the PR and equal to δ. As the density of the gas is increased multi-body effects dominate the potential of mean force. In the language of the Ornstein-Zernike formalism, indirect contributions dominate the structural assembly whereas the direct contributions leading to $g_2(r) = \delta$ are small. When these indirect contributions are strong, as is the case in dense N-body systems, $g_2(r; \delta) \neq \delta$ due the multi-body effects. The potential of mean force (PMF) $w_2(r; \delta)$ between a pair of particles can be extracted from $g_2(r; \delta)$ through the

relationship

$$g_2(r;\delta) = e^{-\beta w_2(r;\delta)}, \tag{10}$$

where $\beta = 1/k_{\mathrm{B}}T$.

To account for multi-body terms, the pairwise softness δ must be be mapped to an N-body softness parameter ζ. The heuristic parameter ζ accounts for multi-body induced effects in the pairwise potential through a weighted distribution of energy states in the PR. In dimension d, we define this parameter as the probability to find a particle in the PR, with respect to a test particle, for a specific value of δ, normalized by the ideal ($\delta = 1$) probability,

$$\zeta_{\mathrm{V}}^{(d)}(\delta) = \frac{\displaystyle\int_0^\sigma r^{d-1} e^{-\beta w_2(r;\delta)}\, dr}{\displaystyle\int_0^\sigma r^{d-1} e^{-\beta w_2(r;1)}\, dr}. \tag{11}$$

For $\delta = 0$, $\zeta_{\mathrm{V}} = 0$ as particles are not allowed in the PR and for $\delta = 1$, $\zeta_{\mathrm{V}} = 1$. Thus, the limiting values of ζ_{V} are in agreement the limiting values of δ.

The results given by Eq. (11) in one, two, and three dimensions are shown in Fig. 7(a), (b), and (c), respectively. The trend in $\zeta_{\mathrm{V}}^{(d)}$ is the same across all dimensions d. As we will show, ϕ has distinct trends that depend highly on the dimensionality of the system. To account for these dimensionally-variant spatial effects, we conjecture, and show in Sec. 2.5, that that a line (contour) integral of the Boltzmann-weighted states over the PR along the one-dimensional line connecting the centers of a pair of particles,

$$\zeta_{\mathrm{L}}(\delta) = \frac{\displaystyle\int_0^\sigma e^{-\beta w_2(r;\delta)}\, dr}{\displaystyle\int_0^\sigma e^{-\beta w_2(r;1)}\, dr}, \tag{12}$$

will more effectively follow the trends observed in spatial properties, specifically ϕ, as the system dimensionality is increased.

Figure 6 shows $g_2(r;\delta)$ for a one-dimensional system at $\phi_0 \in \{0.25, 0.5, 0.75\}$ over various values of δ. For $\phi_0 = 0.25$, the radial distribution function approaches constant behavior for $r < \sigma$. At higher ϕ_0 values, in the PR, $g_2(r;\delta) \neq \delta$ and particles have a propensity to be in overlapped states which is evident by observing that $g_2(0;\delta) \geq g_2(\sigma^-;\delta)$, with the equality holding as $\phi_0 \to 0$. (Note that σ^- and σ^+ correspond to the approach of r to σ from the left

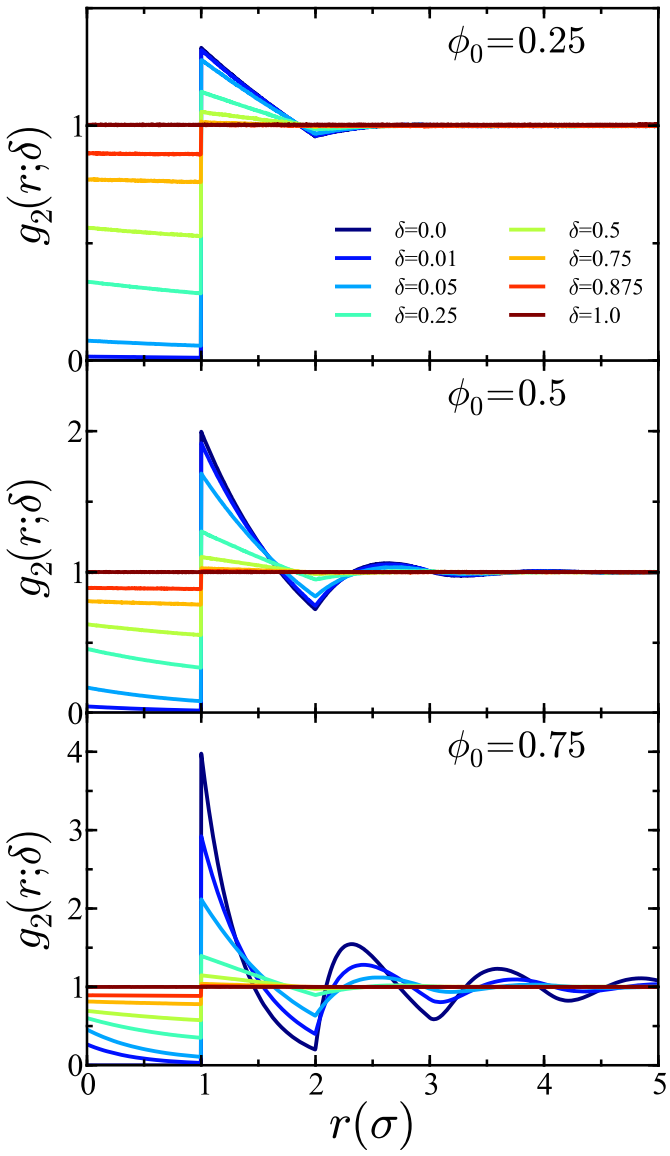

Figure 6: The radial distribution function $g_2(r;\delta)$ for one-dimensional rods ($d = 1$) measured from simulations at various ϕ_0 and δ values using a histogram bin width of $\sigma/300$. The integration was performed for each set of parameters $\{\phi_0, \delta\}$ over a varying number $(5 \times 10^5 - 2 \times 10^6)$ of configurations.

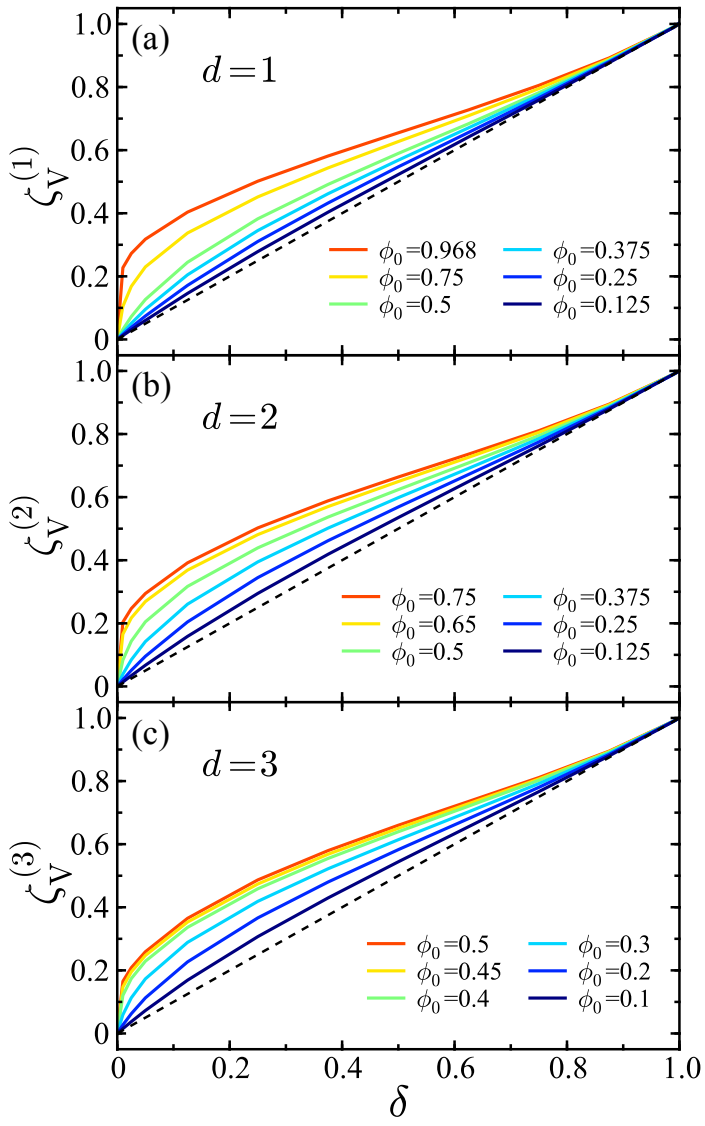

Figure 7: $\zeta_V^{(d)}$ as a function of δ, at various ϕ_0 values, for systems in (a) $d = 1$, (b) $d = 2$, and (c) $d = 3$ dimensions. The black dashed line corresponds to the infinite dilution limit.

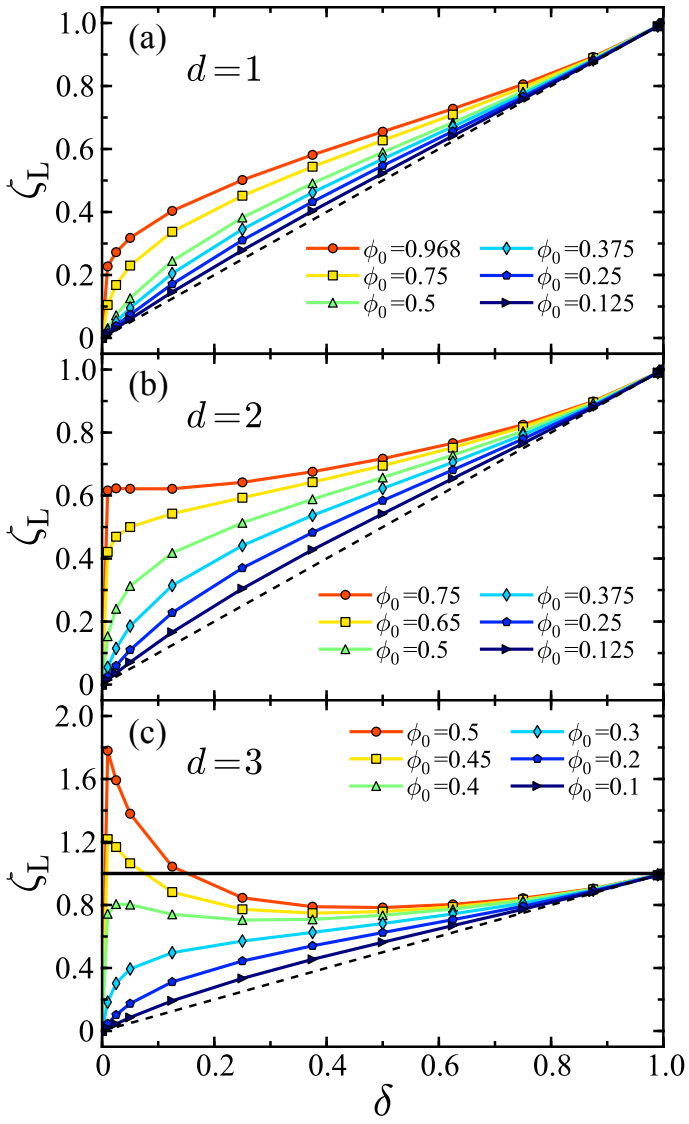

Figure 8: ζ_L as a function of δ, at various ϕ_0 values, for systems in (a) $d = 1$, (b) $d = 2$, and (c) $d = 3$ dimensions. The black dashed line corresponds to the infinite dilution limit. The black solid line in (c) is the $\zeta_L = 1$ upper bound.

or the right, respectively.) The reduced volume state arises from the overlap of effectively-ideal particles into clusters ($N_c \geq 2$). The particles in the cluster are free to overlap at no energy cost as the interaction between them is ideal. If the cluster has HC interactions with a shell of particles surrounding them, the HC interactions push the clustering particles into a completely overlapped state forcing the cluster to minimize the occupied volume. This confinement effect gives rise to the $g_2(0;\delta) \geq g_2(\sigma^-;\delta)$ behavior. It is interesting to note that while particles belonging to the cluster have no intracluster interactions, the characteristic concavity in $g_2(r)$ is also observed in deterministic models in which clustering is brought on by intermolecular and intramolecular interactions.[123, 122, 166, 27]

Figure 8(a) shows $\zeta_{\rm L}$ as a function of δ for a one-dimensional system. The $\zeta_{\rm L}$ values are calculated by numerical integration of Eq. (12) for $g_2(r;\delta)$ values obtained from MD simulations. At the dilute density $\phi_0 = 0.125$, $\zeta_{\rm L}$ weakly deviates from the ideal δ value. As ϕ_0 is increased toward the maximum HC packing fraction, $\phi_0 = 1$, a characteristic shape occurs. For small δ, the $\zeta_{\rm L}$ values deviate strongly from ideal behavior. As δ is increased toward the ideal limit, $\delta = 1$, $\zeta_{\rm L}$ deviates less strongly. This effect is induced by the SPA, as the particles in the system are not strongly correlated when the probability of collision is small.

In two dimensions, as shown in Fig. 9, the trends of $g_2(r;\delta)$ are generally the same as those seen in one dimension. The HC volume fraction $\phi_0 = 0.75$ is above the solid phase transition and $g_2(r;0)$ begins to take on the characteristic shape of a solid. For $\phi_0 = 0.75$ and $\delta = 0.01$, $g_2(0;\delta) > g_2(\sigma^+;\delta)$ showing that the density of the system is greatest inside the the PR. This affects $\zeta_{\rm L}$ strongly, as shown in Fig. 8(b) where the $\zeta_{\rm L}/\delta$ ratios are larger than those in one dimension for small δ.

In Fig. 10, the measured $g_2(r;\delta)$ functions are shown for a system of three-dimensional spheres at various ϕ_0 and δ values. For small δ and large ϕ_0, highly overlapped states are heavily favored and $g_2(0;\delta) \gg g_2(\sigma^+;\delta)$ with respect to one and two dimensional systems. In this large-ϕ_0, small-δ regime, overlapping configurations dominate in the distribution of particles. This clustering state is analogous to the so-called *"cluster anomaly"* found in the deterministic (GEM-n) model [27]. In the SPA it leads to a turnover in the $\zeta_{\rm L}$ function

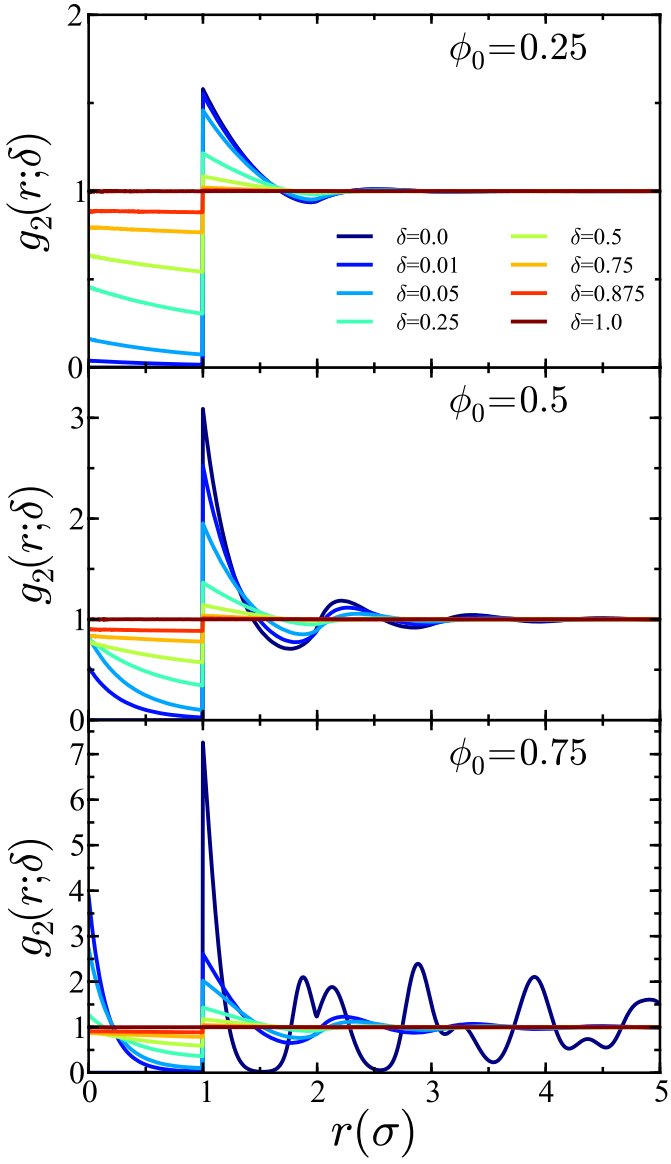

Figure 9: The radial distribution function $g_2(r;\delta)$ for two-dimensional disks ($d = 2$) measured from simulations at various ϕ_0 and δ values using a histogram bin width of $\sigma/300$. The integration was performed for each set of parameters $\{\phi_0, \delta\}$ over a varying number $(5 \times 10^5 - 3 \times 10^6)$ of configurations.

for larger packing fractions ϕ_0 as shown in Fig. 8(c), whereas in one and two dimensional systems $\zeta_{\rm L}$ is a monotonically increasing function of δ at ϕ_0.

The trends observed in $g_2(r;\delta)$ suggest that as the dimensionality is increased, pairs of overlapping particles become more confined by the first solvation shell. For $d = 1$, the number of neighboring sites is 2. For a particle to be allowed to leave a cluster, there must either be a cavity available to accommodate the particle, or a neighboring site must switch interaction from HC to ideal, i.e., a random number $a\,(t_{\rm col})$ generated at the time of collision must be less than δ. With increasing ϕ_0, the probability to find a cavity with enough free volume decreases. Thus, for a particle to leave a cluster it must do so through a stochastic switching of interactions. As the dimensionality is increased, the number of neighboring sites also increases due to the respective packing geometries. With increasing d, the particles in a cluster interact repulsively with more neighbors. This increase in the number of neighbors forces the cluster into a heavily overlapped state. This phenomenon is manifested in the trends of $g_2(r;\delta)$ discussed above.

2.4 Theory

In this section, we derive two expressions for predicting the occupied volume fraction ϕ of a system of SPA particle with hard core volume fraction ϕ_0. The first one is an analog of an expression derived by Rikvold and Stell (RS) [160, 161] for the PSM using the Kirkwood superposition approximation [92], but now obtained for a system of particles evolving through the SPA. The second expression relies on mean field arguments for the conditional probabilities of finding a pair of particles in an overlapped state as particles are sequentially added to the system.

2.4.1 Kirkwood Superposition Approximation for SPA particles

In the PSM [15], the pair correlation function $g_2(r)$ is taken to be a constant in the PR. In this limit, we can define δ, as used in the SPA model, as that constant, i.e., $g_2(r;\delta) = \delta$. Thus, in analogy with Eqs. 11 and 12, both $\zeta_{\rm V}^{(d)}$ and $\zeta_{\rm L}$, for any dimension, are equal to δ, i.e.,

$$\zeta_{\rm L,V}(\delta) = \delta. \tag{13}$$

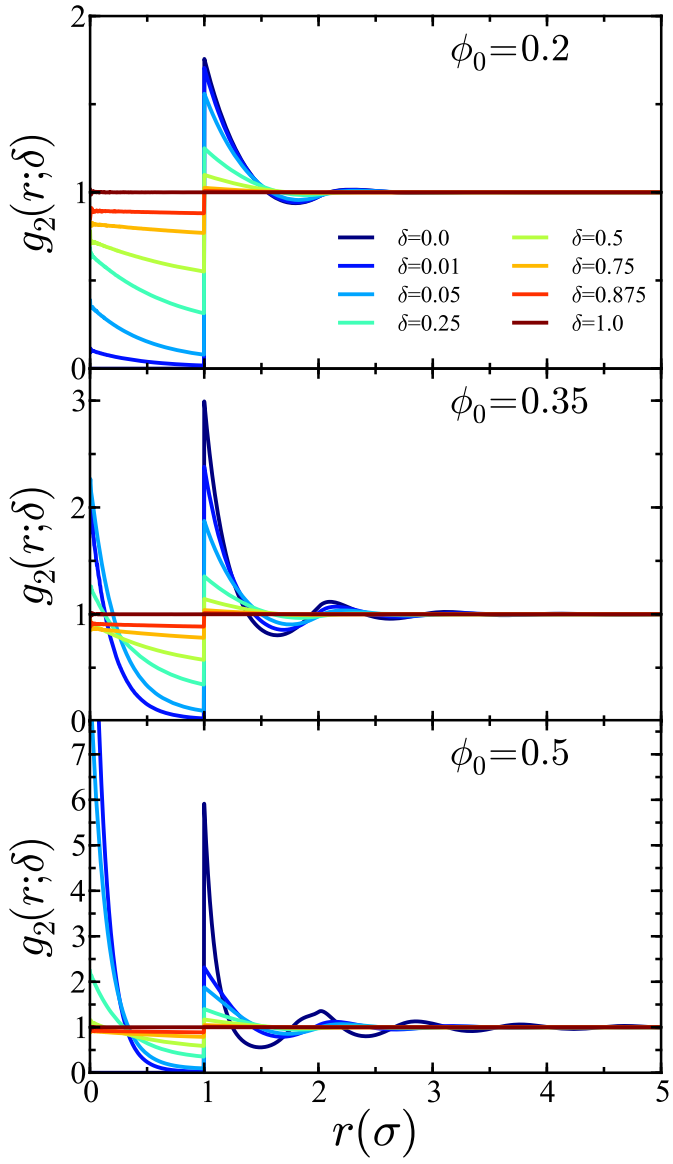

Figure 10: The radial distribution function $g_2(r;\delta)$ for three-dimensional spheres ($d = 3$) measured from simulations at various ϕ_0 and δ values using a histogram bin width of $\sigma/300$. The integration was performed for each set of parameters $\{\phi_0, \delta\}$ over a varying number $(5 \times 10^5 - 3 \times 10^6)$ of configurations.

This is the limiting case of the SPA model at infinite dilution. To predict ϕ in the PSM, RS also used the Kirkwood superposition approximation [92] for higher-order correlation functions,

$$g_n\left(\mathbf{r}_1,\ldots,\mathbf{r}_n\right)=\prod_{1\le i<j\le n} g_2(r_{ij}), \tag{14}$$

e.g.,

$$g_3(\mathbf{r}_1,\ldots,\mathbf{r}_3)=\delta^3, \tag{15}$$

$$g_4(\mathbf{r}_1,\ldots,\mathbf{r}_4)=\delta^6, \tag{16}$$

and in the thermodynamic limit ($N\to\infty, L^d\to\infty, N/L^d=const$) derived a dimensionally invariant expression for the occupied volume fraction through a power series in ϕ_0 [160, 161, 21, 184],

$$\phi^{\text{RS-SPA}}(\phi_0,\delta)=-\sum_{k=1}^{\infty}\frac{(-\phi_0)^k}{k!}\delta^{\frac{k(k-1)}{2}}, \tag{17}$$

where ϕ_0 is the volume fraction for a HC system. From Eq. (17), the limiting values of δ give,

$$\phi^{\text{RS-SPA}}(\phi_0,0)=\phi_0, \tag{18}$$

$$\phi^{\text{RS-SPA}}(\phi_0,1)=1-e^{-\phi_0}. \tag{19}$$

Equation (18) is the HC volume fraction, given by Eq. (5). Equation (19) is the Poisson distributed result [157, 182] for the volume fraction of particles with no spatial correlation at the thermodynamic limit.

Far from the thermodynamic limit (small N), Eq. (17) must be replaced by its finite variant [31],

$$\phi^{N\text{-SPA}}(N,\phi_0,\delta)=-\sum_{k=1}^{N}\binom{N}{k}\frac{(-\phi_0)^k}{N^k}\delta^{\frac{k(k-1)}{2}}. \tag{20}$$

where $\binom{N}{k}$ is the binomial coefficient, and the last term in the summand is the k-th order correlation function g_k. The difference between Eq. (17) and Eq. (20) lies in the series expansions over ϕ_0:

$$\phi^{N\text{-SPA}}=-\sum_{k=1}^{N}C'_k\phi_0^k\,, \tag{21}$$

whereas

$$\phi^{\text{RS-SPA}} = -\sum_{k=1}^{\infty} C_k \phi_0^k \,. \tag{22}$$

The coefficients of these series are

$$C'_k = \binom{N}{k} \frac{(-1)^k}{N^k} \tag{23}$$

and

$$C_k = \frac{(-1)^k}{k!}, \tag{24}$$

where $\binom{N}{k}$ is the binomial coefficient. As $N \to \infty$, $C'_k \to C_k$.

The limiting values of δ in Eq. (20) give

$$\phi^{N\text{-SPA}}(N, \phi_0, 0) = \phi_0, \tag{25}$$

$$\phi^{N\text{-SPA}}(N, \phi_0, 1) = 1 - \left(1 - \frac{\phi_0}{N}\right)^N. \tag{26}$$

As the thermodynamic limit is approached, $\phi^{N\text{-SPA}} \xrightarrow{N\to\infty} \phi^{\text{RS-SPA}}$.

Multi-body interactions leading to clustered states, can drastically affect ϕ in the SPA model. To account for the indirect, multi-body induced effects, ζ must be used in place of δ. The general Kirkwood approximation for the k-th order correlation function in ζ-space is

$$g_k^{(\zeta)} = (\zeta(\delta))^{\frac{k(k-1)}{2}} \,. \tag{27}$$

The analog to the finite N-SPA expression, Eq. (20), for ϕ in ζ-space can thus be written as

$$\phi^{\zeta\text{-SPA}}(N, \phi_0, \zeta(\delta)) = -\sum_{k=1}^{N} \binom{N}{k} \frac{(-\phi_0)^k}{N^k} g_k^{(\zeta)}. \tag{28}$$

with the replacement from Eq. (27) serving to account for the overlaps between the particles. In application, the values of ζ can be calculated using either Eq. (11) or Eq. (12). We will refer to these as the ζ_{V}-SPA and the ζ_{L}-SPA, respectively.

2.4.2 Sequential Iteration Method

A more accurate expression for estimating ϕ was constructed in Ref. [31] through the sequential addition of particles to a hypercube with volume L^d. Although it was derived

for the one-dimensional case, all the arguments of this sequential iteration method (SIM) remain valid for systems of d-dimensional penetrable spheres with arbitrary dimension d. Within the SIM approximation, the occupied volume fraction

$$\phi^{\mathrm{SIM}}(N, \phi_0, \zeta(\delta)) = \phi^{(N)}, \tag{29}$$

remains a function of N, ϕ_0 and the penetration parameter δ (see Eq. (12) above). The RHS of Eq. 29 is the N-particle limit of the series of occupied volume fractions $\phi^{(n)}$ for n particles. Each such fraction can be written as

$$\phi^{(n)} = 1 - \prod_{i=1}^{n} Q^{(i)}\,, \tag{30}$$

where $Q^{(i)}$ is the conditional probability that a random point A not in the covering of the first $i-1$ particles is also not covered by the i-th particle. These probabilities are found as

$$Q^{(i)} = \sum_{k=0}^{i-1} \binom{i-1}{k} \zeta^{i-k-1}(1-\zeta)^k q_k, \tag{31}$$

where q_k is the probability that A remains a point in the void phase of an $i-1$ particle system after the i-th particle is added under the condition that the i-th particle has no overlap with at least k other particles.

For example, The probability that the first particle added to the system does not cover A is q_0. When a second particle is added, then there is a chance it "does not see" the first particle because the hard interaction is not activated. If there are only two particles in the system, then their pairwise penetration probability is δ. However, for the N-particle system, the overlapping probability must obey the many-body condition and, therefore, cannot simply be equated to δ. As discussed in Sec. 2.3, the actual penetration coefficient ζ from Eq. (12) must be used in place of δ to account for multi-body effects. Thus, the probability that the second particle can overlap the first one, and does not cover point A is (ζq_0). Alternatively, when the particles do see each other, as realized with probability $(1-\zeta)$, then these particles behave as hard particles. The probability that the point A is not covered by the second particle is denoted as q_1. The latter differs from q_0 because the hard interaction must be taken into account in the last case. Combining these two outcomes

gives the probability of A not being covered by the second particle,

$$Q^{(2)} = \zeta q_0 + (1-\zeta) q_1 \ . \tag{32}$$

Analogously, the probability that the third particle added to the system does not cover point A consists of three terms:

$$Q^{(3)} = \zeta^2 q_0 + 2\zeta(1-\zeta) q_1 + (1-\zeta)^2 q_2 \ , \tag{33}$$

where the first term is the probability that the hard interaction is not activated between the new and two previously placed particles, and the third particle does not cover point A; the second term is the probability that the hard interaction is activated between the third and one of two other particles, and the third particle does not cover point A; and the last term is the probability that the hard interaction is activated between the third and two other particles, and the third particle does not cover point A. As illustrated in Fig. 11, the general probability of A not being covered by the i-th particle is Q_i where q_k is the probability point A is not covered by a new added particle given k particles have already been placed in the system. This probability must be defined before the expression can be evaluated.

To determine the coefficients q_k, we note that at $\zeta(0) = 0$ the hard interactions are activated throughout the particles network, and the corresponding occupied volume fraction is

$$\phi^{(k)} = k v^{(d)} / L^d = k(1-q_0) \ . \tag{34}$$

where $v^{(d)}$ is the volume of a single sphere in dimension d, given by Eq. (4). On the other hand, for $\zeta(0) = 0$, $Q^{(i)} = q_{i-1}$, and

$$\phi^{(k)} = 1 - q_0 q_1 \cdots q_{k-1} \ . \tag{35}$$

Combining these results, one obtains

$$q_0 q_1 \cdots q_{k-1} = 1 - k(1-q_0) \ . \tag{36}$$

This relation allows one to express q_k via q_0:

$$q_k = \frac{q_0 q_1 \cdots q_k}{q_0 q_1 \cdots q_{k-1}} = \frac{1-(k+1)(1-q_0)}{1-k(1-q_0)} \ . \tag{37}$$

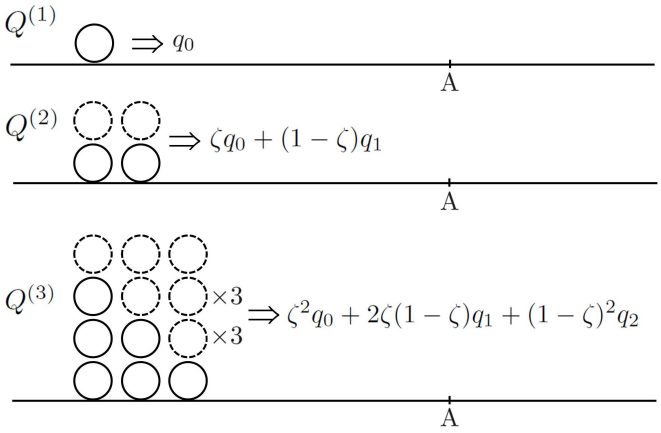

Figure 11: A graphical representation of how the first 3 terms in the SIM are constructed. The solid circles correspond to sets of particles that have an activated hard connection such as those represented by the red lines in Fig. 4. The dashed circles represent particle pairs that are not connected (allowed to penetrate through each other). For $Q^{(3)}$, the two middle configurations have 3 permutations that are each isomorphic.

Taking $\phi^{(k)}$ from Eq. (34), one can find that the recurrence relation reads

$$q_k = \frac{q_0 - \phi^{(k)}}{1 - \phi^{(k)}} \, . \tag{38}$$

where q_0 is the probability that the first particle added to the system does not cover the random point A:

$$q_0 = \frac{L^d - v^{(d)}}{L^d} = 1 - \frac{\phi_0}{N}. \tag{39}$$

Through Eqs. (13), (29), (30), (31), and (38) the expression for $\phi^{\mathrm{SIM}}(N, \phi_0, \zeta(\delta))$ can be evaluated giving

$$\phi^{\mathrm{SIM}}(N, \phi_0, \zeta(\delta)) = 1 - \prod_{i=1}^{N} \left(\sum_{k=0}^{i-1} \binom{i-1}{k} \zeta^{i-k-1} (1-\zeta)^k q_k \right) . \tag{40}$$

It gives the correct result in several limiting cases. For example, in the case of hard spheres, where $\delta = 0$, one obtains

$$\phi^{\mathrm{SIM}}(N, \phi_0, \zeta(0)) = 1 - q_0 q_1 \cdots q_{N-1} = \phi_0, \tag{41}$$

as one expects for the HC limit from Eq. (25). For fully transparent particles in the $\delta = 1$ limit, the occupied volume fraction is

$$\phi^{\mathrm{SIM}}(N, \phi_0, \zeta(1)) = 1 - q_0^N, \tag{42}$$

which is equal to the exact result given by Eq. (26). Thus, at limiting values of δ, the SIM expression is exact. We will refer to Eq. (40) as both the ζ_{V}-SIM and the ζ_{L}-SIM expression, depending on which ζ parameter is used in calculation.

2.5 Discussion

2.5.1 One Dimension

In one dimension, the dynamics are those of a system of rods moving on a line. Shown in Fig. 12 are the results for ϕ given by the N-SPA (20), ζ_{L}-SPA (28) and ζ_{L}-SIM (40) expressions. Note that for $d = 1$, $\zeta_{\mathrm{L}} = \zeta_{\mathrm{V}}$.

For dilute systems, ϕ is an approximately linear function of δ and all three analytic predictors give satisfactory results, interpolating approximately linearly between the completely hard ($\delta = 0$) limit and the completely soft Poisson distributed ($\delta = 1$) limit. As ϕ_0 is increased and the system becomes denser, a characteristic feature of ϕ in systems governed by bounded potentials can be seen. As can be seen in Fig. 12, when δ is reduced slightly from the ideal limit ($\delta = 1$) the response of ϕ is small and apparently linear. Contrast this to the case where δ is increased slightly from the HC limit ($\delta = 0$) and ϕ responds with a large decrease. The non-linear regime close to $\delta = 0$ is caused by the propensity for clusters to be in a completely overlapped state. A conjecture supported by Fig. 8 and Fig. 12 is that

$$\lim_{\phi_0 \to 1} \left. \frac{d\zeta_{\mathrm{L}}(\delta)}{d\delta} \right|_{\delta=0} = \infty \tag{43}$$

and

$$\lim_{\phi_0 \to 1} \left. \frac{d\phi(\delta)}{d\delta} \right|_{\delta=0} = -\infty. \tag{44}$$

These findings reveal another feature of the penetrable particles: at high density, even a subtle chance to overlap will unavoidably be realized. In higher-dimensional systems, we conjecture that it may even give rise to phase transitions. As δ is moved slightly from the $\delta = 0$ limit, ϕ decreases drastically due to pressure pushing the particles into overlapped states. In this regime, both the N-SPA and ζ_{L}-SPA expressions fail to agree with simulation results while the ζ_{L}-SIM expression shows excellent agreement. The error between the results measured from MD and ζ_{L}-SIM expression is $< 1.5\%$ over all values of ϕ_0 and δ. In

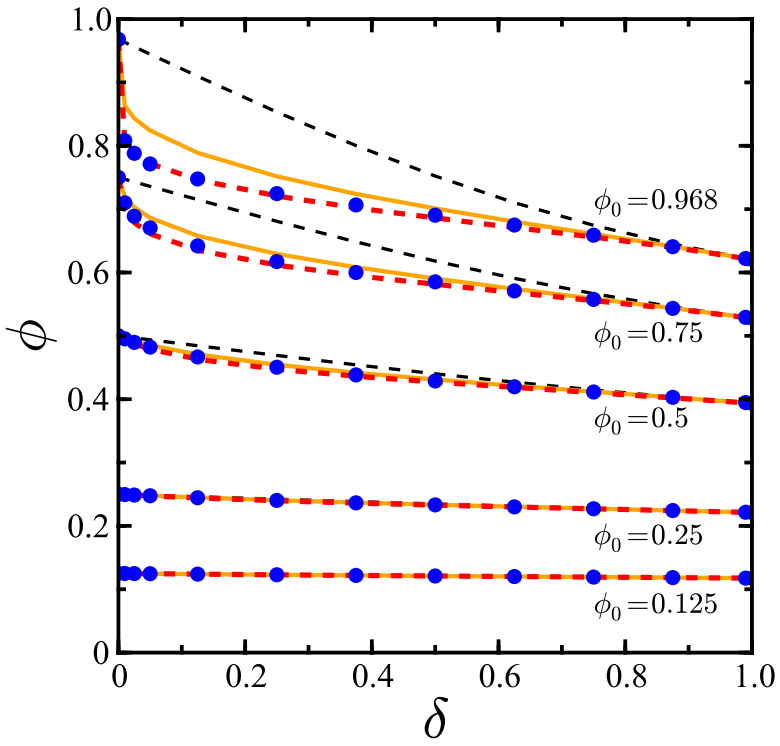

Figure 12: The occupied volume fraction ϕ as a function of the penetration probability parameter δ in one dimension ($d = 1$). The blue filled circles are the results of MD simulations. The result of the N-SPA expression, given by Eq. (20), is shown as a dashed black curve. The ζ_{L}-SPA expression, given by Eq. (28), is shown as a solid orange curve. The ζ_{L}-SIM result, given by Eq. (40), is shown as a dashed red curve.

comparison, the N-SPA expression gives error $> 20\%$ at large ϕ_0 and small δ.

2.5.2 Two Dimensions

The results for ϕ generated from simulation and analytic theory for a two-dimensional system of disks are shown in Fig. 13. The general trends are the same as in one dimension. When $\delta \neq 0$ the observed volume fraction is decreased from ϕ_0. This decrease is pronounced at high densities and small δ where overlapped states are favored as observed in the PR of $g_2(r;\delta)$ in Fig. 9. The N-SPA expression, which is shown only for $\phi_0 = 0.75$, fails in the large-ϕ_0, small-δ regime while both the ζ_{L}-SIM and the ζ_{L}-SPA expressions show agreement with the results measured from MD simulations across all ranges of ϕ_0 and δ studied. The ζ_{L}-SIM expression gives error in ϕ, with respect to values obtained from MD simulation, of $\approx 5\%$ at large ϕ_0 and small δ, with typical error $< 1\%$ outside of this regime. Interestingly,

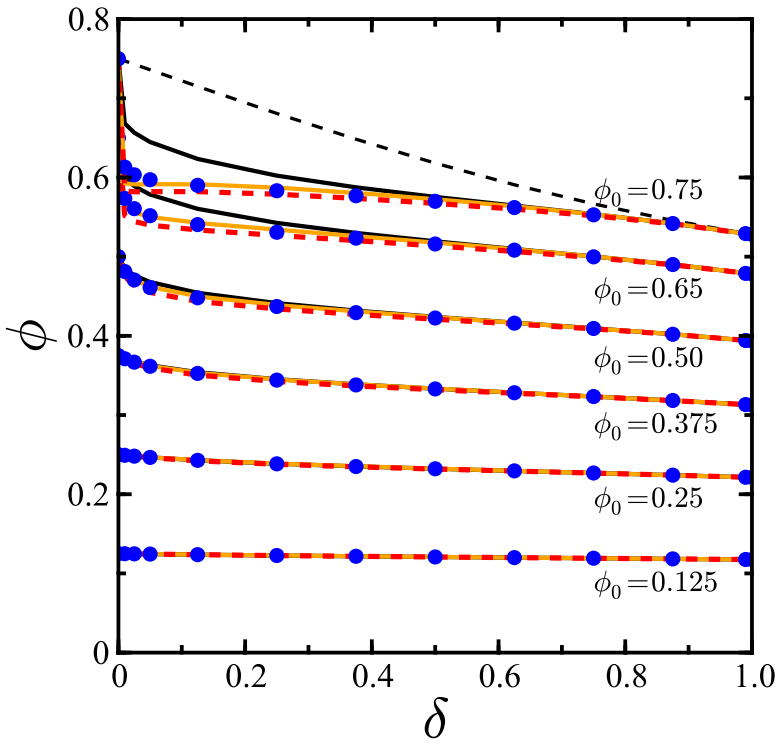

Figure 13: The occupied volume fraction ϕ as a function of the penetration probability parameter δ in two dimensions ($d = 2$). The labeling and symbols correspond to those in Fig. 12, with addition of the ζ_V-SIM result which is shown as a solid black curve. The result of the N-SPA expression (dashed black) is shown only for $\phi_0 = 0.75$.

the dimensionally-scaled ζ_V-SIM expression gives error $\approx 10\%$ at large ϕ_0 and small δ values. This error decreases significantly as δ is increased, but it is always greater than that given by the ζ_L-SIM expression, up to large δ values where the error in both expressions becomes negligible, typically $< 0.1\%$.

2.5.3 Three Dimensions

Figure 14 shows the results for ϕ measured from simulation and predicted by the analytic approaches of Sec. 2.4 for a system of three-dimensional spheres. At low to moderate densities $\phi_0 \in \{0.1, 0.2, 0.3\}$ the results from MD simulations agree with the ζ_V-SIM, ζ_L-SIM, and the ζ_L-SPA expressions across all ranges of δ. In this density regime, the error for all three expressions is $< 2\%$ at small δ values and is typically $< 1\%$ for $\delta \geq 0.25$.

At higher densities $\phi_0 \in \{0.4, 0.5\}$, close and above the HC freezing transition density ($\phi_0 \approx 0.491$), the theoretical predictions are in agreement with the MD results for large δ,

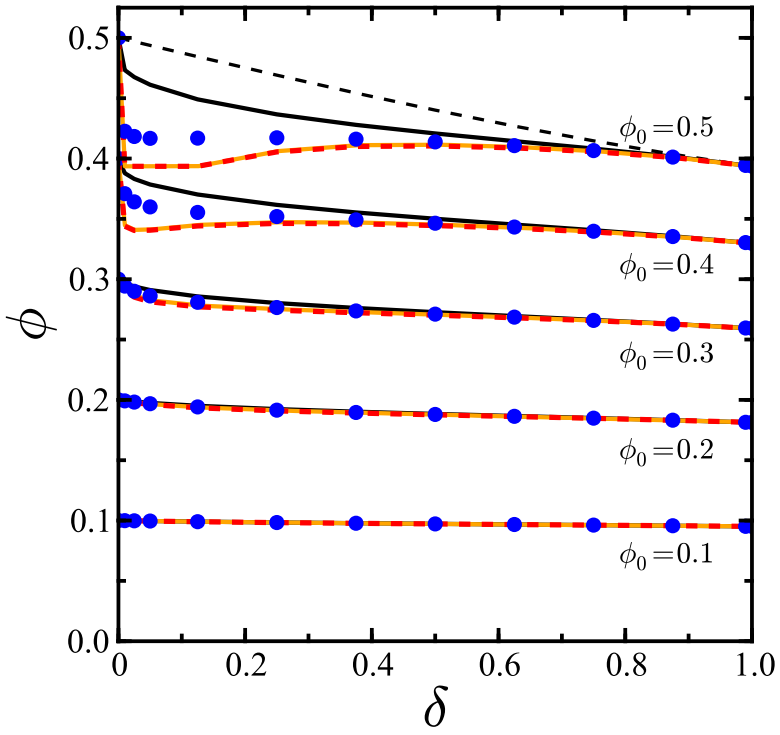

Figure 14: The occupied volume fraction ϕ as a function of the penetration probability parameter δ in three dimensions ($d = 3$). The labeling and symbols correspond to those in Fig. 13. The result of the N-SPA expression (dashed black) is shown only for $\phi_0 = 0.5$.

contrary to the case of small δ. The latter divergence is caused by a change in structure from an isotropic state to a crystal or clustered state. Note that when $\zeta_{\rm L} > 1$, which is shown in Fig. 8(c), the weighting of states in Eqs. (28) and (40) fails catastrophically. In this case we make the *ad hoc* correction that is $\zeta_{\rm L}$ bound above by $\zeta_{\rm L} = 1$. When clustering behavior dominates the structure of the system, it has been shown that for the deterministic PS potential (2) other analytic theories breakdown [198, 175]. In this regime, completely overlapped states are highly favored and theory based on assumptions of spatial uniformity would be expected to fail. At high densities we observe in systems governed by the stochastic potential (6) the same *"cluster anomaly"* found in the deterministic (GEM-n) model [27].

To characterize the anomalous clustered state, the dependence of the clustering probability on ϕ_0 was measured from MD simulations. Let $P_{\rm c}(i)$ denote the probability of a randomly chosen particle being connected by overlaps to i other particles, self-inclusive [198]. If the particle does not overlap with any other particles ($i = 1$) it is a monomer; two penetrating particles form a dimer ($i = 2$) given there is no other particle overlapping the former ones, *etc.*

The results are shown in Fig. 15. At $\delta = 0$, no particles overlap and the system consists entirely of monomers. At small δ and large ϕ_0 the most probable configuration is a dimer. The turnover from a state in which monomers are favored to a state in which the particles cluster and dimers are favored is the exact trend of clustering observed in the (GEM-n) model (c.f. Fig. 4 in Ref. [27]). For intermediate δ, higher order oligomers are formed and the distribution of clusters is Poisson-like as observed by comparing the middle and bottom panels of Fig. 15. For $\delta = 1$ the particles have no spatial correlation and are Poisson distributed.

The internal dimer radial distribution function $g_2^{\rm di}(r;\delta)$ gives the probability to find the second particle in a dimer at a distance r from the first particle. For $r > \sigma$, $g_2^{\rm di}(r;\delta) = 0$ as the two particles are not in a dimerized state in this case. In Fig. 16 the ratio $g_2^{\rm di}(r;\delta)/g_2^{\rm di}(\sigma^-;\delta)$ is shown for various δ values for $\phi_0 = 0.25$ and $\phi_0 = 0.5$. For $r \approx \sigma$, this ratio decreases because the cluster is more likely to be in a higher order oligomer due to the available volume for other particles to occupy. As r approaches 0, the particles become

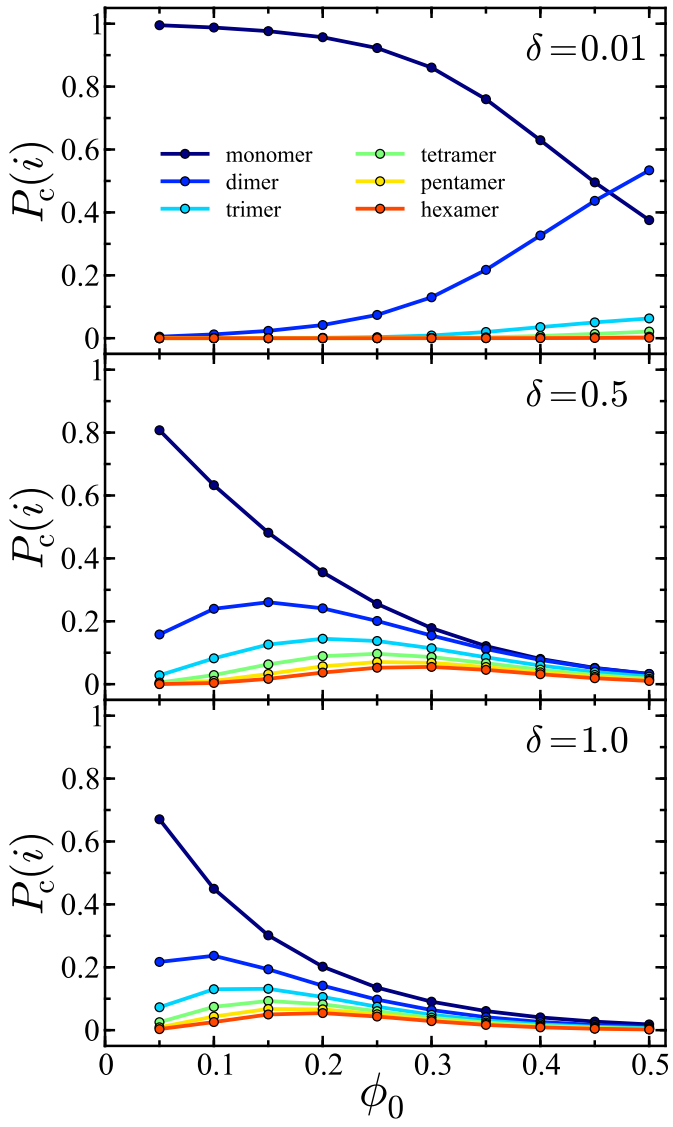

Figure 15: The clustering probabilities $P_c(i)$ of three-dimensional spheres as a function of ϕ_0 for $\delta = 0.01$ (top), $\delta = 0.5$ (middle), and $\delta = 1$ (bottom). Different values of i run from "monomer" ($i = 1$) to "hexamer" ($i = 6$) as indicated in the top panel. For each set of parameters $\{\phi_0, \delta\}$ the probabilities were calculated by integrating over 5×10^5 spatial configurations.

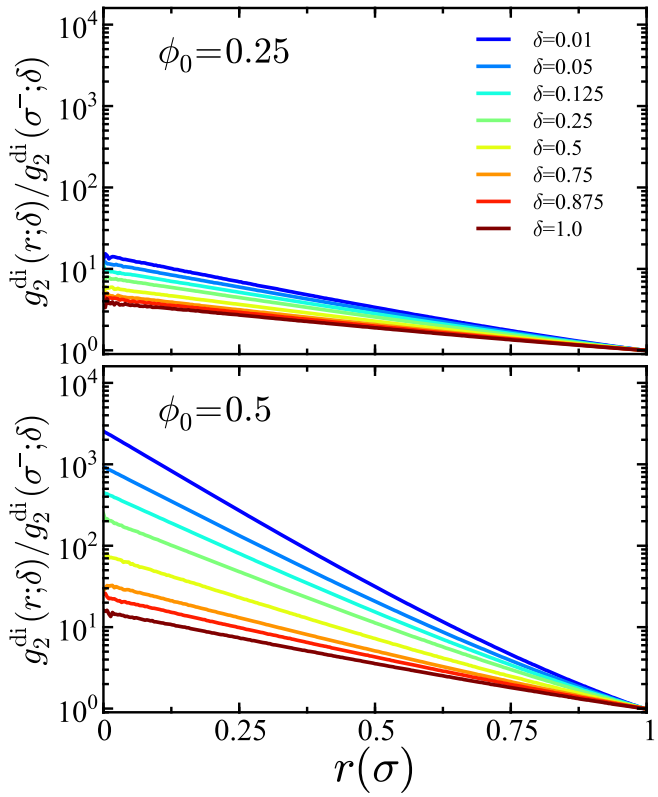

Figure 16: Semi-log plots of the scaled internal dimer $g_2^{\rm di}(r;\delta)/g_2^{\rm di}(\sigma^-;\delta)$ radial distribution functions for three-dimensional spheres at $\phi_0 = 0.25$ (top) and $\phi_0 = 0.5$ (bottom).

completely overlapped. At $\phi_0 = 0.25$ and $\delta = 0.01$, the ratio $g_2^{\rm di}(0;\delta)/g_2^{\rm di}(\sigma^-;\delta) \approx 15$ while at $\phi_0 = 0.5$ and $\delta = 0.01$ it jumps up to ~ 2500 indicating a large increase in propensity for the dimer to be in a highly overlapped state.

2.6 Conclusions

We have studied the static structures of a system of stochastically penetrable spheres through MD simulations and analytic theory in dimensions one, two, and three. In simulation, the interactions between particles are governed by a stochastic potential. This stochastic potential bridges hard-core and ideal behavior through a penetration parameter δ. The value of δ governs whether the particles are allowed to interpenetrate (overlap) or are completely hard. When the particles take on overlapping states, the volume occupied by the system is reduced. To predict the particle volume fraction, analytic theories

have been developed based on conditional probabilities derived from the sequential addition of particles to configuration space. The particle volume fraction has been measured from simulation and the results have been compared to the theoretical predictions. These results were found to be in excellent agreement apart from an observed clustered regime at high densities and small δ in three dimensions. We have characterized this regime through analysis of clustering probabilities and intracluster spatial distributions.

In one and two dimensions, over the densities studied, we see no conclusive evidence of a transition from an isotropic stable state to a cluster-forming regime where particles exist, and persist, in completely overlapped states. Trends in the effective occupied volume fraction ϕ suggest that these transitions could be observed as the density is increased toward the maximum hard-core packing fraction.

A qualitative comparison between the simulation results generated from deterministic bounded models and the presented stochastic bounded model has shown that the stochastic models capture the general behavior of their deterministic analogs. In particular, the collective effect of pairwise soft interactions appear to be characterizable through a single reduced parameter that captures their overlap probability. We further conjecture that the structural properties of deterministic bounded potentials can be exactly reproduced using stochastic models based on this one characteristic. The derivation of stochastically realized, non-Newtonian equations of motion for coarse-grained macromolecular dynamics is a focus of our current research.

CHAPTER III

EFFECTIVE SURFACE COVERAGE OF COARSE-GRAINED SOFT MATTER

3.1 Introduction

In the previous Chapter, a stochastic penetration algorithm (SPA) was introduced to model the structural behavior of systems of soft particles. Here, we present a lattice generalization of the SPA model and apply this model to a sequential adsorption process on a solid substrate. As represented in Fig. 17, the occupied volume fraction of the lattice model can be smoothly mapped to occupied volume fraction of an equilibrium system of particles moving on a continuum configuration space. The structures that emerge from overlapping spatial configurations, such as those generated by the SPA algorithm, render non-trivial geometries of the system's particle phase. This is in contrast to the atomistic scale in which nuclear repulsion does not allow for pairs of atoms to overlap, and thus mutually exclusive probabilistic arguments suffice to describe the resulting bulk phase structure. This overlapping phenomenon has been observed experimentally in the structure factor of dendrimers, measured with small-angle neutron scattering [155] in agreement with the theoretical predictions of Likos and co-workers [110, 5].

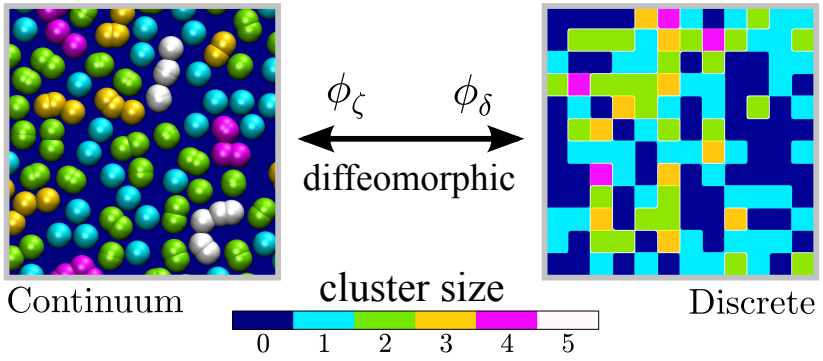

Figure 17: The lattice occupied volume fraction ϕ_δ and the continuum occupied volume fraction ϕ_ζ are connected through the invertible mapping $\delta \mapsto \zeta$.

The determination of the occupied volume fraction of a system's particle phase ϕ is of specific interest for the design of materials with properties driven by bulk phase connectivity, such as conductivity and permeability [184, 102, 176, 41, 175, 31, 30]. The attainable particle phase volume fraction in systems consisting of soft macromolecular structures is much larger than that of systems governed by hard core (HC) potentials [127]. In simple HC models, such as the well known hard sphere system [181], the infinite value of the governing potentials prohibits a set of particles from overlapping. When coarse-grained intermolecular interactions are modeled using bounded potentials, an increase in attainable volume fractions gives rise to complex clustering behavior [110, 135, 134, 210, 27], as the particles are allowed to overlap relative to their characteristic radius of gyration.

The assembly of particles on a substrate that are prohibited from overlapping because of steric repulsion is often modeled using random sequential adsorption (RSA) [48]. In the RSA procedure, particles are deposited sequentially, with the position of the incident particle chosen at random. If the placement of an incident particle on the chosen position leads to overlap with any previously added particle, the particle does not bind to the substrate. The insertion of non-overlapping objects to a volume generates non-equilibrium structures that differ from the configurations generated by HC systems in thermodynamic equilibrium [203, 185]. By forming geometrical objects through combinations of identical spheres, RSA can be extended to polymeric structures [23, 24].

The RSA can be further generalized through the random site model (RSM) by subdividing the substrate into a random distribution of discretized binding sites [83, 178]. The occupied fraction of independent discrete sites, when only monolayers are allowed, can then be obtained from the standard Langmuir isotherm [98]. Multi-layer coverage and distributions in reversible equilibrium adsorption processes can be addressed through the BET (Brunauer, Emmett, and Teller) isotherm [19] as long as adsorbate-adsorbate interactions are ignorable [126].

In the deposition of coarse-grained macromolecules on a surface, there is a possibility for them to occupy the same binding site at a finite energy cost, and this can be addressed

even within interaction models that involve bounded potentials. The single occupancy criterion of the RSM and the Langmuir isotherm does not sufficiently describe the complexity of the generated structures with such multiple occupancy. Multilayer isotherms built on assumptions involving bulk-phase interactions and the independence of each monolayer also fail. Finken *et al.* [51] and Likos *et al.* [113] have developed multiple occupancy lattice models to study the phase behavior of coarse-grained macromolecules through evaluation of approximated partition functions. These studies have elucidated both phase separations and the transition to clustering regimes in equilibrium CG systems, but they are not directly applicable to the prediction of structures generated from sequential addition processes.

The self-organization of cells on microstructured surfaces is another example of an observed multiple occupancy phenomenon. Binding sites are created by coating a substrate with protein. A cell line is introduced to the substrate and the cells self-organize on the binding sites. After organization, a fraction of lattice sites will be occupied by multiple cells [162]. Multiple occupancy is advantageous for processes in which cell-to-cell communication drives survival and function [114] but also a hindrance to the creation of single cell assays.

In this Chapter, we use an avoidance-modified soft sequential adsorption (SSA) algorithm to model coarse-grained macromolecules binding to a substrate. It takes advantage of our recent model [31, 30] treating soft (penetrable) interactions using stochastic hard-sphere potentials. In the SSA process, purely repulsive pairwise interactions drive the assembly, and the bounded nature of the underlying potential allows multiple molecular structures to occupy the same binding site. Simulations and a new theoretical framework of the SSA process provide the fraction of occupied binding sites ϕ and the distribution of occupied sites. For systems at the thermodynamic limit, we derive ϕ using mean field (MF) arguments and compare both the exact and MF results with measurements taken from Monte Carlo (MC) simulations, with excellent agreement observed. These expressions are applied to a system governed by a stochastic bounded potential that includes multi-body interactions. We find that using the exact SSA derivation of ϕ, we can predict the occupied volume fraction of equilibrium configurations of coarse-grained, penetrable systems. The occupied volume fraction also differs from what is observed in the case of relaxed surface coverage

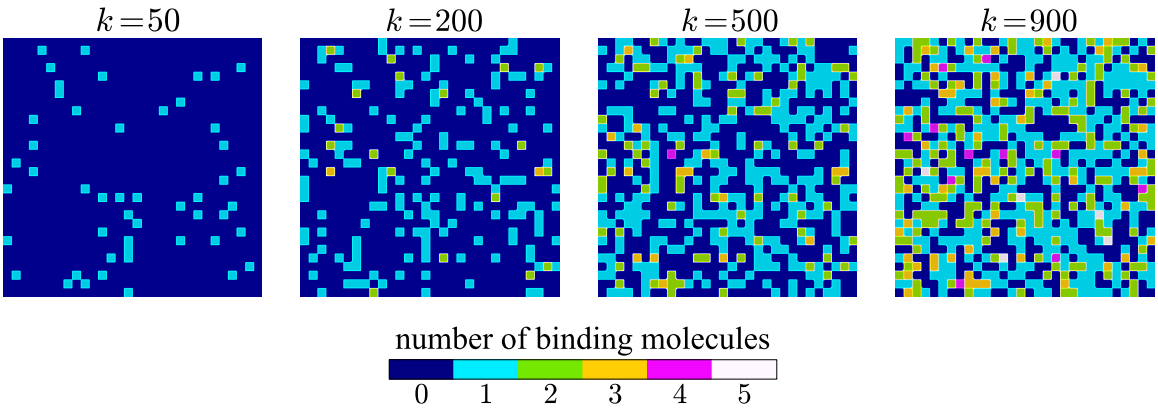

Figure 18: Several configurations generated as $k = 900$ macromolecules are sequentially added to solid substrate with $n = 900$ binding sites. The softness parameter is $\delta = 1$. Each binding site is colored according to the number of particles that occupy that site. The configurations shown are progressive; each configuration c is built from the one before $c_{50} \to c_{200} \to c_{500} \to c_{900}$.

(RSC), that is, when the particles are allowed to move between binding sites upon SSA.

3.2 Soft Sequential Adsorption (SSA)

We consider a substrate with n discrete binding sites and k incident macromolecules, which arrive sequentially, and bind irreversibly to the substrate. The potential between a pair of macromolecules, i and j, is described by

$$V(r_{ij}) = \begin{cases} \epsilon, & r_{ij} = 0 \ , \\ 0, & \text{otherwise} \ , \end{cases} \tag{45}$$

which is ϵ if the pair of macromolecules occupies the same site on the substrate and 0 otherwise. A potential of this form is a lattice generalization of the the well-known penetrable sphere (PS) potential [166, 122, 123, 22, 198] introduced by Marquest and Whitten [124], in order to model solutions of micelles.

Through the introduction of a Boltzmann weighted softness parameter

$$\delta = e^{-\epsilon^\star}, \tag{46}$$

with $\epsilon^\star = \epsilon / k_{\mathrm{B}} T$, the softness of the underlying potential can be reduced to one parameter. The limiting values of this parameter classify the adsorbant as completely hard ($\delta = 0$), when no multiple occupancy is allowed, and completely soft ($\delta = 1$) when macromolecules

are allowed to occupy the same binding site. For a particular system, the actual value of δ would depend on, for example, the critical adsorption point, internal structure, orientation, and chain-length of the incident species [108, 131]. At intermediate values, $0 < \delta < 1$, complex structures are generated through the non-Markovian, avoidance-modified SSA algorithm, which is implemented as follows:

1. *A substrate with n binding sites is created and a value of the softness parameter $\delta \in [0, 1]$ is preassigned to the incident binding macromolecules.*

2. *A macromolecule is created and a binding site on the substrate is selected randomly from a uniform distribution.*

3. *If the binding site is unoccupied, the macromolecule irreversibly adsorbs to the selected site. Bound macromolecules do not diffuse on the surface or desorb from the surface.*

4. *If the binding site is already occupied by $i > 0$ macromolecules, the macromolecule irreversibly adsorbs to the selected site with probability δ^i and is rejected from the site with probability $(1 - \delta^i)$.*

5. *If the macromolecule is rejected from the binding site, a new binding site on the substrate is selected randomly, with all sites having equal probability of being selected, and the acceptance loop (Steps 3-4) is repeated*

The sequential creation-acceptance process is repeated until k macromolecules are added to the substrate. After the sequential addition of macromolecules, the substrate will have some number of occupied and unoccupied sites. The occupied volume fraction ϕ is the average number of occupied binding sites, i.e., the surface coverage concentration.

The number of possible microstates for a lattice system that allows multiple occupancy, where both the macromolecules and binding sites are distinguishable, is n^k. The energy of the system

$$E = \sum_{i=1}^{k} \sum_{i>j} V(r_{ij}), \tag{47}$$

is characterized entirely by the intermolecular interactions. It is notable that the distribution of energy states generated by sequential addition methods cannot be equated to the probabilistic distribution of the canonical Boltzmann partition function [203].

In this article, we will derive methods to predict the weighting of microstates that arise from the SSA procedure. Through calculation of the microstate weighting, either exactly or through approximate methods, spatial properties of a system undergoing SSA, such as ϕ, can be elucidated analytically.

For completely hard ($\delta = 0$) macromolecules, ϕ is trivially

$$\phi_0 = \frac{k}{n}, \tag{48}$$

where the number of binding macromolecule is bounded above by $k = n$, as at this limit there are no available binding sites for a $k + 1$ incident macromolecule. For soft ($\delta > 0$) interactions, multiple macromolecules can occupy the same binding site and ϕ_0 is an upper bound to the actual volume fraction ϕ, *i.e.*, $\phi \leq \phi_0$. Note that when $k > n$ the surface coverage concentration ϕ, which is the expectation value of ratio of occupied binding sites to total binding sites, cannot exceed unity. At the $\delta = 1$ limit, the occupancy follows a binomial distribution

$$\begin{aligned} \phi &= 1 - \left(1 + \sum_{i=1}^{k} \binom{k}{i} \frac{(-\phi_0)^i}{k^i} \right) \\ &= 1 - \left(1 - \frac{\phi_0}{k} \right)^k, \end{aligned} \tag{49}$$

which is bounded above by $\phi = 1$. In the limit ($k \to \infty, n \to \infty$), Eq. (49) can be replaced with well-known Poisson distributed result [157, 182],

$$\phi = 1 - e^{-\phi_0}, \tag{50}$$

which is the volume fraction occupied by macromolecules that overlap with no energy cost at the thermodynamic limit. Figure 18 shows selected configurations generated as macromolecules are sequentially added to binding sites with $\delta = 1$. The softness of the macromolecules allows multiple occupancy of a binding site and causes a decrease in the occupied volume fraction with respect to ϕ_0.

At intermediate softness, $0 < \delta < 1$, the pairwise interactions generate complex behavior in ϕ. In the following two sections of this article, we will derive two expressions to predict the volume of a substrate occupied by an incident molecular species undergoing SSA.

3.3 Exact Occupied Volume Fraction

Consider the sequential addition of k macromolecules added to a substrate with n binding sites. As the particles arrive to the substrate, the probability of selection for a specific site is $1/n$. In the non-trivial $\delta > 0$ regime, after the sequential addition of k macromolecules, the configurations of occupied sites that can be generated are given by the integer partitions $\{\nu_k\}$ of k. Kindt has developed theory to predict the equilibrium cluster size distribution of aggregating monomers using compositions of integers and separable partition functions [91], and we modify his notation for our study. The partitions $\{\nu_k\}$ define a distinct set of occupied configurations (OC) that can be generated. For example, after the addition of 3 macromolecules the allowed OC are $\{\nu_3\}_1 = \{1,1,1\}$, $\{\nu_3\}_2 = \{2,1\}$, and $\{\nu_3\}_3 = \{3\}$ (note that $\{2,1\} = \{1,2\}$). In general, the occupied binding sites take on configurations $\{\nu_k\}_i$ where $i \in \{1,2,\ldots,p(k)\}$ and $p(k)$ is the number of partitions for the integer k. An estimation of $p(k)$ [68], for large k, is

$$p(k) \approx \frac{1}{4k\sqrt{3}}\, e^{\pi\sqrt{2k/3}}. \tag{51}$$

Figure 19 shows the event graph $\mathcal{G}$, encompassing all possible OC that can be generated, for the sequential addition of $k = 4$ macromolecules. The first macromolecule k_0 added to the system must axiomatically bind to an unoccupied site and thus generate $\{\nu_1\}_1 = \{1\}$. This event is marked by letter "U" in Fig. 19. The second macromolecule k_1 can either bind to an unoccupied site (U) generating $\{\nu_2\}_1 = \{1,1\}$, bind to the site occupied by the first macromolecule (event "O_1") generating $\{\nu_2\}_2 = \{2\}$, or be rejected by the site occupied by the first macromolecule (event "$\overline{O}_1$"). If macromolecule k_1 is rejected from the substrate, a new round of acceptance-rejection is begun, thus the only possible final states for k_1 are O_1 and U. Excluding the intermediate rejection outcomes, the third macromolecule k_2 has three possible final states. If the substrate is in configuration $\{\nu_2\}_1$, the macromolecule can bind to an unoccupied site (U) generating $\{\nu_3\}_1 = \{1,1,1\}$ or

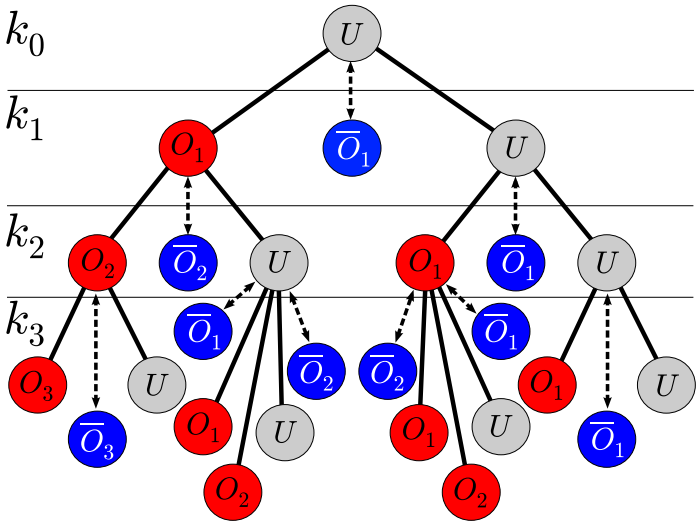

Figure 19: The avoidance-modified event graph $\mathcal{G}$ for the sequential addition $k_0 \rightarrow k_1 \rightarrow k_2 \rightarrow k_3$ of four macromolecules added to a solid substrate. The symbol O_i (red) represents that the macromolecule is accepted onto a binding site occupied by i macromolecules and $\overline{O}_i$ (blue) represents that the macromolecule is rejected from a site occupied by i macromolecules. In the event of rejection, a new site is selected, without memory, and the acceptance-avoidance site selection is repeated. Rejection events are shown as a directed dashed lines. An acceptance of the macromolecule by an unoccupied site is represented by U (gray).

be accepted by either of the two occupied sites (O_1) generating $\{\nu_3\}_2 = \{2, 1\}$. If the substrate is in configuration $\{\nu_2\}_2$, the macromolecule can bind to an unoccupied site (U) generating $\{\nu_3\}_2 = \{2, 1\}$ or be accepted by the site doubly occupied by the previously added macromolecules (O_2) generating $\{\nu_3\}_3 = \{3\}$. As illustrated in Fig. 19, the fourth macromolecule k_3 has an increased complexity of available final states, which have a non-Markovian property, depending on all the previous states and on the possible intermediate rejection outcomes.

Let $\{\omega_k\}_i$ represent the occupancy vector of the partition $\{\nu_k\}_i$,

$$\{\omega_k\}_i = \{o_1, o_2, o_3, \ldots, o_k\}\,, \tag{52}$$

where o_l is the number of sites with l bound macromolecules. For $k = 3$, the occupancy vectors are $\{\omega_3\}_1 = \{3, 0, 0\}$, $\{\omega_3\}_2 = \{1, 1, 0\}$, and $\{\omega_3\}_3 = \{0, 0, 1\}$. Coupled with the

softness parameter δ, the occupancy vector defines a state polynomial,

$$S(\{\omega_k\}_i, \delta) = \sum_{l=1}^{k} o_l \, \delta^l. \tag{53}$$

The normalized state polynomial

$$P_1\big(O \,\big|\, \{\nu_k\}_i\big) = \frac{1}{n} S(\{\omega_k\}_i, \delta), \tag{54}$$

is the probability for the incident macromolecule to be accepted into any *occupied* state (event "O"), on the first round of acceptance-rejection, given that the OC of the substrate is $\{\nu_k\}_i$. Let $P_1\big(\overline{O} \,\big|\, \{\nu_k\}_i\big)$ denote the conditional probability that the incident macromolecule is rejected by the substrate on the first round of acceptance-rejection, given that the OC of the substrate is $\{\nu_k\}_i$:

$$P_1\big(\overline{O} \,\big|\, \{\nu_k\}_i\big) = \sum_{l=1}^{k} \frac{o_l}{n} \, (1 - \delta^l), \tag{55}$$

The probability of acceptance or rejection is the same for every round, but the probability to reach that round depends on the outcome of all previous rounds, *e.g.*, the incident macromolecule can be accepted on the first round, rejected on the first round and accepted on the second, rejected on the first and second and accepted on the third. This sequence continues *ad infinitum*, with each term in the sum representing a successive round of acceptance-rejection. The series is geometric, and thus the evaluated sum can be expressed as

$$P\big(O \,\big|\, \{\nu_k\}_i\big) = P_1\big(O \,\big|\, \{\nu_k\}_i\big) \, \frac{1}{1 - P_1\big(\overline{O} \,\big|\, \{\nu_k\}_i\big)}. \tag{56}$$

The conditional probability for an incident macromolecule to bind to any occupied site given that the substrate is in configuration $\{\nu_k\}_i$ can be expressed through the state polynomials, (Eqs. (53) and (54)),

$$\begin{aligned} P\big(O \,\big|\, \{\nu_k\}_i\big) &= \left(\frac{1}{n} \sum_{i=1}^{k} o_i \, \delta^i\right) \frac{1}{1 - \dfrac{1}{n} \displaystyle\sum_{i=1}^{k} o_i \, (1 - \delta^i)} \\ &= \frac{S(\{\omega_k\}_i, \delta)}{n - k + S(\{\omega_k\}_i, \delta)}. \end{aligned} \tag{57}$$

Accounting for all outcomes, the conditional probability to bind to an unoccupied site is

$$P\big(U \,\big|\, \{\nu_k\}_i\big) = 1 - P\big(O \,\big|\, \{\nu_k\}_i\big). \tag{58}$$

The probability given by Eq. (57) is a sum of the probabilities to bind to each occupied site j (event "O_j"),

$$P\big(O \,\big|\, \{\nu_k\}_i\big) = \sum_{j=1}^{k} P\big(O_j \big|\, \{\nu_k\}_i\big)\,, \tag{59}$$

and thus the conditional probability for the $k+1$ macromolecule to bind to a site occupied by j macromolecules is

$$P\big(O_j \,\big|\, \{\nu_k\}_i\big) = \frac{o_j\, \delta^j}{n-k+S(\{\omega_k\}_i\,,\delta)}. \tag{60}$$

The transition $\{\nu_k\}_i \to O_j$ or $\{\nu_k\}_i \to U$ generates a distinct partition $\{\nu_{k+1}\}_l$ of the $k+1$ integer and thus the index l depends on j and must be included as an argument, $l = l(j)$. The index set $\{i, l\}$ defines a distinct node-to-node transition and we arrive at the expression for the conditional probability that the $k+1$ macromolecule added to the system generates the $\{\nu_{k+1}\}_{l(j)}$ partition, given that the previous k macromolecules are in the OC defined by $\{\nu_k\}_i$,

$$P_T\Big(\{\nu_{k+1}\}_{l(j)} \,\Big|\, \{\nu_k\}_i\Big) = \frac{o_j\, \delta^j}{n-k+S(\{\omega_k\}_i\,,\delta)}, \tag{61}$$

if the $k+1$ macromolecule binds to an occupied site, or

$$P_T\Big(\{\nu_{k+1}\}_{l(j)} \,\Big|\, \{\nu_k\}_i\Big) = 1 - \frac{S(\{\omega_k\}_i\,,\delta)}{n-k+S(\{\omega_k\}_i\,,\delta)}, \tag{62}$$

if the $k+1$ macromolecule binds to an unoccupied site.

Let $\mathcal{P}$ denote all the possible transition paths on the graph $\mathcal{G}$. A subset of $\mathcal{P}$ is $\mathcal{P}_i$ which is all the paths terminating at the configuration defined by the $\{\nu_k\}_i$-th integer partition of k. The index set $\alpha = \{\alpha_1, \alpha_2, \ldots, \alpha_k\}$ is a subset of $\mathcal{P}_i$ and defines a specific path leading from the $\{\nu_1\}_1$ node to the $\{\nu_k\}_i$-th node. The transition probability along a specific path α is the product of all the conditional node-to-node transition probabilities P_T on that path,

$$P_\alpha(\delta) = \prod_{j=1}^{k-1} P_T\Big(\{\nu_{j+1}\}_{\alpha_{j+1}} \big|\, \{\nu_j\}_{\alpha_j}\Big)\,, \tag{63}$$

The probability $P_\alpha(\delta)$ is a function of δ the softness parameter. A change in δ will alter the probability of a node-to-node transition in accordance with Eq. (57).

There are many such paths $\alpha \in \mathcal{P}_i$ and thus the probability to reach the $\{\nu_k\}_i$-th state is the sum over all paths in $\mathcal{P}_i$,

$$P(\{\nu_k\}_i) = \sum_{\alpha \in \mathcal{P}_i} \prod_{j=1}^{k-1} P_T\Big(\{\nu_{j+1}\}_{\alpha_{j+1}} \big| \{\nu_j\}_{\alpha_j}\Big). \tag{64}$$

Equation (64) gives the probability to observe any configuration $\{\nu_k\}_i$.

The fraction of substrate binding sites occupied by $\{\nu_k\}_i$ depends on its size. Let $\lambda(\{\nu_k\}_i)$ be a function that takes a partition as its argument and returns the size of that partition. The occupied volume fraction of the i-th partition is

$$\Phi(\{\nu_k\}_i) = \frac{\lambda(\{\nu_k\}_i)}{n}, \tag{65}$$

which we enforce to be bounded from above at $\Phi = 1$. Combining Eqs. (64) and (65) we obtain,

$$\phi = \sum_{i=1}^{p(k)} \Phi(\{\nu_k\}_i) \left\{ \sum_{\alpha \in \mathcal{P}_i}^{\mathcal{P}_i \subseteq \mathcal{P}} \left(\prod_{j=1}^{k-1} P_T\Big(\{\nu_{j+1}\}_{\alpha_{j+1}} \big| \{\nu_j\}_{\alpha_j}\Big) \right) \right\}, \tag{66}$$

which is the exact probability for a binding site to be occupied after the sequential addition of k macromolecules to n binding sites.

Shown in Fig. 20 are the results for ϕ, given by Eq. (66), as a function of δ for various values of ϕ_0. For large ϕ_0 and small δ, ϕ is observed to rapidly decrease due to propensity for macromolecules to multiply occupy a site. The results from Monte Carlo (MC) simulations are shown as blue circular markers in Fig. 20. The MC results for ϕ agree with those given by Eq. (66).

The site occupation distribution $\mathrm{P}_X(x)$ can also be constructed from Eq. (64), where $x = 0$ corresponds to an unoccupied site, $x = 1$ is a site with one binding macromolecule, etc. For $x \geq 1$ this probability is

$$\mathrm{P}_X(x) = \frac{1}{n} \sum_{i=1}^{p(k)} P(\{\nu_k\}_i)\, o_x \tag{67}$$

where o_x is the x-th element of the occupancy vector for the partition $\{\nu_k\}_i$, defined by Eq. (52). The probability to observe an unoccupied site ($x = 0$) is

$$\begin{aligned} \mathrm{P}_X(0) &= 1 - \sum_{i=1}^{k} \mathrm{P}_X(i) \\ &= 1 - \phi, \end{aligned} \tag{68}$$

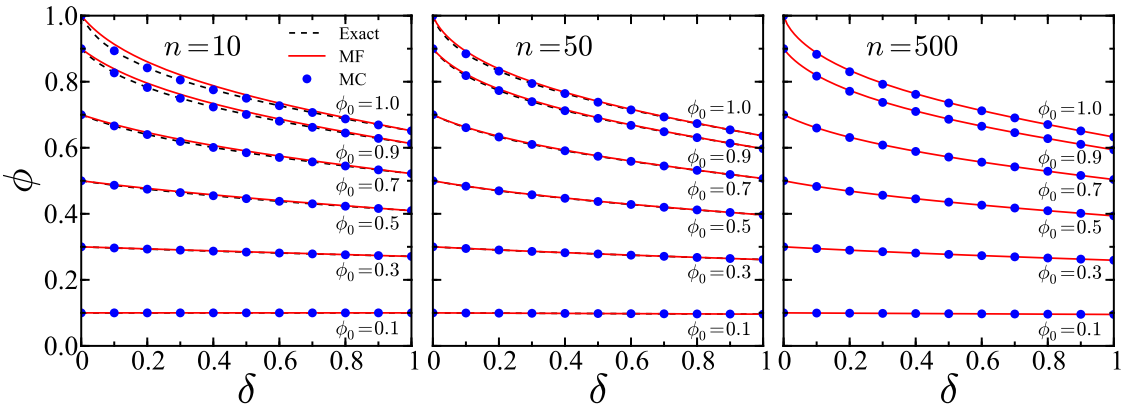

Figure 20: The fraction of occupied sites ϕ for different lattice sizes $n \in \{10, 50, 500\}$ from left to right, respectively, as a function of the softness parameter δ. The results for each lattice size are shown for various $\phi_0 = k/n$ values. Each circular marker (blue) is the the result calculated from 10^6 Monte Carlo (MC) simulations. The exact solution given by Eq. (66), for each value of ϕ_0, is shown as a dashed curve (black). The results predicted by the continuum mean field (MF) approximation, given by Eq. (72) and presented in the next section, Section 3.4, are shown as solid curves (red).

which is the remaining outcome after the probability for all occupied states has been counted.

Figure 21 shows the results for the distributions given by $P_X(x)$ as a function of ϕ_0 for various δ values. For $\delta = 0$ the system is completely hard and consists only of unoccupied and singly occupied sites. At $\delta = 0.025$ multiply occupied sites are allowed and the distribution is highly peaked as system enters clustering regimes at large ϕ_0. As δ is increased, sites that are multiply occupied become more probable and the distribution moves from a Poisson-like distribution at $\delta = 0.5$ to the exactly Poisson distribution at $\delta = 1$. Thus, the occupancy distributions can be separated into four regimes: The singly-occupied HC limit at $\delta = 0$, the clustering regime at small δ, the Poisson-like regime at intermediate δ, and the exactly Poissonian limit at $\delta = 1$.

The scaling of $p(k)$ can be estimated by Eq. (51). As $(k \to \infty, n \to \infty)$ the exact expression for ϕ, given by Eq. (66), becomes intractable due to the large number of partitions that must accounted for in the calculation. Although, as shown in Fig. 20, the values of ϕ at the thermodynamic limit are approached asymptotically, and the exact expression for ϕ gives a method to estimate ϕ for large k.

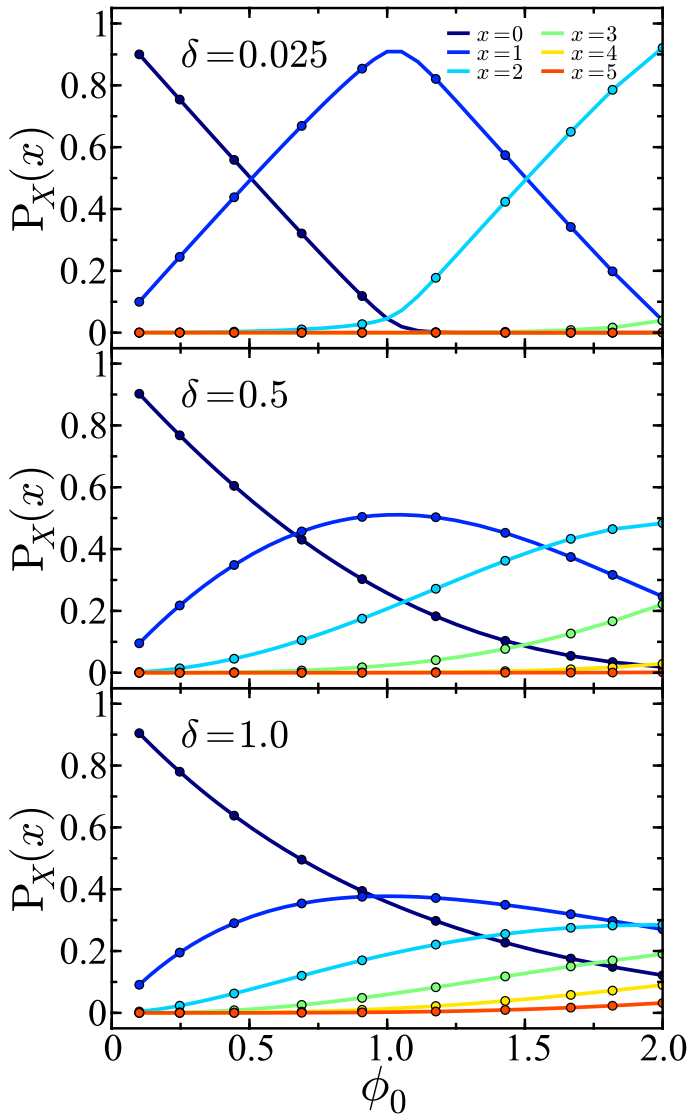

Figure 21: The distribution of site occupation $\mathrm{P}_X(x)$ for $k = 20$ macromolecules as function of ϕ_0. The exact results, given by Eqs. (67) and (68), for $\delta = 0.025$ (top), $\delta = 0.5$ (middle), and $\delta = 1$ (bottom) are shown as solid curves. Each circular markers is the result of 10^6 MC simulations.

3.4 Mean Field Occupancy

In this Section, we derive an expression built on MF arguments for the conditional probabilities to find multiply occupied sites. Herein, we refer to this approximation simply as the MF method. We have previously shown that expressions built on MF arguments can be used to accurately predict ϕ in off-lattice models where the dynamics are governed by stochastic bounded potentials. We will generalize the MF expression for a system undergoing SSA as follows:

Let $Q^{(i)}$ denote the conditional probability that the i-th macromolecule added to system, does not bind to a random site n_{R} given that $i-1$ macromolecules have already been added. The occupied volume fraction after adding k macromolecules can be found as

$$\phi^{(k)} = 1 - \prod_{i=1}^{k} Q^{(i)}. \tag{69}$$

The general probability of site n_{R} not being covered by the i-th particle accounting for all possible configurations (single and multiple occupancy sites) of the previously added $i-1$ macromolecules is

$$Q^{(i)} = \sum_{j=0}^{i-1} \binom{i-1}{j} \delta^{i-j-1}(1-\delta)^{j} q_j. \tag{70}$$

The binomial coefficient $\binom{i-1}{j}$ counts the possible permutations of the j-th configuration. The connection permutation probability q_j is the probability site n_{R} is not occupied by a newly added macromolecule given j macromolecules have already been placed in the system and that the the newly added macromolecule interacts with the previously added macromolecules through the j-th permutation of the interaction network. We find using MF arguments [31]:

$$q_j = \frac{q_0 - \phi^{(j)}}{1 - \phi^{(j)}}, \tag{71}$$

with $q_0 = 1 - 1/n$. The conditional probability q_j accounts for each sequentially added macromolecule having a reduced number of binding sites available, with respect to those previously added. Only in the $\delta = 1$ limit is the available volume not reduced as every macromolecule is completely independent. Through Eqs. (70) and (71), ϕ can be expressed

as

$$\phi^{\mathrm{MF}}(k,\delta) = 1 - \prod_{i=1}^{k}\left(\sum_{j=0}^{i-1}\binom{i-1}{j}\delta^{i-j-1}(1-\delta)^{j}q_j\right). \tag{72}$$

Equation (72) connects ϕ with the softness parameter δ. In the limiting values cases, $\delta = 0$ and $\delta = 1$, it leads to the exact results given by Eqs (48) and (49), respectively.

The results of the MF approximation are shown in Fig. 20. For small n, the MF method slightly overestimates ϕ. As the thermodynamic limit is approached ($k \to \infty, n \to \infty$) the MF method agrees with the exact result, given by Eq. (66), and with results obtained from MC simulations across all ranges of δ and ϕ_0.

3.5 Relaxed Surface Coverage (RSC) vs. SSA

The creation-rejection-acceptance algorithm used to model sequential adsorption of macromolecules in the SSA procedure generates a distribution of energetic states, and hence spatial configurations, that are constrained to remain in place once trapped. This distribution will necessarily differ from the canonical Boltzmann distribution of states that results when the macromolecules are allowed to relax between sites after adsorption resulting in relaxed surface coverage. In this Section, we will derive the equilibrium RSC distribution, use this distribution to calculate the equilibrium value of ϕ on a lattice, and compare this result with that generated from SSA. In a straightforward manner, we will first calculate the canonical partition function $Z(k, n, \beta)$ and use this to calculate the probability of observing a given state. The resulting equilibrium occupied volume fraction can be obtained through the assignment of the Boltzmann-weighted probability to the occupied volume fraction of each corresponding state.

We extend the notation of Section 3.3 through the introduction of extended integer partitions, wherein the $\{\nu_k\}_i$-th partition is appended with zeros such that the length of each extended partition $\{\mu_k\}_i$ is equal to n, i.e., $\lambda(\{\mu_k\}_i) = n$. For example, for $k = 3$ macromolecules binding to $n = 5$ sites, the allowed OC in the extended partition space are $\{\mu_3\}_1 = \{1,1,1,0,0\}$, $\{\mu_3\}_2 = \{2,1,0,0,0\}$, and $\{\mu_3\}_3 = \{3,0,0,0,0\}$ (c.f. the OC described in Section 3.3). We denote the j-th element of the i-th extended partition for the integer k as $\{\mu_k\}_i^j$.

The total number of overlapping contacts for each allowed OC, irrespective of the distribution (equilibrium or non-equilibrium), is given by

$$\mathcal{E}_i\left(\{\mu_k\}_i\right) = \frac{1}{2}\sum_{j=1}^{\lambda\left(\{\nu_k\}_i\right)} \{\mu_k\}_i^j \left(\{\mu_k\}_i^j - 1\right). \tag{73}$$

As the energy is pairwise additive, it is proportional to this quantity, *i.e.*, E_i is given by $\epsilon\mathcal{E}_i\left(\{\mu_k\}_i\right)$ for the i-th level. For $k \leq n$ the canonical partition function is

$$Z(k,n,\beta) = \sum_{i=1}^{p(k)} g_i(\{\mu_k\}_i)\, e^{-\beta\epsilon\mathcal{E}_i\left(\{\mu_k\}_i\right)}, \tag{74}$$

where g_i is the degeneracy of the i-th extended partition. Note that the sum in Eq. (74) is over the integer partitions, not the energy levels themselves. In lattice-based systems, the calculation of the energy of each state is often trivial and consequently the determination of the degeneracy is often the principal hurdle in the evaluation of Z [195, 207]. For $k > n$, there are no partitions of length greater than n available to contribute to the partition function because the length of such partitions would exceed the number of binding sites. Let $p(k,j)$ denote the number of integer partitions of k with exactly j parts. The sum of $p(k,j)$ over all $1 \leq j \leq k$ can then be denoted as $p(k)$, i.e.,

$$p(k) \equiv \sum_{j=1}^{k} p(k,j). \tag{75}$$

Let $\mathcal{K}$ denote the set of all integer partitions of k, and $\mathcal{K}_j$ denote the set of integer partitions with exactly j parts: $\mathcal{K}_j \subseteq \mathcal{K}$. By restricting the sum in Eq. (74) over partitions with less than or equal to n parts, we arrive at the canonical partition function for all ϕ_0 values, including cases with $k > n$,

$$Z(k,n,\delta) = \sum_{j=1}^{n} \left(\sum_{\substack{i=1 \\ \{\nu_k\}_i \in \mathcal{K}_j}}^{p(k,j)} g_i(\{\mu_k\}_i)\, \delta^{\mathcal{E}_i\left(\{\mu_k\}_i\right)} \right). \tag{76}$$

We have substituted the exponential Boltzmann factors in Eq. (76) with the parameter δ, given by Eq. (46).

As noted previously, the total number of microstates for k distinguishable macromolecules binding to n distinguishable sites is n^k. For each set of partitions of length

i, i.e., $\mathcal{K}_i$, we can thus sum over the size of each set through

$$n^k = \sum_{i=1}^{n} q^{\{\mathrm{p}\}}(n,i)\, S_2(k,i), \tag{77}$$

where

$$q^{\{\mathrm{p}\}}(n,i) = \frac{n!}{(n-i)!} \tag{78}$$

is a permutation operator and S_2 is a Stirling number of the second kind. In Eq. (77), each term in the sum is the number of microstates contributed to the total number of microstates by partitions of length i. We now need the number of permutations of each extended partition. Consider the number for ways of ordering k distinguishable macromolecules taken $\{\mu_k\}_i^1, \{\mu_k\}_i^2, \{\mu_k\}_i^3, \ldots, \{\mu_k\}_i^{\lambda(\{\nu_k\}_i)}$ at a time. The number of these permutations is given by

$$\begin{aligned} \mathcal{M}\left(\{\mu_k\}_i\right) &= \frac{k!}{\{\mu_k\}_i^1!\,\{\mu_k\}_i^2!\,\{\mu_k\}_i^3!\cdots\{\mu_k\}_i^k!} \\ &= k!\left(\prod_{j=1}^{\lambda(\{\nu_k\}_i)} \{\mu_k\}_i^j!\right)^{-1}. \end{aligned} \tag{79}$$

The product in the denominator can be truncated at the index value $j = \lambda\left(\{\nu_k\}_i\right)$ as the remaining terms in the product are equal to unity. Let $\{\Omega_k\}_i$ represent the occupancy vector of the extended partition $\{\mu_k\}_i$,

$$\{\Omega_k\}_i = \{o_0, o_1, o_2, o_3, \ldots, o_k\}, \tag{80}$$

where o_l is the number of sites with l bound macromolecules. Note that while the index of $\{\omega_k\}$ varies from 1 to k, the index of $\{\Omega_k\}$ varies from 0 to k. For $k = 3$ and $n = 5$, the occupancy vectors are $\{\Omega_3\}_1 = \{2,3,0,0\}$, $\{\Omega_3\}_2 = \{3,1,1,0\}$, and $\{\Omega_3\}_3 = \{4,0,0,1\}$. We define a permutation operator

$$Q^{\{\mathrm{p}\}}(\{\Omega_k\}_i) = \frac{n!}{o_0!o_1!o_3!\cdots o_k!}, \tag{81}$$

which counts the permutations with repeated elements of $\{\Omega_k\}_i$. The degeneracy of the i-th allowed partition belonging to $\mathcal{K}_j$ and its corresponding extended partition can therefore be expressed as

$$g_i(\{\mu_k\}_i) = \mathcal{M}\left(\{\mu_k\}_i\right) Q^{\{\mathrm{p}\}}(\{\Omega_k\}_i). \tag{82}$$

For consistency, it can be verified that

$$\sum_{\substack{i=1 \\ \{\nu_k\}_i \in \mathcal{K}_j}}^{p(k,j)} g_i(\{\mu_k\}_i) = q^{\{\mathrm{p}\}}(n,j)\, S_2(k,j), \tag{83}$$

and

$$\sum_{j=1}^{n} \left(\sum_{\substack{i=1 \\ \{\nu_k\}_i \in \mathcal{K}_j}}^{p(k,j)} g_i(\{\mu_k\}_i) \right) = n^k. \tag{84}$$

Combining Eqs. (76) and (82), the equilibrium occupied volume fraction ϕ_{E} can be expressed as

$$\phi_{\mathrm{E}}(k,n,\delta) = \sum_{j=1}^{j_{\max}} \left(\sum_{\substack{i=1 \\ \{\nu_k\}_i \in \mathcal{K}_j}}^{p(k,j)} \Phi(\{\nu_k\}_i)\, g_i(\{\mu_k\}_i)\, \delta^{\mathcal{E}_i(\{\mu_k\}_i)} \Big/ Z(k,n,\delta) \right), \tag{85}$$

where $j_{\max} = k$ if $k \leq n$ and $j_{\max} = n$ otherwise. At the limiting values of δ, the well-known values for ϕ are recovered:

$$\lim_{\delta \to 0} \phi_{\mathrm{E}}(k,n,\delta) = \begin{cases} \phi_0, & k \leq n \\ 1, & \text{otherwise} \end{cases} \qquad \text{and} \qquad \phi_{\mathrm{E}}(k,n,1) = 1 - \left(1 - \frac{\phi_0}{k}\right)^k. \tag{86}$$

To validate the analytical expression for ϕ_{E}, MC simulations were performed on systems with various values of δ, ϕ_0, and number of binding sites n. In these simulations, which were implemented using the Metropolis algorithm [129, 54], an initial random configuration was first relaxed to an equilibrium state by generating 10^6 configurations before a sampling phase was initiated. During the sampling phase, 10^6 configurations were generated. The ensemble average of these spatial states is the measured numerical result for ϕ_{E}. As shown in Fig. 22, the results of these simulations are in excellent agreement with the result given by Eq. (85). For systems with $n = 2$ binding sites, the partition function is trivially solved and we employ this case to illustrate the variation of ϕ_{E} with n.

A comparison between the equilibrium results for ϕ_{E}, given by Eq. (85), and the non-equilibrium results for ϕ generated by SSA procedure, and given by Eq. (66), are shown in Fig. 22 for various system parameter values. At low densities ($\phi_0 \leq 0.5$) the equilibrium and SSA results are in close agreement, but show increasing deviation as n is increased. In this density regime, a linear interpolation between ϕ values at the $\delta = 0$ and $\delta = 1$ limits

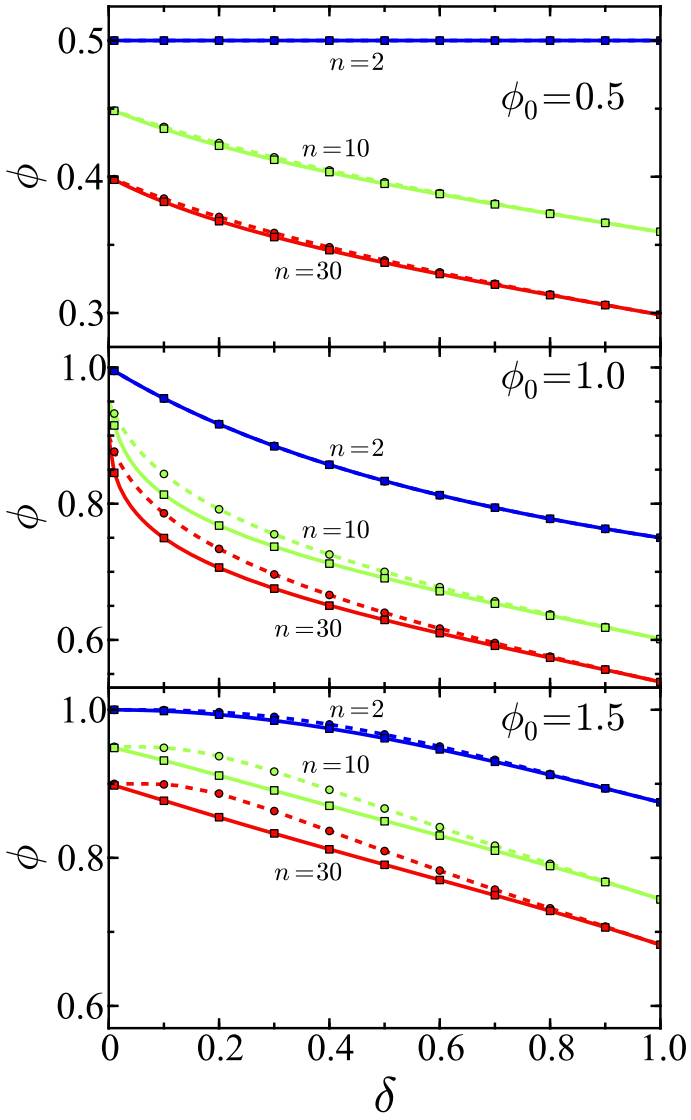

Figure 22: The fraction of occupied sites ϕ for $\phi_0 = 0.5$ (top), $\phi_0 = 1.0$ (middle), and $\phi_0 = 1.5$ (bottom) as a function of δ. For each value of ϕ_0, results are shown for $n = 2$ (blue), $n = 10$ (green), and $n = 30$ (red) binding sites. For $n \in \{10, 30\}$, all results are shift vertically by $\Delta\phi \in \{-0.05, -0.1\}$ for visual clarity. The dashed curves are the analytical results, given by Eq. (66), for a system undergoing SSA. Each circular marker is the result of 10^6 MC simulations for a system undergoing SSA. The analytical RSC distribution, given by Eq. (85), is shown as a solid curve. Each square marker is the result measured from 10^6 configurations generated using the Metropolis MC algorithm for the RSC distribution.

was seen earlier to yield satisfactory results for systems governed by stochastic bounded potentials [31], and this trend persists in the present lattice-based systems.

As the the density of the system is increased, large deviations between the equilibrium and non-equilibrium SSA results are observed. At $\phi_0 = 1.0$, ϕ shows a convex functional shape as for small values of δ, macromolecules are increasingly jammed into occupied sites. The result for the equilibrium RSC distribution is decreased with respect to the ϕ values generated by SSA. This decrease is caused by the propensity of macromolecules to move onto sites that are already occupied, increasing the number of multiple-occupation sites. In the SSA procedure this effect is absent as incident macromolecules bind irreversibly. For $\phi_0 = 1.5$, the system is over-packed as $k > n$. In this regime, macromolecules increasingly bind to already occupied sites, and ϕ shows a concave functional shape, differing sharply from cases with $\phi_0 \leq 1$. Interestingly, at large n, ϕ_{E} is an approximately linear function of δ while ϕ values generated by SSA continue to show strong non-linear behavior.

3.6 Off-Lattice Interactions

On continuum state spaces, systems whose dynamics are governed by deterministic bounded potentials form metastable crystalline phases at high densities (large ϕ_0) [113, 198, 175, 27]. Bounded potentials have also been realized stochastically [31], where the pairwise interaction between a set of particles i and j is described by the following equation:

$$V_{ij}^{\mathrm{S}}(r) = \begin{cases} 0, & r > \sigma \ , \\ 0, & r \leq \sigma \ \text{ and } \ a_{ij}\left(t_{\mathrm{col}}\right) < \delta \ , \\ \infty, & r \leq \sigma \ \text{ and } \ a_{ij}\left(t_{\mathrm{col}}\right) > \delta \ . \end{cases} \tag{87}$$

In dynamical simulations, Eq. (87) is implemented by generating a random number $a_{ij} \in [0, 1]$ at the time of collision t_{col} between particles i and j. If $a_{ij}\left(t_{\mathrm{col}}\right) > \delta$, the particles interact via a hard (HC) potential and collide elastically; otherwise the particles interpenetrate without interacting. As a_{ij} is generated each time the particles collide, the interaction (hard or ideal) between a set of particles can change many times throughout the simulation. In the potential given by Eq. (87), as in the SSA algorithm, δ is softness parameter, bridging completely hard ($\delta = 0$) and completely soft ($\delta = 1$) behavior. At intermediate values,

$(0 < \delta < 1)$, the mixing of hard collisions and soft ideal interactions generates complex spatial arrangements, including clustering regimes at large densities [30].

To study the applicability of Eq. (66) to systems that include off-lattice interactions, molecular dynamics (MD) simulations [70] were performed on a system of $k = 20$ particles (rods in one dimension and disks in two dimensions) constrained to move on a periodic surface $\mathcal{A}$, with each particle having a diameter σ and mass m. The potential between each pair of particles in these simulations is given by Eq. (87). To assign the initial position of each particle, a uniform lattice was constructed in $\mathcal{A}$ and the center of each particle was placed on a distinct lattice site. The initial velocities were sampled from a Boltzmann distribution and the system was then evolved through a time-driven hard-sphere algorithm [3] wherein the particles are treated as semi-hard rods and disks moving on $\mathcal{A}$. The underlying softness of the particle-particle interactions are adjusted through the parameter δ.

The MD simulations were performed in two phases. First, the system was spatially relaxed for 10^4 collisions. The relaxation phase was implemented to achieve an equilibrium structure. In the second phase, ϕ is measured using MC integration [102, 41, 31, 30]. The MC integration approach involves generating a large number of random coordinates in $\mathcal{A}$, and checking if those coordinates are overlapped by any particle from the system. The ratio of sampling points that are overlapped to the total number of points generated is ϕ. For each parameter set $\{\delta, \phi_0\}$, 10^4 frames were integrated by generating 10^6 sampling points per frame. To confirm that the system is in an equilibrium state during this sampling phase, simulations were also performed with the initial positions of the particles chosen randomly. The results measured using random initial positions were in agreement with those measured using a uniform lattice as the initial configuration. The volume fraction ϕ_0 is the occupied volume fraction of the system when no particles overlap. On a continuum state space this volume fraction is $\phi_0 = kv/\mathcal{A}$ where v is the volume of a single rod or disk. When the particles are allowed to overlap ($\delta > 0$) the observed volume fraction ϕ is less than ϕ_0.

The inclusion of off-lattice interactions generates a different distribution of states than those derived in Eqs. (66) and (72) due to the propensity for particles to be pushed into overlapping configurations by neighboring particles. To account for multi-body effects in the

distribution of spatial configurations, the pairwise softness parameter δ must be replaced with a multi-body induced softness parameter ζ, which can be derived from the effective pairwise potential between two particles. We have previously shown that in these systems the softness parameter δ has a significant influence on the form of the radial distribution function $g(r)$ [31, 30] and therefore this distribution is parameterized by δ: $g(r) = g(r;\delta)$. The potential of mean force (PMF), denoted as $w(r;\delta)$, between a pair of particles acts along the line connecting their centers and can expressed through $g(r;\delta)$ from the relationship

$$g(r;\delta) = e^{-\beta w(r;\delta)}, \tag{88}$$

where $\beta = 1/k_{\mathrm{B}}T$. An integral of $e^{-\beta w(r;\delta)}$ over the diameter of a single particle (the region where overlaps occur) is a sum of Boltzmann-weighted pairwise configurations, induced by interactions with all other particles in the system. The ratio of this multi-body induced distribution to the ideal ($\delta = 1$) distribution

$$\zeta(\delta) = \frac{\displaystyle\int_0^\sigma e^{-\beta w(r;\delta)}\, dr}{\displaystyle\int_0^\sigma e^{-\beta w(r;1)}\, dr}, \tag{89}$$

defines ζ. The mapping $\delta \mapsto \zeta$ must be used in Eqs (66) and (72) to account for off-lattice interactions.

As shown in Fig. 23, for a system of one-dimensional rods, the results for ϕ predicted by the lattice model and the MF model, both with ζ mapping, are in excellent agreement with the results measured from MD simulations over all ranges of δ and ϕ_0 studied. Figure 24 shows the results for ϕ given by the lattice model and the MF model, both with ζ mapping, and the results measured from MD simulations for a system of two-dimensional disks. The results are in excellent agreement apart from the small-$\delta(< 0.05)$, large-$\phi_0(= 0.769)$ regime. The compared theoretical expressions account only for acceptance and rejection outcomes, and in this regime the PMF has attractive sections and forms metastable wells in the overlapping region ($0 \leq r < \sigma$), causing deviation. The well depth of the PMF in the overlapping region, $\Delta V = w(\sigma^-;\delta) - w(0;\delta)$, increases at higher densities and lower δ values. For $\phi_0 = 0.25$ and $\delta = 0.75$, $\Delta V \approx 0.03\ k_{\mathrm{B}}T$, while for $\delta = 0.01$, $\Delta V \approx 0.9\ k_{\mathrm{B}}T$. At the highest density studied, $\phi_0 = 0.769$, for $\delta = 0.75$, $\Delta V \approx 0.1\ k_{\mathrm{B}}T$ and for $\delta = 0.01$,

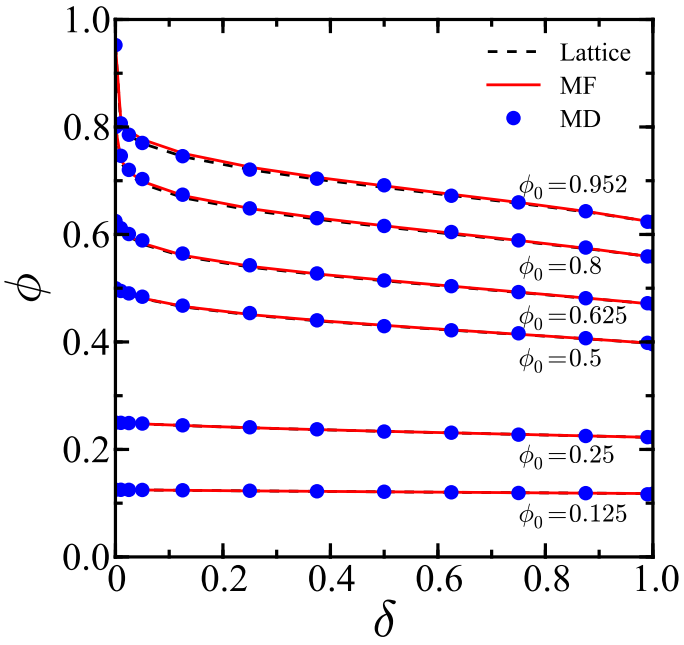

Figure 23: Occupied volume fraction ϕ one-dimensional rods as a function of the softness parameter δ for a system with included off-lattice interactions. The filled circles (blue) are the results measured from MD simulations. The dashed curves (black) are the results of the lattice model, obtained by combining Eqs. (66) and (89), The solid curves (red) are the results from the continuum MF method given by Eqs. (72) and (89).

$\Delta V \approx 5\, k_{\mathrm{B}}T$. Thus at large densities and small interparticle softness, a distinct transition to a cluster-forming regime is observed. The deviations between the MF results and the results measured from MD simulations, as shown in Fig. 24, are caused by this phase transition which is not included in the derivation of Eq. (72). This clustering phenomenon is in agreement with that previously observed in systems governed by deterministic [134] and stochastic [30] bounded potentials. As δ is moved slightly from the $\delta = 0$ limit, ϕ decreases drastically due to pressure pushing the particles into overlapped states. As higher densities are approached, the lattice model gives a slightly better prediction of ϕ with respect to the MF model. This is expected, as configurations on the continuum become more lattice-like when the available free volume for each particle decreases.

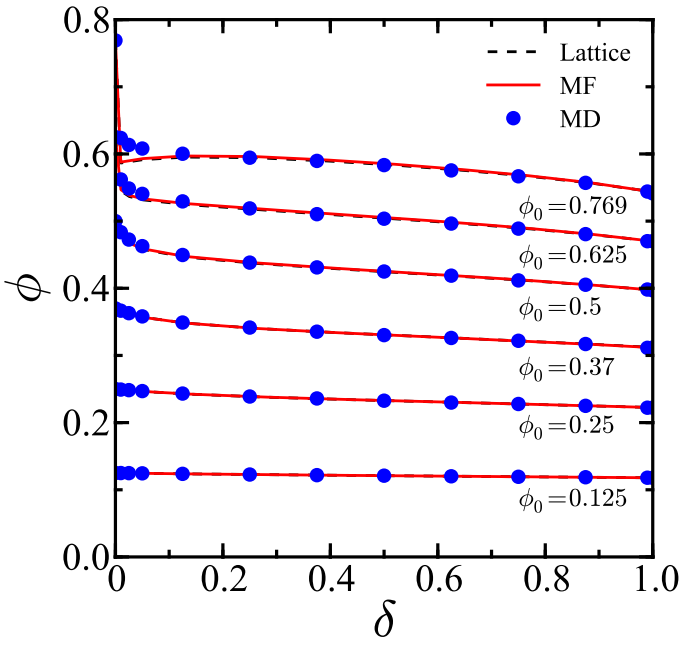

Figure 24: Occupied volume fraction ϕ of two-dimensional disks as a function of the softness parameter δ for a system with included off-lattice interactions. The filled circles (blue) are the results measured from MD simulations. The dashed curves (black) are the results of the lattice model, obtained by combining Eqs. (66) and (89), The solid curves (red) are the results from the continuum MF method given by Eqs. (72) and (89).

3.7 Conclusions

Motivated by the design of mesoscale devices with unique functionalities, we have obtained analytic and numerical relationships for the characteristic surface coverage in the sequential adsorption of soft macromolecules to a solid substrate with discrete binding sites. The exact fraction of occupied binding sites ϕ and the site occupancy distributions have been solved exactly for a developed avoidance-modified multiple occupancy model. The results of this derivation have been confirmed by comparison with Monte Carlo (MC) simulations. Due to the complexity of the exact expression at the thermodynamic limit, a mean field (MF) derivation for ϕ was presented and compared with the exact result and results measured from MC simulations. We have found that as the thermodynamic limit is approached, the MF expression converges to the exact result. Moreover, we conjecture that the MF expression is exact at the thermodynamic limit for a system consisting of discrete binding

sites.

The inclusion of off-lattice interactions was realized using a stochastic bounded potential which allows multiple macromolecules to occupy the same volume in a continuum configuration space. Molecular dynamics (MD) simulations were performed on system of macromolecules confined to move on a surface under the influence of a stochastic bounded potential. The fraction of configuration space occupied by the particle phase of the system was measured and compared with the results given the exact and MF expressions derived for the on-lattice sequential adsorption procedure. We find excellent agreement between these results, which provides evidence that, at the mesoscale, spatial configurations generated through avoidance-modified sequential addition processes can be smoothly mapped to the spatial configurations of a system in thermodynamic equilibrium. The relaxed surface coverage mechanism following the SSA has also been obtained directly from theory, confirmed by simulation, and seen to lead to reduced occupied volume fractions.

The results presented in this Chapter elucidate the range of clustering behavior and accessible structural configurations due to the soft and complex fluid interactions. Such interactions can arise at the mesoscopic length scales of computational models when the forces acting on atomistic degrees of freedom are coarse-grained. Fabrication processes involving the absorption of particles on a surface can generally be modeled through the stacking of non-overlapping building blocks. The present work includes the possibility that the inter-particle interactions are soft enough to allow overlaps. Fabrication utilizing such particles could thus lead to very different kinds of assemblies (with larger effective densities) and may be useful in creating new devices.

CHAPTER IV

TRANSPORT PROPERTIES OF PENETRABLE RODS

4.1 Introduction

In this Chapter we consider a system of of rods in one dimension, evolving through the stochastic penetration algorithm (SPA) presented in Chapter 2. Our aim is to derive dynamical properties across all ranges of softness δ, ranging from the $\delta = 0$ hard rod (HR) limit to the $\delta = 1$ ideal limit. One-dimensional systems are studied mainly because they are often analytically tractable. These analytic results give insight into more realistic systems in higher dimensions. The equation of state for the a HR ($\delta = 0$) system was solved exactly by Tonks [181] and thus this system is colloquially known as a Tonks gas. Further theoretical studies of the nonequilibrium properties of the HR system have also been performed, notably by Jepsen [82], Lebowitz *et al.* [99, 100, 101], and also Kasperkovitz and Reisenberger [85]. Bishop and Berne [14] as well as Haus and Raveché [69] have confirmed the predictions of previous theoretical work using molecular dynamics simulations.

Here, we develop theory to predict the dynamical properties of a one-dimensional SPA system. We find that while the spatial properties derived in Chapter 2 are complex, the dynamical properties can predicted adequately using simple Enskog corrections to Boltzmann kinetic theory. As shown in Fig 25, the value of the softness parameter δ has a significant influence on the dynamical behavior. Shown in Fig 25(a) are trajectories for a system of HRs. At the HR limit ($\delta = 0$) the system is well-ordered having only nearest-neighbor interactions. As shown in Fig 25(d), at the ideal limit ($\delta = 1$) the particles never interact and each particle moves ballistically. For intermediate values of δ, as shown Fig 25(b) and (c), complex interaction networks are generated. The aim of this Chapter is to understand the effect that these interaction networks have on the system's dynamical observables.

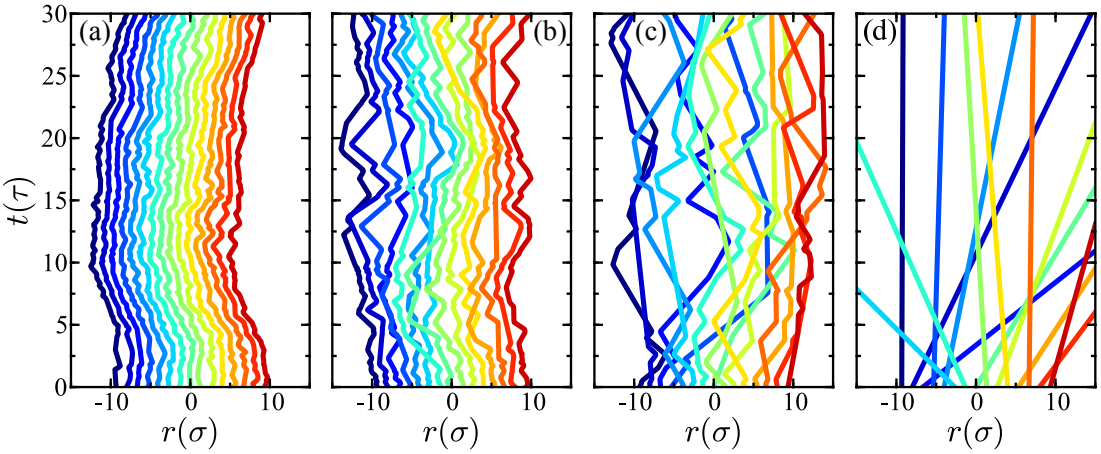

Figure 25: Representative SPA trajectories of 15 initially neighboring particles evolving through Eq. (93) for (a) $\delta = 0.0$, (b) $\delta = 0.05$, (c) $\delta = 0.5$, and (d) $\delta = 1.0$ at $\phi_0 = 0.75$. The trajectory of each particle is shown in a different color. The x-axis shows the particles position in reduced units r/σ and the y-axis shows time in reduced units t/τ.

4.2 Simulation Details

Molecular dynamics (MD) simulations have been performed on a system of $N = 200$ rods with each rod having a length σ and mass m. These particles are constrained to move under periodic boundary conditions on a line of length L_x. The initial positions of each particle are chosen by placing each particles center of mass on a uniform lattice. The initial velocities are sampled from a Boltzmann distribution,

$$f_{\mathrm{M}}(v_x) = \sqrt{\frac{m}{2\pi k_{\mathrm{B}} T}} \exp\left(-\frac{m v_x^2}{2 k_{\mathrm{B}} T}\right). \tag{90}$$

The average speed for a one-dimensional Maxwellian system is $\langle v \rangle = \sqrt{2 k_{\mathrm{B}} T / \pi m}$. Throughout this Chapter, values of the reported observables are reduced using σ and $\tau = \sigma / \sqrt{k_{\mathrm{B}} T / m}$. The dynamics of the system of rods are evolved through the SPA introduced in Chapter 2. The time-dependence of SPA connection network can be expressed as a symmetric adjacency matrix

$$\mathbf{S}(t) = \begin{pmatrix} s_{11} & s_{12} & \cdots & s_{1N} \\ s_{21} & s_{22} & \cdots & s_{2N} \\ \vdots & \vdots & \ddots & \vdots \\ s_{N1} & s_{N2} & \cdots & s_{NN} \end{pmatrix} \tag{91}$$

where each s_{ij} takes values 0 or 1, depending on if the pairwise connection is HC or ideal. Through Eq. (91) and the hard sphere potential

$$V^{\mathrm{HS}}(r) = \begin{cases} 0, & r > \sigma \ , \\ \infty, & r \leq \sigma \ . \end{cases} \tag{92}$$

the single particle equation of motion can be expressed as,

$$m\ddot{r}_i = -\sum_{j \neq i}^{N} s_{ij}(\delta, t) \nabla V^{\mathrm{HS}}(r_{ij}). \tag{93}$$

The *effective* potential can be expressed as

$$V(t;\delta)_{\mathrm{eff}} = -k_{\mathrm{B}}T \left(\sum_{i<j}^{N} s_{ij}(t) \right) \ln \delta, \tag{94}$$

which is identical to the potential energy of the penetrable sphere (PS) model, given by Eq. 2.

In simulation, before a sampling phase was initiated, the system was aged for $\mathcal{N} > 10^5$ total (hard and soft) collisions. Formally, the potential energy of the system is always zero and a system of particle evolving through Eq. (93) samples the NVE ensemble with the temperature T being a conserved quantity. The HC volume fraction $\phi_0 = N\sigma/L_x$ is the occupied volume fraction of the system when no spheres overlap ($\delta = 0$). Throughout this Chapter we will express the dynamical properties as function of effective density ϕ_0 and interparticle softness δ.

4.3 Structural Properties

The dynamical properties presented in this Chapter can be derived from knowledge of the radial distribution function (RDF) $g_2(r)$. Specifically, the value of the RDF at positive contact $g_2(\sigma^+)$ and the ζ parameter, presented in Chapter 2, play a key role in the investigated dynamical processes. Salsburg, Zwanzig, and Kirkwood [164] have derived an exact analytic expression for the RDF of the HR model. This structural prediction has been shown to agree with results obtained through MD simulations [14, 69]. In this Section, we will extend a derivation by Malijevský and Santos [123] for the RDF of a system of deterministic penetrable rods to obtain theoretical expressions for ζ and other pair-wise structural parameters of the SPA model.

As presented in Chapter 2, the softness parameter δ has a large influence on the functional form of the RDF, and therefore we must include it as a parameter $g_2(r;\delta)$. The known positive contact values of the RDF at the limiting values of δ are

$$g_2(\sigma^+;0) = \frac{1}{1-\phi_0}, \qquad g_2(\sigma^+;1) = 1, \tag{95}$$

for a Tonks gas and an ideal gas, respectively. These expressions are valid at the thermodynamic limit. In SPA systems the ratio of negative flow to positive flow is equal to δ, i.e.,

$$\delta = \frac{g_2(\sigma^-;\delta)}{g_2(\sigma^+;\delta)}\,, \tag{96}$$

where $g_2(\sigma^-;\delta)$ as the RDF value at negative contact.

Malijevský and Santos [123] have derived an expression for the penetrable sphere (PS) model in one dimension. Adapting this derivation for the SPA model gives

$$g_2(r;\delta) = (r-1)C_0(\delta)\Theta(1-r) + \sum_{n=0}^{\infty}\psi(r-n)\Theta(r-n), \tag{97}$$

where

$$C_0(\delta) = \delta\frac{\sigma}{\phi_0}\epsilon_1(\epsilon_0-\epsilon_1), \tag{98}$$

and

$$\psi_n(r) = \exp\left[-\epsilon_1 r\right]\frac{\sigma}{\phi_0}\frac{r^{n-1}}{n!}(n+(\epsilon_0-\epsilon_1)r)\epsilon_1^n. \tag{99}$$

The parameter ϵ_1 is a solution to the transcendental equation

$$\epsilon_1 = \frac{1-\delta}{\delta}(\epsilon_0-\epsilon_1)\exp\left[-\epsilon_1\right], \tag{100}$$

and can be expressed in terms of ϵ_0 as

$$\epsilon_1 = \frac{\sigma\epsilon_0-\phi_0}{\phi_0}. \tag{101}$$

Equation (97) gives an excellent approximation to the RDF across all values of δ, as shown in Fig. 26. Although not shown, the agreement between Eq. (97) and the results measured from simulation begins to diverge at densities above HR close-packing ($\phi_0 > 1$) and small-δ values.

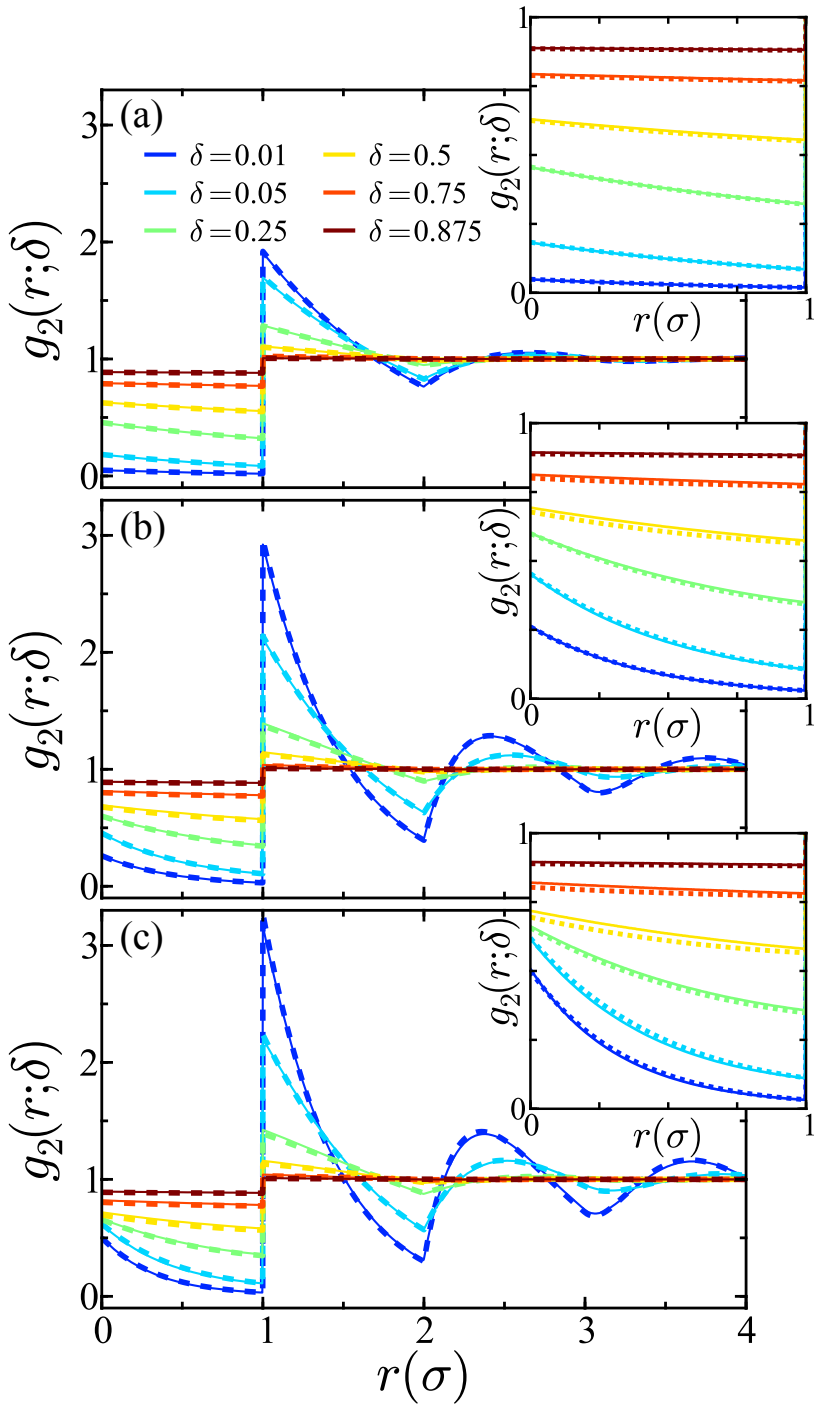

Figure 26: The radial distribution function for (a) $\phi_0 = 0.5$, (b) $\phi_0 = 0.75$, and (c) $\phi_0 = 0.85$ and various values of δ. The solid line is the result of MD simulations. The dashed line is the result given by Eq. (97). Above each each panel is an inset of the penetrative region.

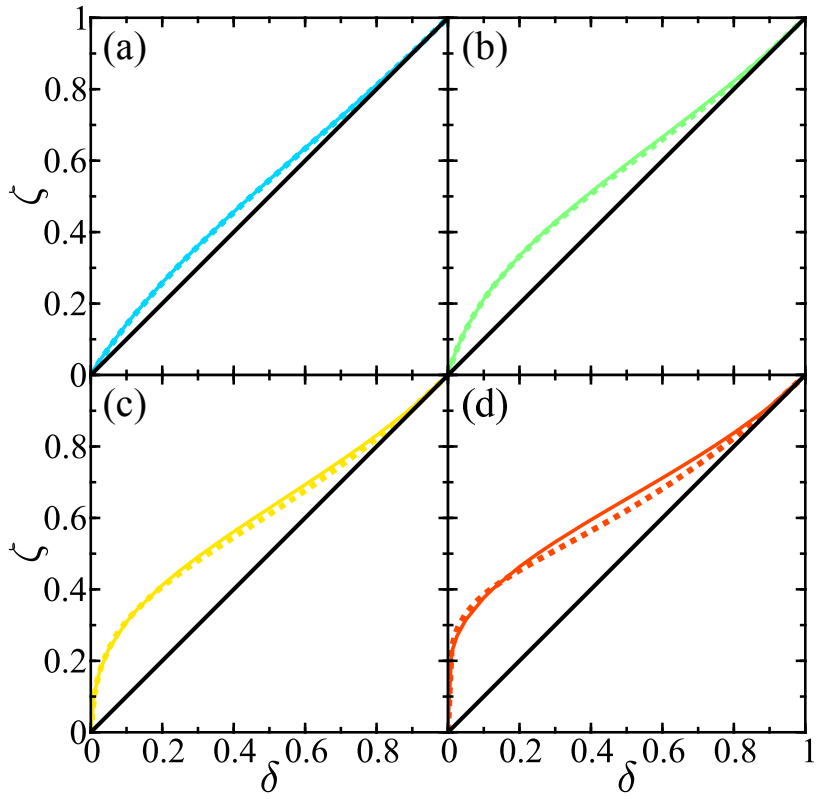

Figure 27: ζ as a function of δ for (a) $\phi_0 = 0.25$, (b) $\phi_0 = 0.5$, (c) $\phi_0 = 0.75$, and (d) $\phi_0 = 0.95$. In each panel, the solid curve is the result measured from MD simulations and the dotted curve is the result obtained from a quadrature of Eq. (97) over the penetrative region. The thick solid line is the infinite dilution limit where $\zeta = \delta$.

Combining Eqs. (10), (12), and (97), the multi-body softness paramter ζ can be obtained non-empirically. Shown in Fig. 27 are the results of the theoretical prediction for ζ, and the empirical results. These results are in excellent agreement.

To quantify the degree of pair-wise translation order in the SPA system, the structural order parameter

$$-s_2(\delta) = \frac{\phi_0}{\sigma} \int_0^\infty g_2(r;\delta) \ln g_2(r;\delta) - [g_2(r;\delta) - 1]\, dr \ , \tag{102}$$

was computed from simulation results. For a perfectly crystalline system, $-s_2(0) = \infty$, and for an ideal gas at any density, $-s_2(1) = 0$. As illustrated in Fig. 28(a), $-s_2$ is a monotonically increasing function of ϕ_0, which is the same trend expected for simple fluids. Moreover, we observe no anomalous clustering behavior, characterized by a turnover in $-s_2$, in a one-dimensional SPA system. Anomalous clustering has been previously observed in a Gaussian-core fluid in three dimensions [95], and also for the SPA model in three dimensions [30].

Truskett and co-workers [96] have put forth the cumulative structural order integral

$$I_{s_2}(r;\delta) = \frac{\phi_0}{\sigma} \int_0^r g_2(r';\delta) \ln g_2(r';\delta) - \big[g_2(r';\delta) - 1\big]\, dr' \ . \tag{103}$$

to measure the contribution that each coordination shell has on the total pair-wise order. Note that in the limit $r \to \infty$, $I_{s_2} \to -s_2$. For densities close to and greater than close-packing ($\phi_0 > 0.95$), there is less correlation inside the core region than that observed at lower densities. Thus, overlapping rods become decorrelated with increasing density at small values of δ. This trend can be observed in Fig. 28(b).

4.4 Mean Free Path and Collision Frequency

The mean free path λ, defined as the average distance a single particle travels between collisions, is the characteristic length scale of ballistic motion. In systems evolving through continuous potentials, particles constantly interact and the notion of discrete and impulsive events, i.e, collisions, is ill-defined. In one dimension, Boltzmann kinetic theory predicts that for a system of rarefied HRs ($\delta = 0$),

$$\lambda_{\mathrm{B}} = \frac{\sigma}{\sqrt{2}\phi_0} \ , \tag{104}$$

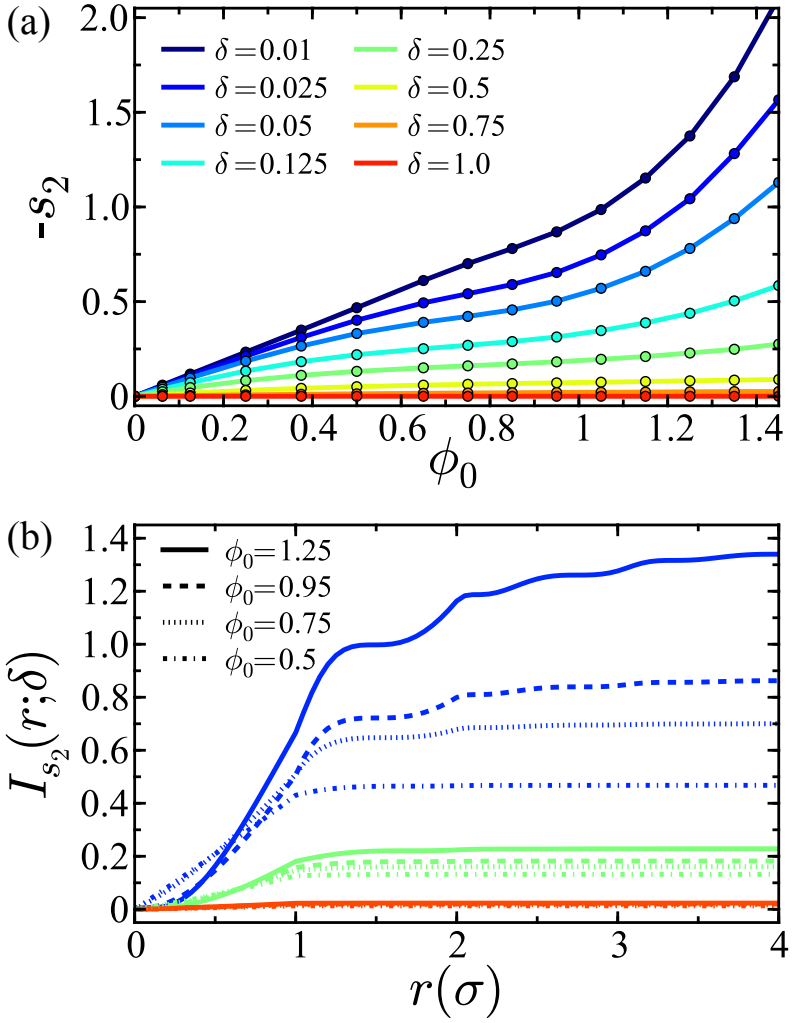

Figure 28: (a) The pairwise structural order parameter $-s_2$ as a function of ϕ_0 for various values of δ. The results have been extrapolated to the $\phi_0 = 0$ limit. (b) The cumulative order integral $I_{s_2}(r;\delta)$ at $\delta = 0.01$ (blue), $\delta = 0.25$ (green), and $\delta = 0.75$ (red) for $\phi_0 \in \{0.5, 0.75, 0.95\}$.

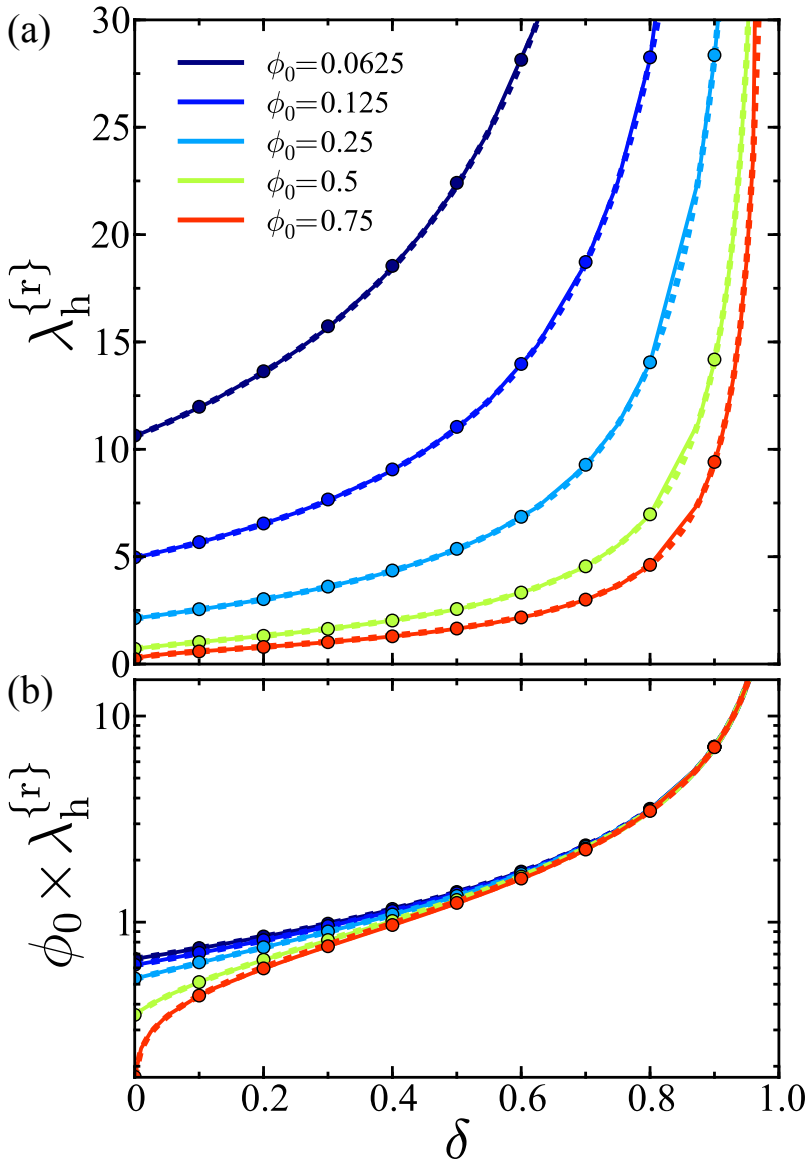

Figure 29: (a) The reduced mean free path $\lambda_h^{\{r\}} = \lambda_h/\sigma$ as a function of δ, for various values of ϕ_0. (b) The reduced mean free path scaled by the HC volume fraction $\phi_0 \times \lambda_h^{\{r\}}$ as a function of δ. In both panels the circles are the results measured from MD simulations. The curves given by Eq. (106) are shown using empirical values for $g_2(\sigma^+;\delta)$ (dashed) and parametrized values (solid).

which is valid at infinite dilution where $g_2(\sigma^+) = 1$. As the density of the system is moved away from infinite dilution limit toward a structured state, Eq. (104) must be modified by the Enskog factor χ

$$\lambda_{\rm h} = \frac{\lambda_{\rm B}}{\chi} \, , \tag{105}$$

where $\chi = g_2(\sigma^+)$ is the radial distribution function at positive contact. For finite densities ($\phi_0 > 0$), $g_2(\sigma^+) \neq 1$, and $\lambda_{\rm h} < \lambda_{\rm B}$, as the system has intrinsic structure.

In systems evolving through stochastic rules the effect of δ has a large significance on the static structure and also on $g_2(\sigma^+; \delta)$. Due to the the local density of surrounding particles, Eq. (105) must be modified by a factor $(1 - \delta)$ giving

$$\lambda_{\rm h}(\delta) = \frac{\sigma}{\sqrt{2}\phi_0} \left(\frac{1}{(1-\delta) g_2(\sigma^+; \delta)} \right) \, , \tag{106}$$

which is the Enskog-modified mean free path for a system evolving under the SPA model.

A comparison between the results given by Eq. (106) and results measured from simulation is shown in Fig. 29(a). The results measured from simulation are in excellent agreement with those predicted by Eq. (106) over all values of δ and ϕ_0 studied. For small δ, $\lambda_{\rm h}$ is non-linear in ϕ_0. For larger values of δ, the free path scales linearly in density, which can be observed in Fig. 29(b).

From Eq. (106) and the average speed $\langle v \rangle$, the hard collision frequency can be expressed as

$$\omega_{\rm h} = \frac{\langle v \rangle}{\lambda_{\rm h}} \, , \tag{107}$$

and the soft collision frequency as

$$\omega_{\rm s} = \frac{\langle v \rangle}{\lambda_{\rm B}} g_2(\sigma^-; \delta) \, . \tag{108}$$

Note that a soft mean free path is ill-defined as a particle can exchange velocities many times between soft collision events. The total collision frequency

$$\omega_{\rm tot} = \omega_{\rm h} + \omega_{\rm s} \, . \tag{109}$$

can therefore be expressed in term of the positive and negative contact values,

$$\omega_{\rm tot}(\delta) = \frac{\langle v \rangle}{\lambda_{\rm B}} \left(\frac{g_2(\sigma^+; \delta)}{g_2(\sigma^-; \delta) \left(g_2(\sigma^+; \delta) - g_2(\sigma^-; \delta) \right)} \right) \, . \tag{110}$$

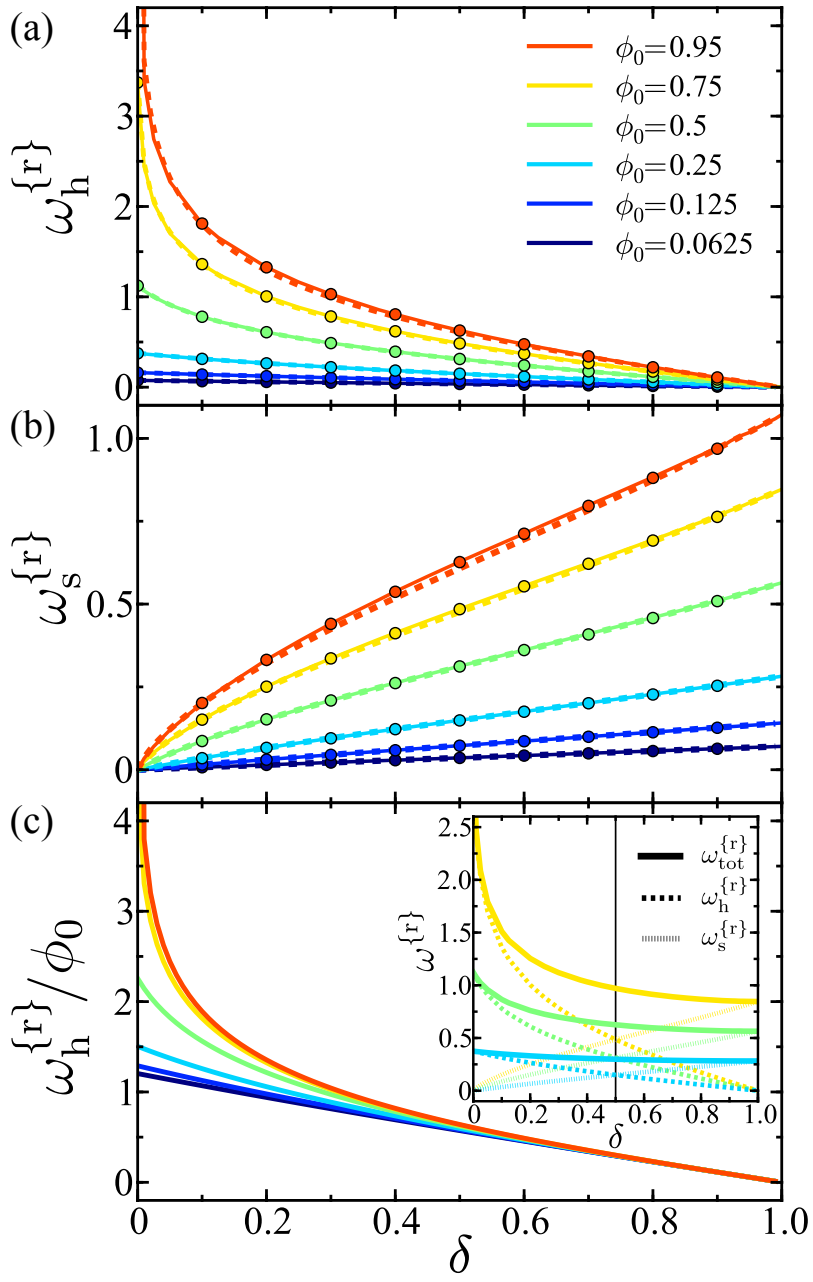

Figure 30: (a) The reduced hard collision frequency $\omega_{\rm h}^{\{\rm r\}} = \omega_{\rm h}\tau$ as a function of δ. (b) The reduced soft collision frequency $\omega_{\rm s}^{\{\rm r\}} = \omega_{\rm s}\tau$ as a function of δ. For both (a) and (b), the curves given by Eq. (107), are shown using empirical values (solid) and theoretical values (dashed) for $g_2(\sigma^+;\delta)$. The circles are the results measured from MD simulations. (c) The the reduced hard collision frequency scaled by ϕ_0 as a fucntion of δ with $g_2(\sigma^+;\delta)$ values given by Eq. (theoretical). Inset is the reduced total collision frequency $\omega_{\rm tot}^{\{\rm r\}}$ given by Eq. (107) with $g_2(\sigma^+;\delta)$ taken from empirical values. The solid horizontal line ($\delta = 0.5$) is the point where $\omega_{\rm h}^{\{\rm r\}} = \omega_{\rm s}^{\{\rm r\}}$. In all panels, the colors correspond to respective ϕ_0 values shown in the legend of (a).

Shown in Fig. 30 is a comparison between the theoretical collision frequencies and the results measured from simulation. While $\omega_{\rm s}$ is an approximately linear function of δ, $\omega_{\rm h}$ is highly non-linear in the small-δ regime at large densities. The results for the scaled hard collision frequency $\omega_{\rm h}/\phi_0$, shown in Fig 30(c), illustrate the hard collision frequency that does not scales linearly in density. Inset in Fig 30(c) are the measured results for total collision frequency $\omega_{\rm tot}$ and as expected, for $\delta = 0.5$, $\omega_{\rm h} = \omega_{\rm s}$.

4.5 Velocity Autocorrelation Function

The velocity autocorrelation function (VACF) $\langle v_x(0)v_x(t)\rangle$ defines the relaxation rate of a single particle's velocity to the average value, i.e., it defines the time-scale over which a particle's velocity decorrelates with its intial value. In one dimension, the normalized VACF can be expressed as

$$\psi(t) = \frac{\langle v_x(0)v_x(t)\rangle}{\langle v_x(0)v_x(0)\rangle} \tag{111}$$

Enskog theory predicts that for uncorrelated (binary) collision processes the VACF is

$$\psi_{\rm E}(\delta; t) = e^{-2\omega_{\rm h}(\delta)t} \tag{112}$$

where $\omega_{\rm h}(\delta)$ is the hard collision frequency, given by Eq. (107). This exponential decay is observed in other systems such as a Markovian Langevin system with an uncorrelated noise term. For an infinite system of HRs, Jepsen [82] presented an exact solution for the VACF. Interestingly, he predicted an asymptotic decay with a negative tail scaling as t^{-3}, which was later confirmed in simulation [14, 69].

Figure 31 shows the short-time results for the VACF, given by Eq. (112) and the results measured from MD simulations. In the liquid-like density regimes, these results are in agreement. Moreover, the short-time decay of the VACF is approximately exponential for all values of δ, while the long-time decay shows exponential behavior only in the large-δ regime, as illustrated in Figure 32.

From the Green-Kubo relation, the diffusion coefficient can be expressed in terms of the VACF as

$$D = \int_0^\infty \langle v_x(0)v_x(t)\rangle \, dt. \tag{113}$$

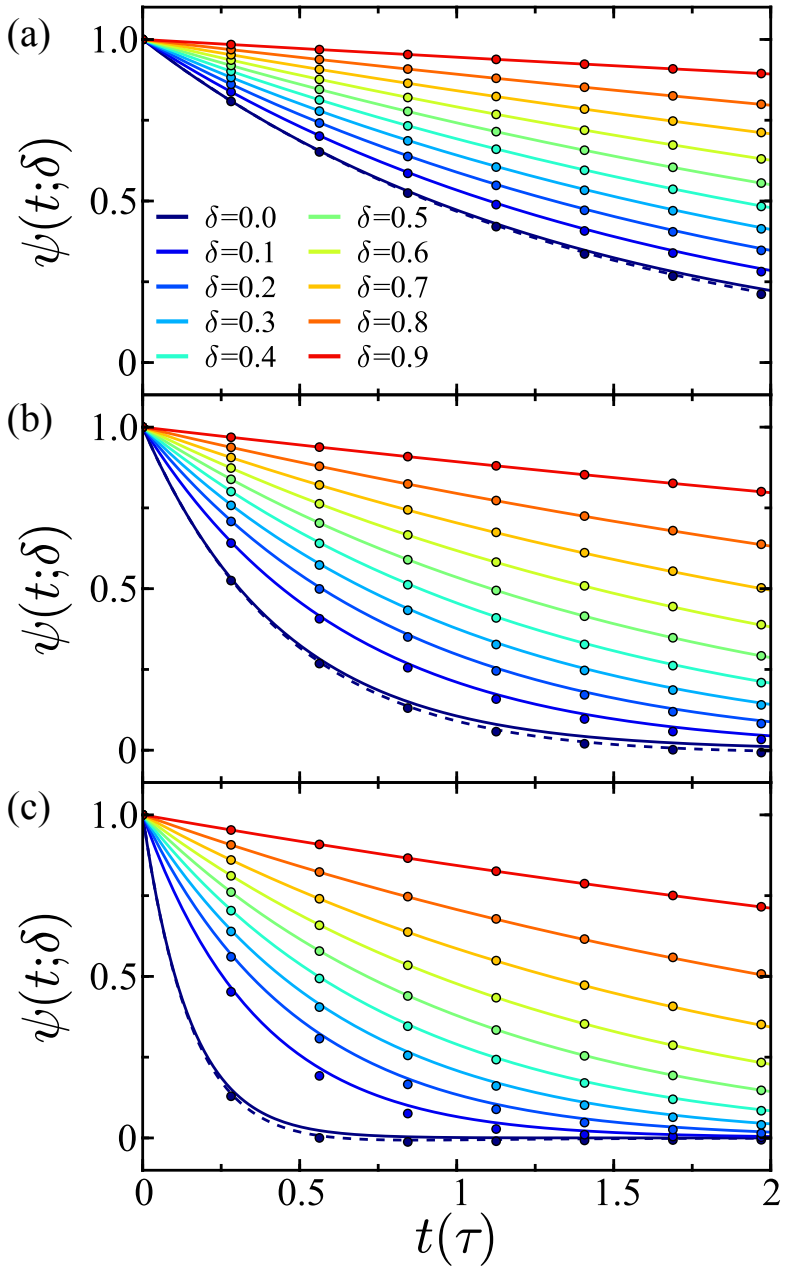

Figure 31: The short-time decay of the velocity autocorrelation $\psi(t;\delta)$ for various values of δ at (a) $\phi_0 = 0.25$, (b) $\phi_0 = 0.5$, and (c) $\phi_0 = 0.75$. The circular markers are the results measured from MD simulations. The solid curves are the Enskog result given by Eq. 112. The dashed curves are exact result [82] for an infinite system of HRs.

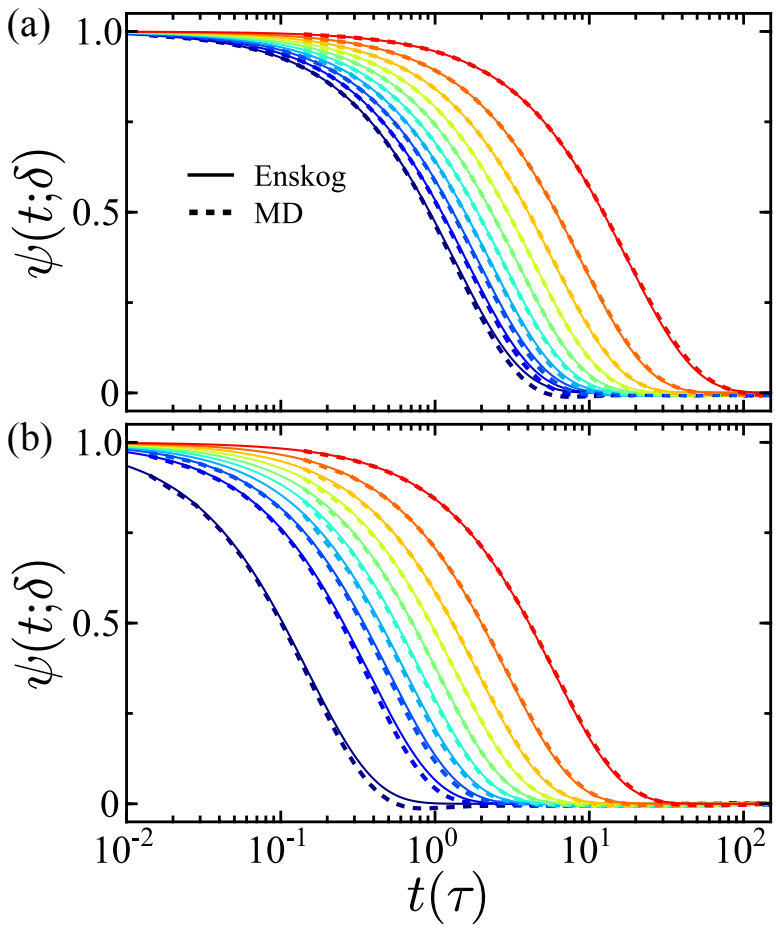

Figure 32: Semi-log plot showing the long-time decay of the velocity autocorrelation $\psi(t;\delta)$ for various values of δ at (a) $\phi_0 = 0.25$ and (b) $\phi_0 = 0.75$. The dashed lines are the results measured from MD simulations. The solid curves are the Enskog result. Each curve is colored as in Fig. 31.

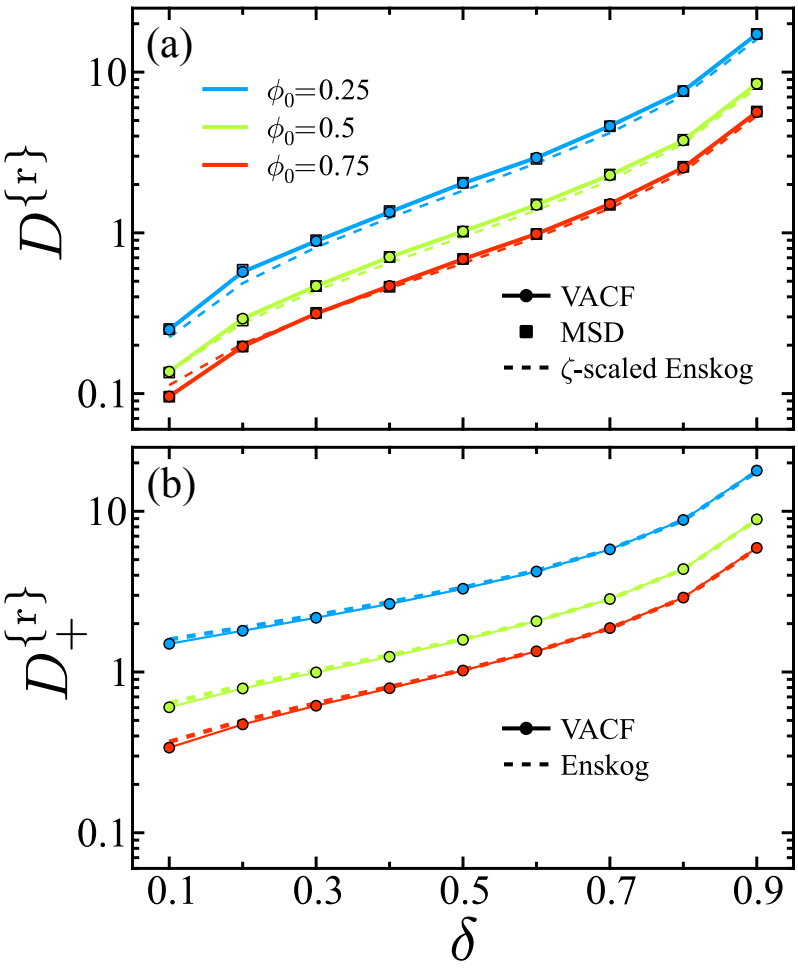

Figure 33: (a) The reduced diffusion constant $D^{\{r\}} = D/\sigma\sqrt{k_B T/m}$ as a function of δ for $\phi_0 = 0.25$ (blue), $\phi_0 = 0.5$ (green), and $\phi_0 = 0.75$ (red). (b) The reduced diffusion constant $D_+^{\{r\}} = D_+/\sigma\sqrt{k_B T/m}$ as a function of δ. The solid curves with circular markers are the results measured from the velocity autocorrelation function (VACF), calculated from MD simulations. The square markers are the results given by the mean square displacement (MSD), calculated from MD simulations. The dashed curves are the results given by Eq. (114) in (a) and Eq. (116) in (b).

Combining Eqs. (12), (112), and (113), we arrive at a theoretical expression for the diffusion coefficient,

$$D_\zeta(\delta) = \frac{k_\mathrm{B}T}{m\sigma}\int_0^\infty\int_0^\sigma e^{-(\beta w_2(r;\delta)+2\omega_\mathrm{h}(\delta)t)}\,dr\,dt, \tag{114}$$

which we will refer to as the ζ-scaled VACF. Figure 33(a) illustrates the agreement observed between the theoretical ζ-scaled diffusion coefficient and diffusion coefficient measured from simulation using Eq. (113), and also with the result obtained from the mean-square displacement (MSD). To quantify the effect the negative tail has on the measured diffusion coefficient, the measured VACF was integrated up to the first time that the sign of the VACF changes from positive to negative t_c. The positive contribution to the total integral for D is thus

$$D_+(\delta) = \int_0^{t_\mathrm{c}} \langle v_x(0)v_x(t)\rangle\,dt. \tag{115}$$

Based on the results presented in Fig. 31 for the short-time decay of the VACF, it is expected that the positive contribution can be well-approximated by the exponential Enskog VACF,

$$D_+(\delta) = \frac{k_\mathrm{B}T}{m}\int_0^{t_\mathrm{c}} e^{-2\omega_\mathrm{h}(\delta)t}dt. \tag{116}$$

As can be observed Fig. 33(b), Eq. (116) is in agreement with values obtained by integrating Eq. (115), over all parameter values studied. Comparing the true values for D with those for D_+, it can be seen that the negative tail has a significant effect on these values. This effect persists for small-δ regimes but is less severe for large values of δ as the collisions become less correlated.

4.6 Conclusions

The dynamical properties of a system of penetrable rods constrained to move on a line in one dimension have been probed through theory and simulation. We have shown that through a single softness parameter, the limiting dynamical regimes can be bridged. In contradiction to unbounded deterministic models in which information flow between neighboring particles is continuous, stochastic interactions allow particles to overlap and resulting connection networks allow the derivation equations of motion representative of mesoscale dynamics.

Extending the current single-length-scale system to a system with multiple length scales [64, 205, 141, 97, 37] provides for possible future directions of the present work. Barkan *et. al* have shown that the controlled assembly of particles interacting through bounded potentials with multiple length scales allows the generation of structures with periodic and aperiodic lattice geometries, including quasi-crystalline phases [9] and Archer *et. al* have shown that in a system of two-length-scale, soft-core (bounded) particles, there exists a crystal-liquid state as characterized by a set of mobile particles inside a lattice structure [4]. Extending the SPA to have multiple regions of stochastic penetration, could give rise to similar structural behavior and allow for probing such systems at finite temperatures.

CHAPTER V

CHEMICAL REACTIONS INDUCED BY OSCILLATING EXTERNAL FIELDS

5.1 Introduction

Optimal control of reaction pathways in systems undergoing configurational changes can be achieved through forcing from tailored external fields. These fields can be tuned to induce specific deformations on a potential energy surface, providing control of state-to-state transitions [206, 177, 87]. In these processes, a formally exact rate calculation can be obtained through transition state theory (TST) and it is thus is a pillar of classical reaction dynamics and kinetics [189, 188, 133, 191, 200, 72]. The principle assumption of TST is that there exists a hypersurface between reactant and product confirmations that is crossed only once by reactive trajectories during the ascent of an energy barrier separating these basins. The TST reaction rate is calculated from the flux through this dividing surface (DS). If the DS is recrossed by reactive trajectories, TST will give an overestimate to the rate. If a recrossing-free surface can be constructed, the TST rate is classically exact. With this criterion defined, a fundamental focus of reaction dynamics is the construction of a recrossing-free DS.

A phase space DS that is free of recrossings can be constructed in conservative systems at energies close to the reaction threshold. In systems with two degrees of freedom, the optimal DS is the configuration space projection of an unstable periodic orbit (PO) [150, 151, 146, 149]. In systems with higher dimensionality, the generalization of this PO is a normally hyperbolic invariant manifold (NHIM) [73, 71, 193, 35, 107, 199, 44, 45, 180]. The NHIM bounds the TS, being one less in dimension [193]. It defines a recrossing-free surface at energies below bifurcation thresholds [77, 2, 118]. Reactive trajectories are mediated by stable and unstable manifolds (reaction pathways) attached to the NHIM. These pathways persist even in reactions where state transitions are not dictated by purely configurational

changes [78].

In systems subjected to time-varying external forcing, the formulation of the NHIM as a hypersphere of constant energy breaks down. For example, field-matter interactions constitute processes where energy is exchanged with a reacting system. These interactions lead to emergent and controllable behavior in assembly phenomena [42, 80, 156, 117], organic synthesis [109], protein folding [147], the detection of DNA [115], and photodissociation [25]. Knowledge of the mechanism by which these interactions mediate reactive flow provides a methodological tool in the design of molecular devices with unique functionality [163, 130, 209].

The development of materials that undergo conformational changes in response to an external trigger offer examples of such emergent technology [18, 88, 6, 130, 128]. Stimuli such as thermal variations, electric fields, and photoinduction have been used as triggers for the conversion of chemical energy into mechanical work [49, 106, 52, 209]. Assemblies that convert chemical energy into directional motion can achieved through isomerization reactions which are induced either from light or applied electric fields [75, 93, 163]. In these responsive materials, controlling the rate and pathway at which reactants transform to products is fundamental to harness mechanical actions for applicative purposes.

The goal of this Chapter is to develop a rate theory for reactions that are driven by periodic external fields in weak thermal environments. We have shown in Ref. [29] that in systems driven periodically, there persists an optimal DS that is time-dependent. This structure differs from the canonical view of the TS as a structure that is fixed in time at a saddle point on the potential energy surface. Here, we develop a rate theory based on reactive flux through this recrossing-free DS and the stability of the corresponding TS. In Ref. [28] we have shown that for single-mode sinusoidal driving, the stability of the moving TS directly determines the reaction rate. In conservative systems, stability analysis is known to characterize molecular motions as well as determine the rate of configurational transitions [84, 171, 56, 63, 2]. Building on our previous work, we test the viability of stability analysis to determine reaction rates in systems driven by multi-mode waveforms with no thermal driving. To what extent the developed theory persists in systems that are coupled to a

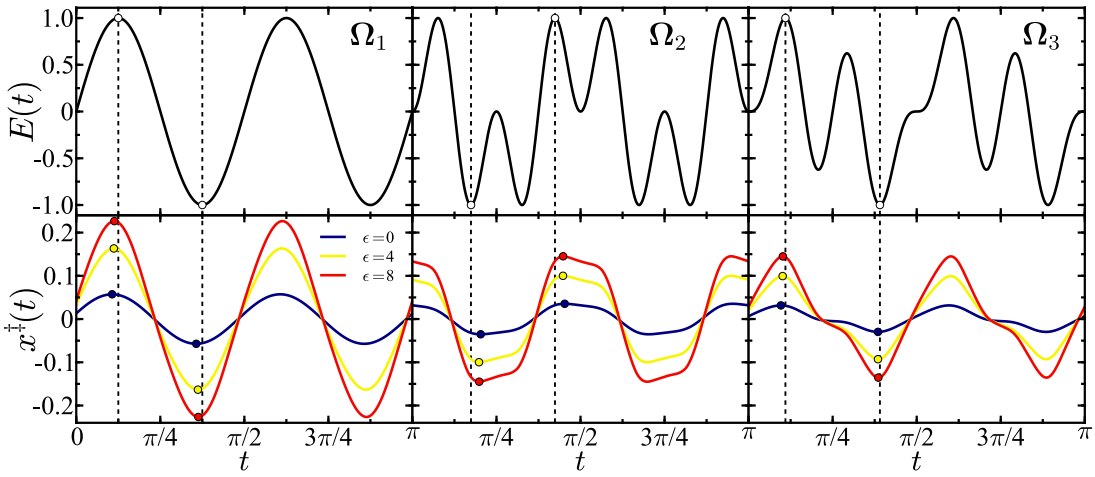

Figure 34: Functional forms of the periodic driving $E(t)$ for the frequency sets $\mathbf{\Omega}_1$ (left), $\mathbf{\Omega}_2$ (middle), and $\mathbf{\Omega}_3$ (right) with fundamental driving frequency $\Omega_f = 4$ are shown in the top row. The corresponding TS trajectory for each frequency set and anharmonic parameter values $\epsilon \in \{0, 4, 8\}$ are shown in the bottom row. Various extrema of $E(t)$ are denoted by circles with arguments shown as dashed vertical lines. The corresponding extrema of $x^\ddagger(t)$ are denoted by circles and colored according to the respective ϵ value. Parameters for all panels are $\sigma = 0$, $\gamma = 1$, and $\varphi = 0$ in dimensionless units.

thermal bath is also tested through inclusion and variation of the thermal driving strength.

This outline of this Chapter is as follows: In Sec. 5.2 a dynamical system is introduced to model barrier crossings in chemical reactions forced by periodic external fields. In Sec. 5.3 a dividing surface that is recrossing-free is constructed for this model in the absence of thermal driving. Section 5.4 contains analytical theories to predict the reaction rates of driven reactions by calculation of the reactive flux through this dividing surface for both globally non-linear and locally linear dynamics. A comparison between the the developed theories and the rates calculated from numerical integration of large ensembles of trajectories is presented in Sec. 5.5. Section 5.6 contains a comparison of reaction rates with included thermal driving to the rates of corresponding systems that are purely deterministically driven. Finally, in Sec. 5.7 we concluded with future directions of the presented work.

5.2 Model Details

The interaction of an external field with a reactant species can strongly influence the mechanism and rate of a reaction [144, 86, 87]. As a paradigmatic example of a chemical reaction

driven under kinetic control, we consider a particle of unit mass moving along a reaction coordinate x. The trajectory of the particle begins at a position x_0 on the reactant side of an energy barrier that is moving in space under the influence of a time-dependent external field $E(t)$. The chosen potential surface is the quartic form

$$U(x) = -\tfrac{1}{2}\omega_{\mathrm{b}}^2(x - E(t))^2 - \tfrac{1}{4}\epsilon(x - E(t))^4. \tag{117}$$

The time dependent, instantaneous position of the moving barrier top (BT) is specified by $E(t)$.

With the inclusion of additional non-conservative dissipation as well as stochastic driving forces, a particle moving in the potential (117) can be described by the Langevin equations of motion

$$\begin{aligned} \dot{x} &= v, \\ \dot{v} &= -\gamma v + \omega_{\mathrm{b}}^2(x - E(t)) + \epsilon(x - E(t))^3 + \sqrt{2\sigma}\,\xi(t), \end{aligned} \tag{118}$$

where $\gamma \geq 0$ is a dissipation parameter, ω_{b} is the barrier frequency, and ϵ is an anharmonic coefficient. Thus, for $\epsilon \neq 0$ the coordinate of the particle is non-linearly coupled to the moving barrier. By restricting the anharmonic coefficient to values $\epsilon \geq 0$, there is a single maximum in the potential located at the BT. The random fluctuating force $\xi(t)$ is Gaussian white noise obeying the statistical properties

$$\langle \xi(t) \rangle = 0 \quad \text{and} \quad \langle \xi(t)\xi(t') \rangle = \delta(t - t'). \tag{119}$$

The strength of the noise is varied through the parameter $\sigma \geq 0$.

Depending on the geometry of $U(x)$, initial conditions, as well as the specific realization of the thermal environment and the external field, a trajectory will either surmount the energy barrier and form product or remain on the reactant side. The reaction rate for a system evolving through (118) can be obtained by calculating the normalized flux of *reactive* trajectories through the the TS [133].

In this article, we consider periodic external driving of the form

$$E(t) = a \prod_{\omega \in \mathbf{\Omega}_s} \sin(\omega\, t + \varphi). \tag{120}$$

where $\mathbf{\Omega}_s \subset \mathbb{R}$ is a finite set of frequencies. The waveforms consist of a fundamental frequency Ω, and convolutions of this fundamental with higher order partial frequencies. Three frequency sets $\mathbf{\Omega}_s$ are considered: the single fundamental frequency $\mathbf{\Omega}_1 = \{\Omega\}$, the fundamental and the second partial $\mathbf{\Omega}_2 = \{\Omega, 2\Omega\}$, and the fundamental, second, and third partials $\mathbf{\Omega}_3 = \{\Omega, 2\Omega, 3\Omega\}$. The fundamental driving frequency Ω_f is Ω for the $\mathbf{\Omega}_1$ and $\mathbf{\Omega}_2$ sets, and 2Ω for the $\mathbf{\Omega}_3$ set. The products in Eq. (120) can be written as finite sums

$$\begin{aligned} E_1(t) &= a\sin(\Omega t + \varphi), \\ E_2(t) &= \frac{a}{2}(\cos(\Omega t) + \cos(3\Omega t + 2\varphi)), \\ E_3(t) &= \frac{a}{4}(\sin(2\Omega t + \varphi) + \sin(4\Omega t + \varphi) \\ &\quad + \sin(6\Omega t + 3\varphi) + \sin(\varphi)), \end{aligned} \tag{121}$$

where the leading order terms show the characteristic fundamental frequency. The amplitude of each waveform is set to unity by changing the value of the parameter a. For the $\mathbf{\Omega}_1$, $\mathbf{\Omega}_2$, and $\mathbf{\Omega}_3$ sets, $a = 1$, $a \approx 1.299$, and $a \approx 1.822$, respectively. The functional forms of (121) are shown in Fig. 34.

5.3 The Transition State Trajectory

The construction and existence of a structure whose configuration space projection is free of recrossings is dependent on the mechanism and geometry of a given reaction. For example, Mullen *et al.* have proposed that for ion-pair dissociation a no-recrossings DS does not exist [139, 138]. We have previously shown that for a periodically driven system with no thermal driving, an optimal DS can be readily obtained as an unstable PO in the region of the BT [29]. Moreover, a DS that is free of recrossings is known to exist in thermally driven systems for the case of a harmonic barrier [10, 13]. The time evolution of the configuration space projection of this DS has been termed the transition state trajectory [10, 13, 12, 159, 11, 29, 28]. While not necessarily unique with respect to the no recrossings criterion over finite time intervals, i.e., there may be other objects that are free of recrossings over an arbitrary time interval where the population dynamics are sampled, the configuration projection of the TS trajectory defines a DS that is recrossing-free.

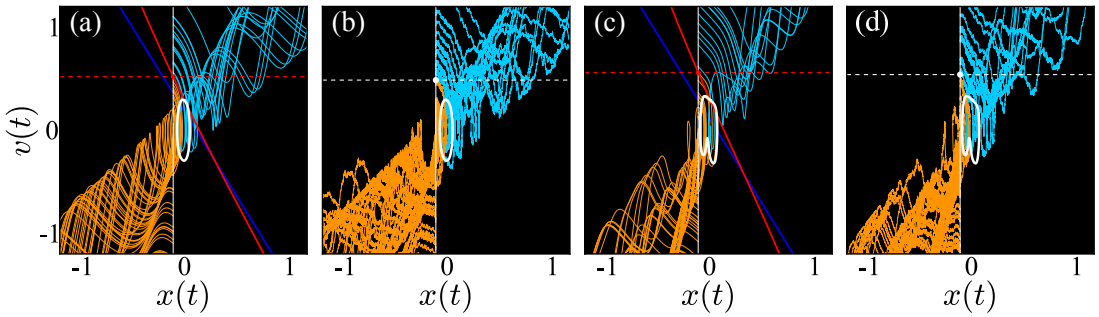

Figure 35: Phase space plots for a swarm of trajectories following the equations of motion (118) with various driving frequency sets and parameter values: $\mathbf{\Omega}_1$ with $\Omega_f = 5$ and $\epsilon = 1$ for (a) $\sigma = 0$ (noiseless) and (b) $\sigma = 0.025$ (thermal) driving, $\mathbf{\Omega}_3$ with $\Omega_f = 4$ and $\epsilon = 3$ for (c) $\sigma = 0$ and (d) $\sigma = 0.025$. The initial position for every trajectory, $x_0 = -0.1$, is shown as a vertical solid white line. Reactive trajectories are colored in cyan and nonreactive trajectories are colored in orange. The TS trajectory $\mathbf{\Gamma}^\ddagger$ is shown as a solid white curve. The critical velocity $V^\ddagger$ is indicated by a circle at the intersection of the dashed horizontal line and the line of initial conditions. The solid red curve is the critical curve $V_c^\ddagger$ and the solid blue curve is the harmonic critical curve $V_c^\ddagger|_{\epsilon=0}$. Parameters for all panels are $\gamma = 1$ and $\varphi = 0$ in dimensionless units.

The TS trajectory is a specific trajectory that never descends into either the product or reactant regions, remaining bounded to BT for all time. For the the system (118) it is a moving saddle point and thus has attached stable and unstable manifolds. As illustrated in Fig. 36, the TS trajectory does not follow the time evolution of the energetic maximum given by the BT. All trajectories that exponentially approach the TS trajectory as $t \to \infty$ are contained on the stable manifold. These trajectories will never descend from the BT region and therefore separate reactive from nonreactive trajectories in phase space. The unstable manifold is formed of trajectories that approach the TS trajectory as $t \to -\infty$. The role of the unstable manifold is less important for the purposes considered here.

For an arbitrary driving $E(t)$ of a harmonic ($\epsilon = 0$) potential the equations of motion can be solved exactly and an exact form of the TS trajectory can be obtained. The eigenvalues of (118)

$$\lambda_{s,u} = -\frac{1}{2}\left(\gamma \pm \sqrt{\gamma^2 + 4\omega_b^2}\right), \tag{122}$$

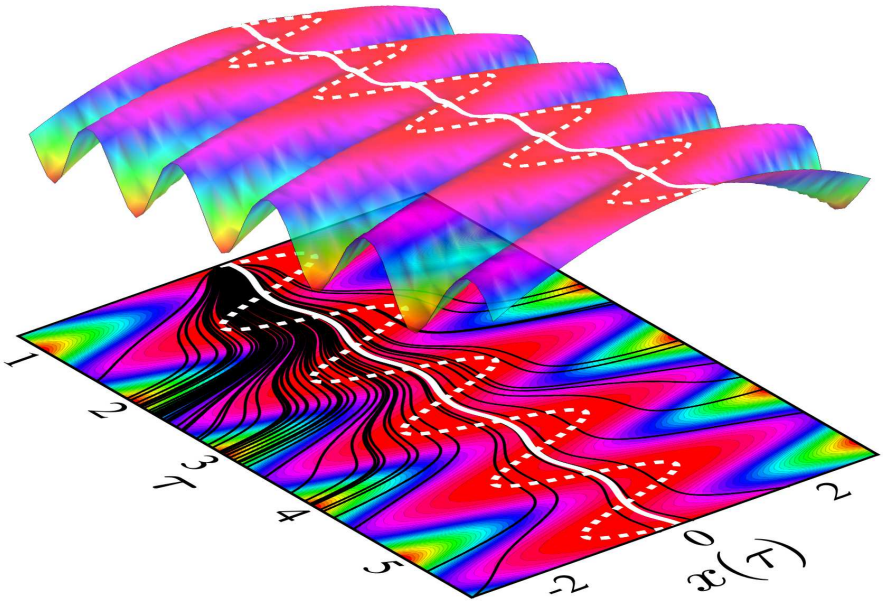

Figure 36: The time evolution of $x(t)$ for a swarm of 75 trajectories following the equations of motion (118) with $E(t) = a\sin(\Omega t + \varphi)$ are shown in black (below). The trajectories are superimposed on a contour plot of the potential energy surface created by the time evolution of Eq. (117). A three dimensional image of the potential surface is shown above. The trajectory of the instantaneous barrier top is shown in dashed white. The transition state trajectory is shown in solid white. Time is shown in units of $\tau = \Omega t/2\pi + 3/4$. All trajectories start at an initial position $x_0 = -0.1$ to the left of the instantaneous barrier top. The initial velocity v_0 is sampled from a Boltzmann distribution. Parameters are $\omega_{\rm b} = 1$, $k_{\rm B}T = 1$, $\epsilon = 1$, $\Omega = 3$, $\gamma = 4$, $a = 1$, and $\varphi = 0$ in dimensionless units.

correspond to the stable and unstable manifolds. The S functionals [13, 86]

$$S_\tau[\mu, g; t] = \begin{cases} -\displaystyle\int_t^\infty g(\tau)\, \exp(\mu(t-\tau))\, d\tau \quad : \ \mathrm{Re}\,\mu > 0, \\ \\ +\displaystyle\int_{-\infty}^t g(\tau)\, \exp(\mu(t-\tau))\, d\tau \quad : \ \mathrm{Re}\,\mu < 0, \end{cases} \tag{123}$$

obtained as a Green's function solution, suppress the transient exponential factor in the solution and return only the equilibrium portion. In the absence of thermal driving ($\sigma = 0$), the TS trajectory for a harmonic barrier can therefore be expressed as [159, 11, 29, 28]

$$\begin{aligned} x^\ddagger(t) &= \frac{\omega_\mathrm{b}^2}{\lambda_\mathrm{u} - \lambda_\mathrm{s}} \left(S[\lambda_\mathrm{s}, E; t] - S[\lambda_\mathrm{u}, E; t] \right), \\ v^\ddagger(t) &= \frac{\omega_\mathrm{b}^2}{\lambda_\mathrm{u} - \lambda_\mathrm{s}} \left(\lambda_\mathrm{s} S[\lambda_\mathrm{s}, E; t] - \lambda_\mathrm{u} S[\lambda_\mathrm{u}, E; t] \right). \end{aligned} \tag{124}$$

For the case of T-periodic motion of a harmonic barrier, the TS trajectory can be identified more easily by looking for a bounded solution to the equations of motion. For the single frequency $\mathbf{\Omega}_1$ case, the ansatz

$$x_1^\ddagger(t) = A \sin(\Omega t + \varphi) + B \cos(\Omega t + \varphi), \tag{125}$$

yields the solution

$$A = A_1, \qquad B = B_1, \tag{126}$$

where

$$\begin{aligned} A_k &= a\, \frac{\omega_\mathrm{b}^2(\omega_\mathrm{b}^2 + (k\Omega)^2)}{(\gamma k\Omega)^2 + (\omega_\mathrm{b}^2 + (k\Omega)^2)^2}, \\ B_k &= a\, \frac{\omega_\mathrm{b}^2 \gamma k\Omega}{(\gamma k\Omega)^2 + (\omega_\mathrm{b}^2 + (k\Omega)^2)^2}. \end{aligned} \tag{127}$$

In the absence of friction, $\gamma = 0$, this simplifies to

$$A_1 = a\, \frac{1}{1 + \Omega^2/\omega_\mathrm{b}^2}, \qquad B_1 = 0. \tag{128}$$

In this case the TS trajectory will oscillate in phase with the barrier, but with smaller amplitude $A_1 < a$.

For the $\mathbf{\Omega}_2$ and $\mathbf{\Omega}_3$ cases, ansätze can be constructed through Fourier series expansion of Eq. (120) yielding the solutions

$$\begin{aligned} x_2^\ddagger(t) = \tfrac{1}{2}(&A_1 \cos(\Omega t) - B_1 \sin(\Omega t) \\ &- A_3 \cos(3\Omega t + 2\varphi) + B_3 \sin(3\Omega t + 2\varphi)), \end{aligned} \tag{129}$$

in the $\mathbf{\Omega}_2$ case and

$$\begin{aligned} x_3^{\ddagger}(t) = \tfrac{1}{4}(&A_2\sin(2\Omega t+\varphi) + B_2\cos(2\Omega t+\varphi) \\ &+ A_4\sin(4\Omega t+\varphi) + B_4\cos(4\Omega t+\varphi) \\ &- A_6\sin(6\Omega t+3\varphi) - B_6\cos(6\Omega t+3\varphi) \\ &+ a\sin(\varphi)), \end{aligned} \tag{130}$$

in the $\mathbf{\Omega}_3$ case.

For periodically driven anharmonic barriers ($\epsilon \neq 0$), as in the harmonic case, the TS trajectory is an unstable PO [29], however in this case the system of equations (118) cannot be solved exactly. Let $\mathbf{\Gamma} = (x, v)$ represent a point in phase space. The phase space vector of the TS trajectory $\mathbf{\Gamma}^{\ddagger} = (x^{\ddagger}(t), v^{\ddagger}(t))$ is a bounded solution to the equations of motion. To find this bounded solution, numerical Newton-Raphson root finding methods were applied although perturbation theories have been previously employed [159, 11].

The dynamics of $x^{\ddagger}(t)$ are illustrated in Fig. 34, showing that the TS trajectory does not correspond to the energetic maximum of the potential surface. For dissipative systems ($\gamma \neq 0$), $x^{\ddagger}(t)$ will either lag behind in phase, as is the case for both the $\mathbf{\Omega}_1$ and $\mathbf{\Omega}_3$ sets, or advance in phase as is the case for the $\mathbf{\Omega}_2$ set, with respect to motion defined by $E(t)$. Also note that $x^{\ddagger}(t)$ oscillates with a smaller amplitude than $E(t)$. Thus, even for in-phase oscillations, e.g., when $\gamma = 0$, it will not correspond to the location of an energetic saddle point. Figure 34 also shows the dependence of $x^{\ddagger}(t)$ on the anharmonic parameter ϵ. As ϵ is increased, the curvature of the energy barrier also increases. Non-intuitively, this results in a larger amplitude of oscillation for $x^{\ddagger}(t)$ to remain bounded to the BT. This trend persists for all $\mathbf{\Omega}_s$.

Shown in Fig. 37 and Fig. 38 is the time evolution of $x(t)$ and $v(t)$ for a set of trajectories starting at some point x_0 to the left of the barrier. Specifically, the potential (117) describes an inverted (an)harmonic oscillator. Most trajectories quickly move away from the DS in accordance with the unstable nature of the PO.

For dynamical analysis it is advantageous to introduce a coordinate system which has

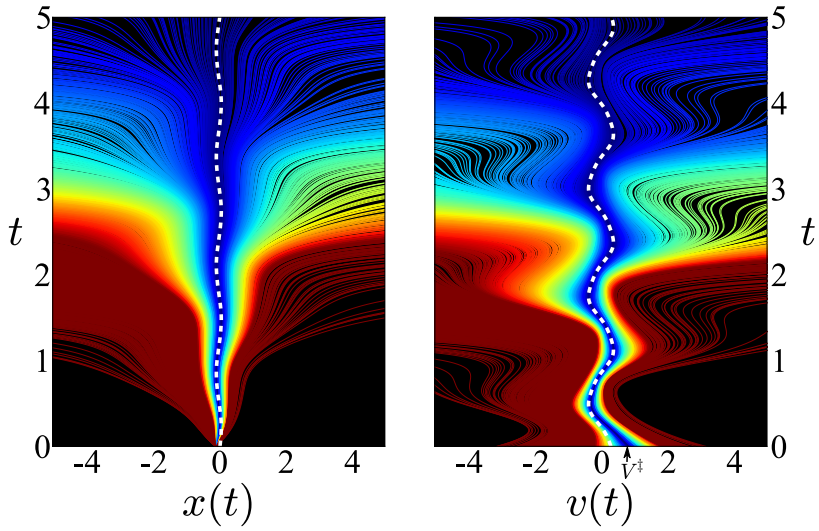

Figure 37: Time evolution of $x(t)$ (left) and $v(t)$ (right) for a swarm of 2000 trajectories following the equations of motion (118). The transition state trajectory (TS) is shown in dashed white. The trajectories are colored according to the difference in initial velocity, $\left|V^{\ddagger} - v_0\right|$, with respect to the critical velocity $V^{\ddagger}$ as marked. The colors range from dark blue to dark red (or black to gray in grayscale) and are scaled, increasingly, by this difference. Parameters are $\epsilon = 2$, $\Omega = 5$, $\gamma = 3$, $a = 1$, and $\varphi = 0$.

a fixed point at the origin. In relative coordinates

$$\Delta x = x - x^{\ddagger}(t), \qquad \Delta v = v - v^{\ddagger}(t), \tag{131}$$

the equations of motion read

$$\begin{aligned} \Delta\dot{x} &= \Delta v, \\ \Delta\dot{v} &= -\gamma\Delta v - U'(\Delta x + x^{\ddagger}(t)) + U'(x^{\ddagger}(t)). \end{aligned} \tag{132}$$

The relative equations of motion have a fixed point $\Delta\mathbf{\Gamma}^{\star}$ at $\Delta x = \Delta v = 0$, i.e., on the TS trajectory, and the surrounding vector field itself will now oscillate with period T, the same period as the driving. The TS trajectory has both a stable and an unstable manifold attached. In relative coordinates, the directions of these manifolds will depend on time.

5.4 Reaction Rate Theory

In the TST formalism, the rate of a chemical reaction is given by the time-dependence of the conversion process from reactant to product (R $\rightarrow$ P) where a DS in either configuration space or phase space separates the reactive constituents. The reaction rate can be obtained

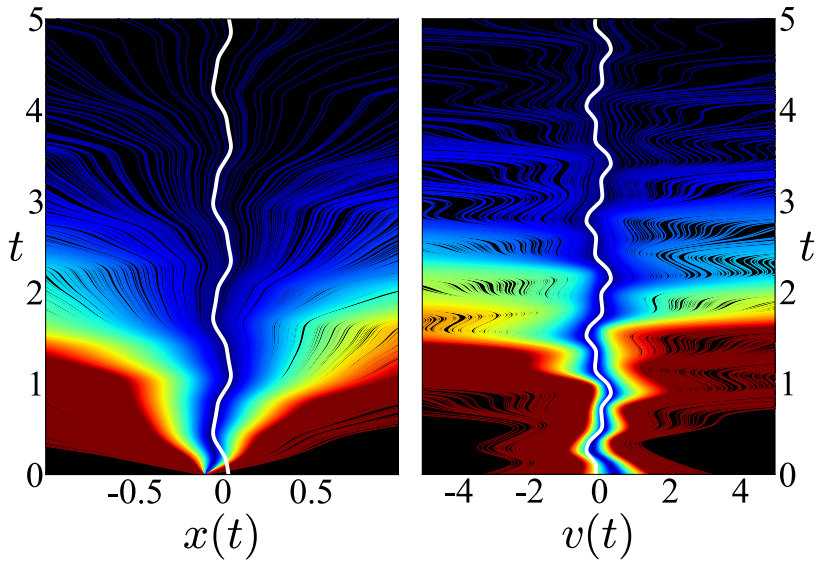

Figure 38: The time evolution of $x(t)$ (left) and $v(t)$ (right) for a swarm of 2000 trajectories following the equations of motion (118) with the frequency set $\mathbf{\Omega}_2$. All trajectories start at an initial position $x_0 = -0.1$ to the left of the instantaneous barrier top. The transition state trajectory (TS) is shown in white. The trajectories are colored according to the difference in initial velocity, $\left|V^{\ddagger} - v_0\right|$, with respect to the critical velocity $V^{\ddagger}$. The colors range from dark blue to dark red and are scaled, increasingly, by this difference. The coordinate $x(t)$ and velocity $v(t)$ for every individual trajectory are shown in matching colors. The initial velocity v_0 is sampled from a Boltzmann distribution. Parameters are $\omega_{\mathrm{b}} = 1$, $k_{\mathrm{B}}T = 1$, $\epsilon = 6$, $\Omega = 5$, $\gamma = 3$, $a = 1$, and $\varphi = 0$ in dimensionless units.

from the dynamics of the normalized reactive population ($P_{\mathrm{R}} \to P_{\mathrm{P}}$) either through analytical propagation of the phase space density of initial conditions or by treating large numbers of trajectories as discrete sets, and integrating the equations of motion.

Consider a set of trajectories evolving through (118) that all have initial positions $x_0 < x^{\ddagger}(0)$ on the reactant side of the moving surface. The initial position distribution at time $t = 0$ is $\delta(x - x_0)$ and the initial phase space density is

$$p_0(x, v) = \delta(x - x_0)\, q(v) \tag{133}$$

where $q(v)$ is a Boltzmann distribution. The initial velocity v_0 of each trajectory is sampled from $q(v)$, although at later times due to dissipation and driving this distribution will not be conserved. A fraction of this initial density contains reactive trajectories. From the survival probability of P_{R} the reaction rate can be expressed as the instantaneous flux-over-population, where the flux calculation is formally exact due to DS attached to the TS trajectory being recrossing-free.

5.4.1 Harmonic Barriers

When the barrier is harmonic ($\epsilon = 0$), reactive trajectories will cross the moving DS at a time [12]

$$t^{\ddagger} = \frac{1}{\lambda_{\mathrm{u}} - \lambda_{\mathrm{s}}} \ln\left(\frac{\Delta v_0 - \lambda_{\mathrm{u}} \Delta x_0}{\Delta v_0 - \lambda_{\mathrm{s}} \Delta x_0}\right). \tag{134}$$

The crossing time is a monotonically decreasing function of the initial velocity Δv_0: fast trajectories cross earlier. It diverges as $\Delta v_0 \to \lambda_{\mathrm{s}} \Delta x_0$ approaches the stable manifold, and it tends to zero as $\Delta v_0 \to \infty$.

At any time $t > 0$, the product region $\Delta x > 0$, to the right of the moving surface, will contain all those trajectories that cross the surface at a time $t^{\ddagger} < t$. These are the trajectories that have an initial velocity of at least $v_{\min} = v^{\ddagger}(0) + \Delta v_{\min}$, where $t^{\ddagger}(\Delta v_{\min}) = t$. From this condition we obtain

$$\Delta v_{\min} = \frac{\lambda_{\mathrm{u}} e^{-\lambda_{\mathrm{u}} t} - \lambda_{\mathrm{s}} e^{-\lambda_{\mathrm{s}} t}}{e^{-\lambda_{\mathrm{u}} t} - e^{-\lambda_{\mathrm{s}} t}}\, \Delta x_0. \tag{135}$$

The population of the product region at time t is therefore

$$P_{\mathrm{P}}(t) = \int_{v_{\min}(t)}^{\infty} q(v)\, dv, \tag{136}$$

and the flux across the moving surface is

$$\begin{aligned} F_{\mathrm{M}}(t) &= \frac{dP_{\mathrm{P}}}{dt} \\ &= -q(v_{\min}(t))\,\frac{dv_{\min}}{dt} \\ &= -q(v_{\min}(t))\,\frac{d\Delta v_{\min}}{dt} \\ &= -q(v_{\min}(t))\,\Delta x_0\,(\lambda_{\mathrm{u}}-\lambda_{\mathrm{s}})^2\,\frac{e^{(\lambda_{\mathrm{u}}+\lambda_{\mathrm{s}})t}}{(e^{\lambda_{\mathrm{u}}t}-e^{\lambda_{\mathrm{s}}t})^2}. \end{aligned} \tag{137}$$

This result is positive because $\Delta x_0 < 0$.

Alternatively, the flux can be calculated directly from the flux integral

$$F_{\mathrm{M}}(t) = \int_0^\infty d\Delta v\,\Delta v\,p_t(\Delta x = 0, \Delta v), \tag{138}$$

where $p_t(\Delta x, \Delta v)$ is the density of trajectories in phase space at time t. Initially, this density is

$$p_0(\Delta x, \Delta v) = \delta(\Delta x - \Delta x_0)\,q(v^\ddagger(0) + \Delta v). \tag{139}$$

At later times, it can be obtained from

$$p_t(\Delta x, \Delta v) = e^{\gamma t}\,p_0(\Delta x(-t), \Delta v(-t)). \tag{140}$$

Here $\Delta x(-t)$ and $\Delta v(-t)$ denote the phase space point reached from $\Delta x, \Delta v$ by propagating backwards to $-t$, i.e., it is the initial condition that has reached $\Delta x, \Delta v$ at time t. The exponential prefactor accounts for the shrinkage of phase space volume: The relative dynamics stretches distances at a rate λ_{u} in the u direction and by a rate $\lambda_{\mathrm{s}} < 0$ in the s direction. Volumes therefore are "stretched" at a constant rate $\lambda_{\mathrm{u}} + \lambda_{\mathrm{s}} = -\gamma < 0$, and densities must increase accordingly.

Because the relative dynamics is linear, the equations of motion can be solved explicitly. The result is

$$\begin{aligned} \Delta x(-t) &= a_x\,\Delta x + a_v\,\Delta v, \\ \Delta v(-t) &= b_x\,\Delta x + b_v\,\Delta v, \end{aligned}$$

with

$$a_x = \frac{\lambda_{\rm u}\, e^{-\lambda_{\rm s} t} - \lambda_{\rm s}\, e^{-\lambda_{\rm u} t}}{\lambda_{\rm u} - \lambda_{\rm s}}, \qquad a_v = \frac{e^{-\lambda_{\rm u} t} - e^{-\lambda_{\rm s} t}}{\lambda_{\rm u} - \lambda_{\rm s}} < 0,$$

$$b_x = -\frac{\lambda_{\rm u}\lambda_{\rm s}(e^{-\lambda_{\rm u} t} - e^{-\lambda_{\rm s} t})}{\lambda_{\rm u} - \lambda_{\rm s}}, \qquad b_v = \frac{\lambda_{\rm u}\, e^{-\lambda_{\rm u} t} - \lambda_{\rm s}\, e^{-\lambda_{\rm s} t}}{\lambda_{\rm u} - \lambda_{\rm s}}.$$

We thus obtain the flux integral

$$\begin{aligned} F_{\rm M}(t) &= e^{\gamma t} \int_0^\infty d\Delta v\, \Delta v\, \delta(a_v\, \Delta v - x_0)\, q(v^\ddagger(0) + b_v\, \Delta v) \\ &= e^{\gamma t} \int_0^\infty d\Delta v\, \Delta v\, \frac{\delta\left(\Delta v - x_0/a_v\right)}{|a_v|}\, q(v^\ddagger(0) + b_v\, \Delta v) \\ &= \frac{e^{\gamma t}}{-a_v}\, \frac{x_0}{a_v}\, q\left(v^\ddagger(0) + b_v/a_v\, x_0\right), \end{aligned} \tag{141}$$

which can be shown to agree with Eq. (137).

In the limit $t \to \infty$, the minimum velocity (135) is approximately

$$\begin{aligned} \Delta v_{\rm min} \;\; &= \;\; \lambda_{\rm s}\, \Delta x_0 - (\lambda_{\rm u} - \lambda_{\rm s}) \Delta x_0\, e^{-(\lambda_{\rm u} - \lambda_{\rm s}) t} \\ &\quad + \mathcal{O}\left(e^{-2(\lambda_{\rm u} - \lambda_{\rm s}) t}\right). \end{aligned} \tag{142}$$

As expected, it tends to $\lambda_{\rm s}\, \Delta x_0$, which is the location of the stable manifold. Therefore,

$$v_{\rm min}(\infty) = v^\ddagger(0) + \lambda_{\rm s}\, \Delta x_0 = V^\ddagger. \tag{143}$$

The critical velocity $V^\ddagger$ is determined by the point of intersection between the stable manifold and the line $x = x_0$ of initial conditions [159, 11]. The identification of $V^\ddagger$ allows the separation of reactive ($v_0 > V^\ddagger$) and nonreactive trajectories ($v_0 < V^\ddagger$) from initial conditions. The stable manifold at $t = 0$ can be calculated through extension of this point to all values of x_0 and defines a critical curve $V_c^\ddagger$. As illustrated in Figs. 35(a) and 35(c), $V_c^\ddagger$ is a time-invariant phase space object which separates the reactive and nonreactive basins.

Fig. 39 illustrates trajectories for various strengths of the anharmonicity. The critical velocity, shown as a red circle, marks the boundary between reactive and nonreactive trajectories. The reactive trajectories trace the forward branch of the unstable manifold while the nonreactive trajectories trace the backward branch. The location of a trajectory's initial velocity with respect to $V^\ddagger$ decides which branch the trajectory follows as it moves toward

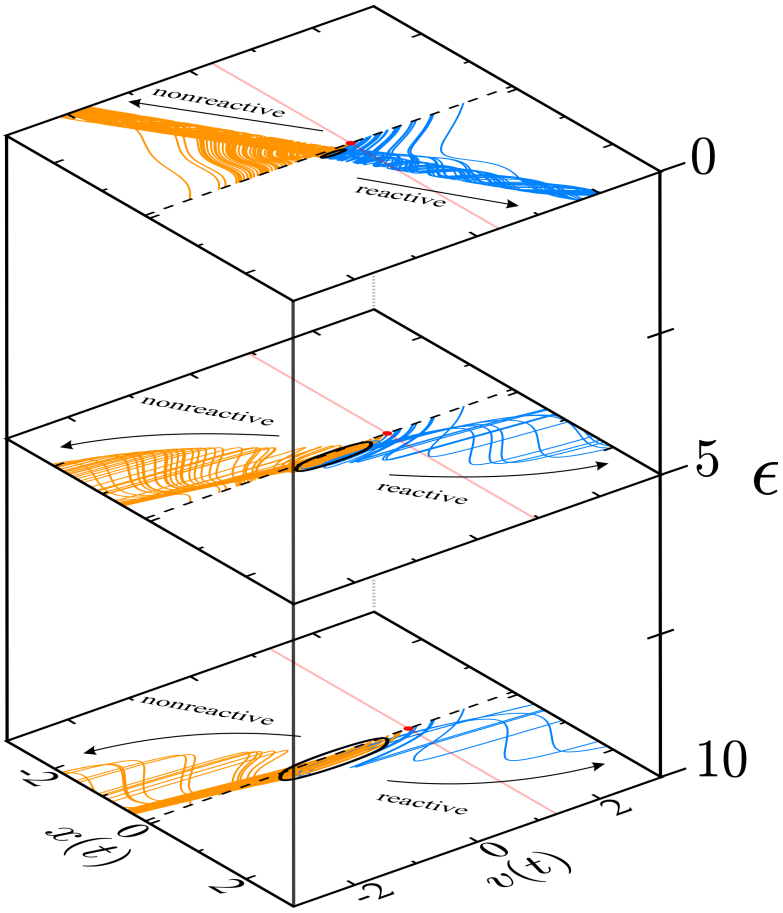

Figure 39: A swarm of 100 trajectories starting at x_0 (dashed black line) propagated by Eq. (118) at $\epsilon = 0$, 5 and 10. Reactive and nonreactive trajectories are identified by labeled arrows. The TS trajectory is a periodic orbit in solid black. The critical velocity $V^{\ddagger}$ lies at the vertex of x_0 and the grey (red) line. Parameters are $\Omega = 5$, $\gamma = 1$, $a = 1$, and $\varphi = 0$.

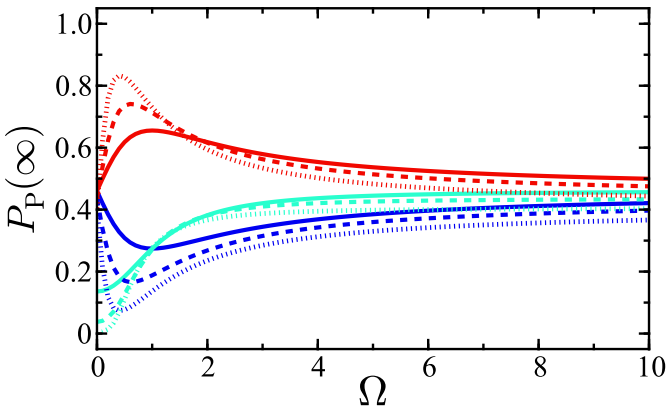

Figure 40: The asymptotic product population $P_{\rm P}(\infty)$ of the harmonic potential ($\epsilon = 0$) as a function of driving frequency Ω for the $\mathbf{\Omega}_1$ frequency set. The curves are colored with respect to the the value of the initial phase shift: $\varphi = 0$ (blue), $\varphi = \pi/2$ (cyan), and $\varphi = \pi$ (red). For each value of φ, the dependency of the asymptotic population on the friction parameter γ is shown by varying the linestyle: $\gamma = 0$ (solid), $\gamma = 1$ (dashed), and $\gamma = 2$ (dotted).

its final state. It can also be seen in Fig. 39 that $V^\ddagger$ increases with increasing ϵ, and thus increasing the anharmonicity decreases the amount of product formed. This increase in $V^\ddagger$ is due to the curvature in the stable and unstable manifolds that is induced by anharmonicity.

The product population in the long-time limit is

$$P_{\rm P}(\infty) = \int_{v^\ddagger(0)+\lambda_{\rm s}\,\Delta x_0}^{\infty} q(v)\,dv. \tag{144}$$

As shown in Fig. 40, the asymptotic population of the product region depends strongly on the frequency of the barrier motion Ω, the initial phase φ, and the friction γ. The asymptotic value is approached according to

$$\begin{aligned} P_{\rm P}(t) &= P_{\rm P}(\infty) - \int_{v_{\rm min}(\infty)}^{v_{\rm min}(t)} q(v)\,dv \\ &= P_{\rm P}(\infty) + q(v_{\rm min}(\infty))\,(\lambda_{\rm u} - \lambda_{\rm s})\,\Delta x_0\,e^{-(\lambda_{\rm u}-\lambda_{\rm s})t} \\ &\quad + \mathcal{O}\left(e^{-2(\lambda_{\rm u}-\lambda_{\rm s})t}\right). \end{aligned} \tag{145}$$

The rate of approach, i.e., the barrier crossing rate is

$$\lambda_{\rm u} - \lambda_{\rm s} = \sqrt{\gamma^2 + 4\omega_{\rm b}^2}. \tag{146}$$

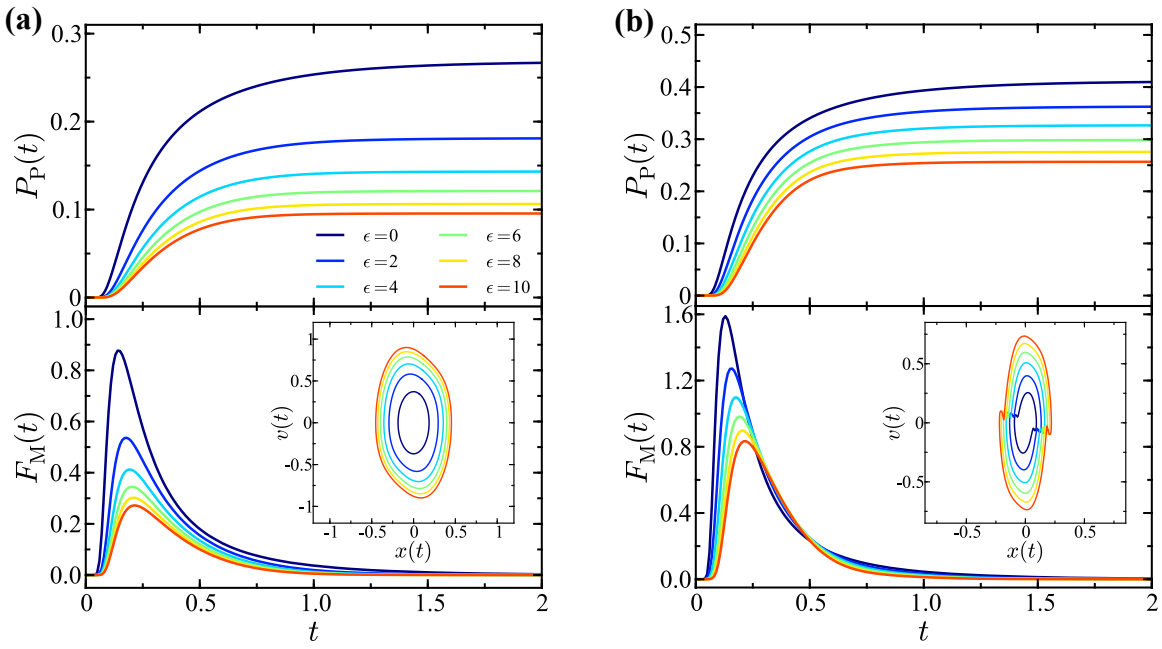

Figure 41: (a) Product population shown as a function of time for frequency set $\mathbf{\Omega}_1$ with varying anharmonicity ϵ (top). Flux through the moving DS as given by Eq. 150 (bottom). Inset are phase space plots of the transition state trajectories (TS). (b) Product population shown as a function of time for frequency set $\mathbf{\Omega}_2$ with varying anharmonicity ϵ (top). Flux through the moving DS with inset plots of TS trajectories (bottom). Coloring is the same as (a). Parameters for all panels are $\omega_{\mathrm{b}} = 1$, $k_{\mathrm{B}}T = 1$, $\Omega = 2$, $\gamma = 1$, $a = 1$, and $\varphi = 0$ in dimensionless units.

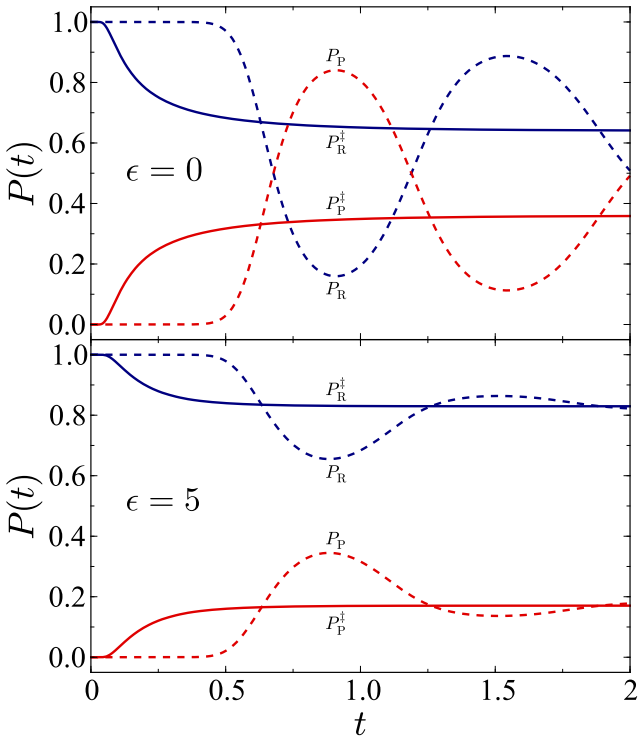

Figure 42: Time dependence of the reactant $P_{\rm R}$ and product $P_{\rm P}$ populations for harmonic and anharmonic barriers obtained relative to the instantaneous barrier top (dashed lines) and the TS trajectory (solid lines). All other parameters as in Fig. 39.

It depends only on the damping and the shape of the barrier, but not on the details of the barrier motion or the distribution of initial conditions (unless $q(v_{\rm min}(\infty))$ happens to vanish).

To test that the DS is recrossing-free, we simulated ensembles of 10^6 trajectories with an initial position $x_0 = -0.1$ to the left of the instantaneous barrier top and initial velocities sampled from a Boltzmann distribution. For every time t we compute the normalized reactant population $P_{\rm R}(t)$ and the normalized product population $P_{\rm P}(t)$. The time evolution of $P_{\rm R}(t)$ for varying parameters values is shown in Fig. 41. The harmonic case is shown in Fig. 41(a) and the anharmonic case is shown in Fig. 41(b). In all cases, the DS is free of recrossings, as is evident from the observation that the reactant populations decrease monotonically.

This is in stark contrast to the reactant and product populations that are obtained from a DS attached to the instantaneous barrier top. That surface can be recrossed many

times. As a consequence, reactant and product populations determined from this surface are not monotonic, but show pronounced oscillations as a function of time, as shown in Fig. 42. Using the instantaneous barrier top as a DS, in accordance with the canonical view of the transition state, an observer would alternatingly overestimate and underestimate the reactive portion of the ensemble of initial conditions. Populations obtained from the recrossing-free DS not only converge faster to their long-time asymptotic values, they also approach these values monotonically and thereby provide rigorous upper or lower bounds for the limiting values.

5.4.2 Anharmonic Barriers

Analogous to the harmonic case, for an anharmonic barrier we assume that there is a unstable PO with the period of the driving. This is similar to the POs used by Lehmann *et al* [104, 105, 103]. for the case thermal activation with included additive periodic driving. Note that this TS trajectory $\mathbf{\Gamma}^{\ddagger}$ is an exact solution to the equations of motion. As $\mathbf{\Gamma}^{\ddagger}$ is an unstable PO, it has stable and unstable manifolds attached. The manifolds are uniquely defined and can be calculated perturbatively [159, 11] or with a numerical scheme. The dependence of these manifolds on ϵ and the corresponding phase space reaction dynamics are shown in Figs. 35(a) and 35(c). With increasing anharmonicity, $V^{\ddagger}$ also increases due to curvature in the stable manifold. This results in a decrease in fraction of trajectories that that surmount the barrier and form product.

The nonlinear equations of motion (132) cannot, in general, be solved exactly. Let

$$\mathbf{\Phi}(\mathbf{\Gamma}_0, t_0; t) = \begin{pmatrix} \varphi_x(\mathbf{\Gamma}_0, t_0; t) \\ \varphi_v(\mathbf{\Gamma}_0, t_0; t) \end{pmatrix} \tag{147}$$

represent the phase space point that is reached at time t by a trajectory that starts at $\mathbf{\Gamma}_0$ at time t_0. Because of the external driving, it depends on t and t_0 separately, not only on the difference $t - t_0$. The Jacobian matrix of this trajectory with respect to the initial conditions is

$$\boldsymbol{J}(\mathbf{\Gamma}_0, t_0; t) = \begin{pmatrix} \dfrac{\partial \varphi_x}{\partial x_0} & \dfrac{\partial \varphi_x}{\partial v_0} \\ \dfrac{\partial \varphi_v}{\partial x_0} & \dfrac{\partial \varphi_v}{\partial v_0} \end{pmatrix}. \tag{148}$$

All derivatives on the right hand side of (148) are to be evaluated at $(\mathbf{\Gamma}_0, t_0; t)$.

Reactive trajectories are those that have an initial velocity $v_i > V^\ddagger$, where the critical velocity $V^\ddagger$ is measured at x_0. Each reactive trajectory will cross the moving DS at a time $t_c(\Delta v_i)$ and with a velocity v_c. If the the crossing time decays monotonically from $t_c(\Delta V^\ddagger) = \infty$ to $t_c(\infty) = 0$ the inverse function $\Delta v_i(t_c)$ or $v_i(t_c) = v^\ddagger(0) + \delta v_i(t_c)$ can be obtained. For any crossing time $t_c > 0$, there is a unique initial velocity v_i that will lead to a crossing at the given time.

The population of the product region $\Delta x > 0$ at time t_f is therefore, as in Eq. (136),

$$P_{\mathrm{P}}(t_c) = \int_{v_i(t_c)}^{\infty} q(v)\, dv, \tag{149}$$

and the flux across the moving surface is

$$\begin{aligned} F_{\mathrm{M}}(t_c) &= \frac{dP_{\mathrm{P}}}{dt_c} \\ &= -q(v_i(t_c))\, \frac{dv_i}{dt_c} \\ &= -q(v_i(t_c))\, \frac{d\Delta v_i}{dt_c} \end{aligned} \tag{150}$$

This result is positive because the initial velocity is a decreasing function of the crossing time.

The flux can also be evaluated directly from the flux integral (138)

$$F_{\mathrm{M}}(t_c) = \int_0^{\infty} d\Delta v\, \Delta v\, p_{t_c}(\Delta x = 0, \Delta v), \tag{151}$$

where $p_t(\Delta x, \Delta v)$ is the density of trajectories in phase space at time t. Initially, this density is (Eq. (139))

$$p_0(\Delta x, \Delta v) = \delta(\Delta x - \Delta x_0)\, q(v^\ddagger(0) + \Delta v). \tag{152}$$

At later times, it can be obtained from Eq. (140)

$$p_t(\Delta x, \Delta v) = e^{\gamma t}\, p_0(\varphi_x(\Delta x, \Delta v, t; 0), \varphi_v(\Delta x, \Delta v, t; 0)). \tag{153}$$

Here we have used the general notation for the flow of the equation of motion. The exponential accounts for the shrinkage of phase space volume and the corresponding increase in

density. It is the same as in the harmonic case: In general, the flow of a differential equation $\dot{\boldsymbol{u}} = \boldsymbol{f}(\boldsymbol{u})$ leads to a stretching of volume whose rate is the divergence of the vector field $\boldsymbol{f}$. For Eq. (132), this rate is constant $-\gamma$, so that over time t all volumes will shrink by a factor $e^{-\gamma t}$.

The flux integral formula (138) now reads

$$F_{\mathrm{M}}(t_c) = e^{\gamma t_c} \int_0^\infty d\Delta v \, \Delta v \, \delta(\varphi_x(0, \Delta v, t_c; 0) - \Delta x_0) \; q(v^\ddagger(0) + \varphi_v(0, \Delta v, t_c; 0)). \tag{154}$$

The δ function requires that the trajectory that reaches $\Delta x = 0, \Delta v$ at time t_c must have started at Δx_0 at time 0. It produces a single contribution to the integral at velocity $\Delta v_c(t_c)$, so that

$$F_{\mathrm{M}}(t_c) = e^{\gamma t_c} \, q(v^\ddagger(0) + \Delta v_i(t_c)) \, \frac{\Delta v_c(t_c)}{\left| \frac{\partial \varphi_x}{\partial \Delta v_0} \Big|_{t_c} \right|}, \tag{155}$$

where $\varphi_v(0, \Delta v, t_c; 0) = \Delta v_i(t_c)$ and the subscript t_c indicates that the derivative is to be evaluated at $(0, \Delta v_c(t_c), t_c; 0)$. Similarly, a subscript 0 will be used to require evaluation at $(\Delta x_0, \Delta v_i(t_c), 0; t_c)$. These subscripts indicate derivatives of the flow taken along the trajectory from $(\Delta x_0, \Delta v_i(t_c))$ at $t = 0$ forward in time to $(0, \Delta v_c(t_c))$ at $t = t_c$ (subscript 0) and along the same trajectory backward in time (subscript t_c).

To verify that the flux integral (155) gives the same result as (150) that was obtained from the product population, it must be shown that

$$-\frac{d\Delta v_i}{dt_c} = e^{\gamma t_c} \, \frac{\Delta v_c(t_c)}{\left| \frac{\partial \varphi_x}{\partial \Delta v_0} \Big|_{t_c} \right|}. \tag{156}$$

To this end, first note that $\Delta v_i(t_c)$ is defined by the condition

$$\varphi_x(\Delta x_0, \Delta v_i(t_c), 0; t_c) = 0.$$

Differentiating this condition with respect to t_c gives,

$$\frac{\partial \varphi_x}{\partial \Delta v}\bigg|_0 \frac{d\Delta v_i}{dt_c} + \frac{\partial \varphi_x}{\partial t}\bigg|_0 = 0. \tag{157}$$

Now $\partial \varphi_x / \partial t$ is the velocity of the trajectory at the end point. The second term in Eq. (157) is therefore $\Delta v_c(t_c)$. With this result, the condition (156) simplifies to

$$-\frac{\partial \varphi_x}{\partial \Delta v}\bigg|_{t_c} = e^{\gamma t_c} \, \frac{\partial \varphi_x}{\partial \Delta v}\bigg|_0. \tag{158}$$

Under the given assumptions on the geometry, the derivative on the left hand side is negative: A trajectory that arrives at the DS with larger velocity must have started further away, i.e., at smaller $\Delta x(0)$.

The derivatives occurring in Eq. (158) are elements of the Jacobian matrices

$$\boldsymbol{J}|_{t_c} = \boldsymbol{J}(0, \Delta v_c(t_c), t_c; 0) = \begin{pmatrix} \left.\frac{\partial \varphi_x}{\partial x}\right|_{t_c} & \left.\frac{\partial \varphi_x}{\partial v}\right|_{t_c} \\ \left.\frac{\partial \varphi_v}{\partial x}\right|_{t_c} & \left.\frac{\partial \varphi_v}{\partial v}\right|_{t_c} \end{pmatrix}$$

and

$$\boldsymbol{J}|_{0} = \boldsymbol{J}(\Delta x_0, \Delta v_i(t_c), 0; t_c) = \begin{pmatrix} \left.\frac{\partial \varphi_x}{\partial x}\right|_{0} & \left.\frac{\partial \varphi_x}{\partial v}\right|_{0} \\ \left.\frac{\partial \varphi_v}{\partial x}\right|_{0} & \left.\frac{\partial \varphi_v}{\partial v}\right|_{0} \end{pmatrix}$$

respectively. Because these matrices describe variations around the same trajectory, taken forwards and backwards in time, they are inverse to each other. Formally, this can be shown by taking derivatives of the flow property

$$\boldsymbol{\Phi}(\boldsymbol{\Phi}(\boldsymbol{\Gamma}_0, 0; t_c), t_c; 0) = \boldsymbol{\Gamma}_0 \qquad \text{for all } \boldsymbol{\Gamma}_0,$$

which says that propagating an arbitrary phase space point $\boldsymbol{\Gamma}_0$ forward in time by t_c and back again will return the original point.

By the well known formula for the inverse of a 2×2 matrix, it follows that

$$\begin{aligned} \boldsymbol{J}|_{t_c} &= (\boldsymbol{J}|_0)^{-1} \\ &= \frac{1}{\det \boldsymbol{J}|_0} \begin{pmatrix} \left.\frac{\partial \varphi_v}{\partial v}\right|_{0} & -\left.\frac{\partial \varphi_x}{\partial v}\right|_{0} \\ -\left.\frac{\partial \varphi_v}{\partial x}\right|_{0} & \left.\frac{\partial \varphi_x}{\partial x}\right|_{0} \end{pmatrix}, \end{aligned}$$

so that

$$\left.\frac{\partial \varphi_x}{\partial \Delta v}\right|_{t_c} = -\frac{1}{\det \boldsymbol{J}|_0} \left.\frac{\partial \varphi_x}{\partial \Delta v}\right|_{0}.$$

Now

$$\det \boldsymbol{J}|_0 = e^{-\gamma t_c}$$

is the factor by which phase space volumes shrink during time t_c. This proves the condition (158) and therefore the equality of the two flux formulas.

5.4.3 Dynamics near the TS

The TS trajectory is a moving saddle point and thus trajectories in the neighborhood of $\mathbf{\Gamma}^\ddagger$ can be described by a linearization of the equations of motion. In the phase space vector relative coordinate $\Delta\mathbf{\Gamma} = (\Delta x, \Delta v)$ this linearization is given by

$$\Delta\dot{\mathbf{\Gamma}} = \boldsymbol{J}(t)\,\Delta\mathbf{\Gamma} \tag{159}$$

where

$$\boldsymbol{J}(t) = \begin{pmatrix} 0 & 1 \\ \omega_{\mathrm{b}}^2 + 3\epsilon(x^\ddagger(t) - E(t))^2 & -\gamma \end{pmatrix} \tag{160}$$

is the Jacobian of Eq. (132) about $\mathbf{\Gamma}^\ddagger$. The asymptotic decay rate of $P_{\mathrm{R}}(t)$ is determined by the behavior of trajectories with initial conditions close to the stable manifold. For an ensemble of trajectories constituting an initial phase space density p_0, trajectories that emanate close to $V_c^\ddagger$ (the stable manifold at $t = 0$) will persist in the neighborhood where (159) is valid for long times. The decay of these trajectories determines the the reaction rate.

The stretching and compression of phase space about a PO is known to dictate escape rates in conservative [84, 171, 56] and dissipative systems [28]. For systems of form (159) where $\boldsymbol{J}(t)$ is periodic, the rate of deformation of in the linearized phase space can be quantified through calculation of the Floquet exponents [172].

To classify the stability of $\Delta\mathbf{\Gamma}^\ddagger$ we consider the dynamics of a perturbation vector $\Delta\boldsymbol{\sigma}(t)$. The equation of motion (159) is linear in $\Delta\boldsymbol{\sigma}(t)$ and thus it satisfies

$$\Delta\dot{\boldsymbol{\sigma}} = \boldsymbol{J}(t)\,\Delta\boldsymbol{\sigma}, \quad \Delta\boldsymbol{\sigma}(0) = \boldsymbol{I}, \tag{161}$$

where $\boldsymbol{I}$ is the 2×2 identity matrix. The principal fundamental matrix solution over one period of the driving is the monodromy matrix

$$\boldsymbol{M} = \begin{pmatrix} \Delta\sigma^{(1)}(T) & \Delta\sigma^{(2)}(T) \\ \Delta\dot{\sigma}^{(1)}(T) & \Delta\dot{\sigma}^{(2)}(T) \end{pmatrix}. \tag{162}$$

A fundamental matrix solution $\Delta\boldsymbol{\sigma}(t)$ of (159) at some later time $t + kT$, for $k = 1, 2, 3\ldots$, can be obtained as

$$\Delta\boldsymbol{\sigma}(t + kT) = \boldsymbol{M}^k\Delta\boldsymbol{\sigma}(t), \tag{163}$$

through repeated operation by the monodromy matrix.

The eigenvalues $m_{\mathrm{s},u}$ of $\boldsymbol{M}$ are the Floquet multipliers. The Floquet exponents

$$\mu_{\mathrm{s},u} = \frac{1}{T} \ln |m_{\mathrm{s},u}| \tag{164}$$

quantify the stability of $\Delta\boldsymbol{\Gamma}^{\ddagger}$ and give the rate of expansion or contraction of the perturbation of per unit time [33, 16, 187]. The TS trajectory has both an unstable $\mu_u > 0$ and a stable $\mu_s < 0$ exponent which correspond to stretching and contraction of the initial perturbation in the directions of the unstable and stable manifolds, respectively.

Let $\boldsymbol{v}_{\mathrm{u,s}}(0)$ be the eigenvectors of $\boldsymbol{M}$. By Floquet's theorem and the positivity of the Floquet multipliers, the vectors

$$\boldsymbol{v}_{\mathrm{u,s}}(t) = e^{-\mu_{\mathrm{u,s}} t}\, \Delta\boldsymbol{\sigma}(t)\, \boldsymbol{v}_{\mathrm{u,s}}(0) \tag{165}$$

are periodic in time with period T. In the coordinate system defined by these vectors,

$$\Delta\boldsymbol{\Gamma}(t) = z_{\mathrm{u}}(t)\, \boldsymbol{v}_{\mathrm{u}}(t) + z_{\mathrm{s}}(t)\, \boldsymbol{v}_{\mathrm{s}}(t), \tag{166}$$

the linearized equations of motion (159) read

$$\dot{z}_{\mathrm{u,s}} = \mu_{\mathrm{u,s}}\, z_{\mathrm{u,s}}, \tag{167}$$

with the solution

$$z_{\mathrm{u,s}}(t) = C_{\mathrm{u,s}}\, e^{\mu_{\mathrm{u,s}} t}. \tag{168}$$

Therefore, the vectors $\boldsymbol{v}_{\mathrm{u,s}}(t)$ determine the instantaneous directions of the stable and unstable manifolds in the linear approximation. The actual stable and unstable manifolds are tangent to these directions at the TS trajectory.

According to Eq. (166), the dynamics of Eq. (159) is therefore given by

$$\Delta x(t) = C_{\mathrm{u}}\, \alpha_{\mathrm{u}}(t)\, e^{\mu_{\mathrm{u}} t} + C_{\mathrm{s}}\, \alpha_{\mathrm{s}}(t)\, e^{\mu_{\mathrm{s}} t}, \tag{169}$$

where $\alpha_{\mathrm{u,s}}$ are the first components of the vectors $\boldsymbol{v}_{\mathrm{u,s}}$. They are periodic with period T. A trajectory with given initial conditions C_{u} and C_{s} will cross the moving dividing surface $\Delta x = 0$ at time t determined by

$$e^{(\mu_{\mathrm{u}} - \mu_{\mathrm{s}})t} = -\frac{C_{\mathrm{s}}}{C_{\mathrm{u}}}\, \frac{\alpha_{\mathrm{s}}(t)}{\alpha_{\mathrm{u}}(t)}. \tag{170}$$

If the initial condition C_s is fixed and a trajectory with a certain value of C_u crosses the moving DS at time t, Eq. (170) shows that a trajectory with initial value $C_\mathrm{u}e^{(\mu_\mathrm{u}-\mu_\mathrm{s})T}$ will cross at time $t+T$. Iteration then leads to the existence of trajectiories with initial values $C_\mathrm{u}e^{(\mu_\mathrm{u}-\mu_\mathrm{s})nT}$ that cross at time $t+nT$.

For an arbitrary time interval of length T, trajectories that cross the DS in this interval form a strip in the phase plane. Trajectories that cross the DS in the next following time interval T form a similar strip that that is closer to the stable manifold. In the region where the linearized system is valid, the phase space density is constant. The flux of trajectories through the DS in a given time interval is proportional to the width of the strip that contains these trajectories. During sequential periods this width decreases by a factor $e^{-(\mu_u-\mu_s)t}$. From this it follows that, up to periodic modulation, the flux must decay as $e^{-(\mu_u-\mu_s)t}$ and the barrier crossing rate is

$$k_\mathrm{f} = \mu_u - \mu_s, \tag{171}$$

which expresses the reaction rate in terms of the characteristic Floquet exponents of the TS trajectory. Equation (171) generalizes Eq. (146) for the case of an anharmonic barrier.

5.5 Numerical Results and Comparison with Theory

The reaction rate of (118) was calculated by simulating ensembles of $n = 10^8 - 10^9$ trajectories for every set of parameters $\{\Omega, \gamma, \epsilon, \sigma\}$ and following the survival probability of P_R as a function of time. A Runge-Kutta-Maruyama scheme [140] was implemented to perform the integration. In the absence of noise ($\sigma = 0$), this algorithm is the well-known fourth-order Runga-Kutta method. For all numerical simulations non-dimensional parameters were used by choosing units such that the barrier frequency ω_b and driving amplitude are unity. Each trajectory was given an initial position $x_0 = -0.1$ (in the reactant region) and v_0 was sampled from a Boltzmann distribution with $k_\mathrm{B}T = 1$. The choice of initial conditions is arbitrary as the asymptotic decay rate of $P_\mathrm{R}(t)$ is independent of the choice of initial distribution, suffice that there is enough density about the stable manifold such that a rate exists [28].

The ensemble of n trajectories was evolved through the equations of motion (118). The

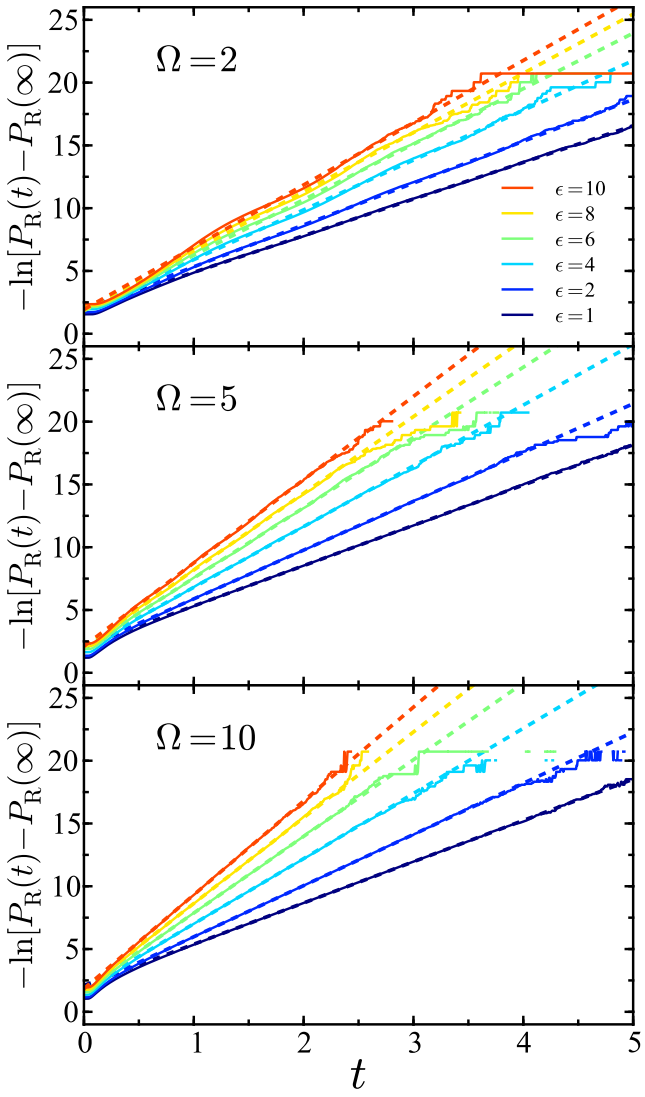

Figure 43: Time dependence of the scaled logarithm of the reactant population, $-\ln\left[P_{\mathrm{R}}(t) - P_{\mathrm{R}}(\infty)\right]$, for $\Omega = 2$ (top), $\Omega = 5$ (middle), and $\Omega = 10$ (bottom) using the $\mathbf{\Omega}_s^{(1)}$ frequency set. Values of the anharmonic parameter are $\epsilon \in \{1, 2, 4, 6, 8, 10\}$ with the reactive population $P_{\mathrm{R}}(t)$ calculated from integration of 10^9 trajectories for each value. Least squares fits to the non-transient section of the logarithmic curve are shown as dashed lines with colors corresponding to the respective ϵ values. The slope of the dashed line is barrier crossing rate k_{f}. Parameters are $\omega_{\mathrm{b}} = 1$, $k_{\mathrm{B}}T = 1$, $\gamma = 1$, $a = 1$, and $\varphi = 0$ in dimensionless units.

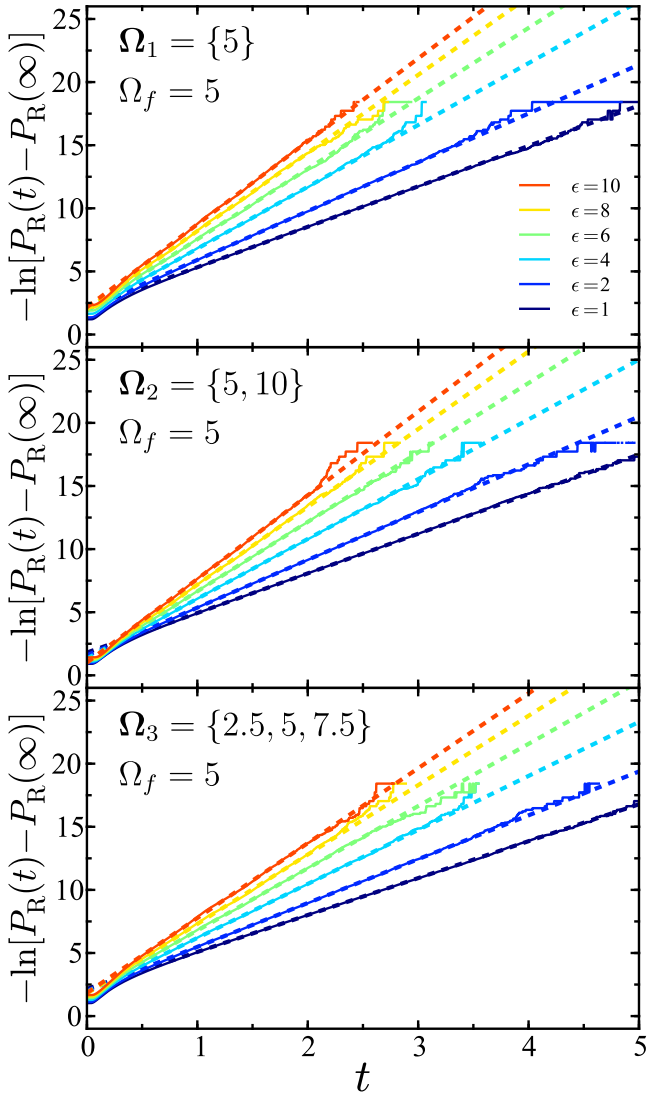

Figure 44: Time dependence of the scaled logarithm of the reactant population, $-\ln[P_{\rm R}(t) - P_{\rm R}(\infty)]$, for $\mathbf{\Omega}_1$ (top), $\mathbf{\Omega}_2$ (middle), and $\mathbf{\Omega}_3$ (bottom) with $\Omega_f = 5$ for all panels. Values of the anharmonic parameter are $\epsilon \in \{1, 2, 4, 6, 8, 10\}$. The slope of each dashed line is the barrier crossing rate $k_{\rm f}$. The color of each line corresponds to the respective ϵ value. In all panels, parameters are $\gamma = 1$ and $\varphi = 0$.

normalized reactant population was calculated at each time step in the integration scheme. An indicator function was employed to follow the state evolution of each trajectory,

$$h_{\mathrm{R}}[x(t)] = \begin{cases} 0, & x(t) > x^{\ddagger}(t) \ , \\ 1, & x(t) < x^{\ddagger}(t) \ , \end{cases} \tag{172}$$

where $x^{\ddagger}(t)$ is the configuration space projection of the TS trajectory. If for a specific trajectory i, $x_i(t) > x^{\ddagger}(t)$ that trajectory is in the product state and is not counted in the reactant population at time t. The instantaneous normalized population of the reactant region can be found by summing over all n trajectories and then normalizing by a factor $1/n$,

$$P_{\mathrm{R}}(t) = \frac{1}{n} \sum_{i=1}^{n} h_{\mathrm{R}}[x_i(t)]. \tag{173}$$

Trajectories can only exist in one of two states, reactant or product, and so the normalized product population $P_{\mathrm{P}} = 1 - P_{\mathrm{R}}$.

As shown in Figs. 43 and 44, for all frequency sets, the scaled logarithm of the normalized reactant population is approximately linear in time after an initial transient section implying a first-order rate process. The asymptotic reaction rate k_{f} can thus be found as the slope of the scaled logarithmic curve in the long-time limit. Periodic modulation in the decay of $P_{\mathrm{R}}(t)$ was found to become more prominent for low frequency driving ($\Omega_f \lessapprox 2$). In these cases the global exponential rate was calculated as an average over these modulations.

A comparison between the rates calculated from numerical simulation and rates predicted by Eq. (171) is shown in Fig. 45. For all frequency sets $\mathbf{\Omega}_s$ and parameter values, agreement is observed. Underdamped ($\gamma < 2$), overdamped ($\gamma > 2$), and critically damped ($\gamma = 2$) regimes of a corresponding harmonic well were considered. Agreement between the rates persists over all ranges of damping. For high frequency driving ($\Omega_f > \omega_{\mathrm{b}}$), the exponential rate can be averaged over several periods of driving and modulations in the decay are minimal, as illustrated in Fig. 44. Periodic modulations in the decay of $P_{\mathrm{R}}(t)$ are prominent for low driving frequencies ($\Omega_f \approx \omega_{\mathrm{b}}$) and the integration of $n = 10^8$ trajectories resulted in reaching the numerical asymptote $P_{\mathrm{R}}(\infty)$ at times less than the period of the external driving. In cases where the asymptotic region was not sufficiently sampled, a larger number

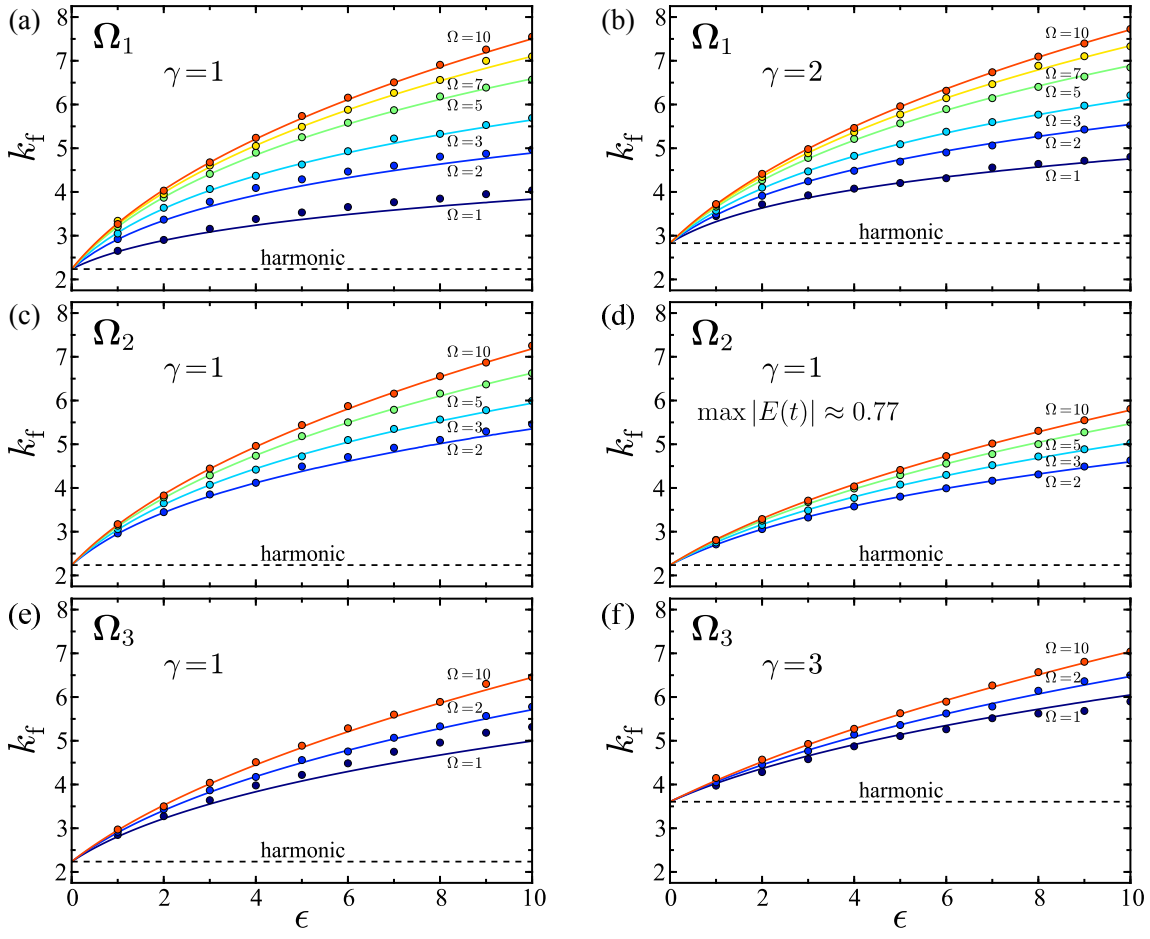

Figure 45: The barrier crossing rates of systems following the equations of motion (118) as a function the anharmonic parameter ϵ for various frequency sets $\mathbf{\Omega}_s$, driving frequencies Ω, and values of friction γ, as denoted in each panel. The circles denote the rates $k_{\rm f}$ calculated from the time evolution of $P_{\rm R}(t)$ through numerically simulation and correspond to the dashed lines in Fig. 44. The solid curves are the rates predicted by the difference in the characteristic Floquet exponents $\mu_{\rm u}-\mu_{\rm s}$ of the corresponding TS trajectory.

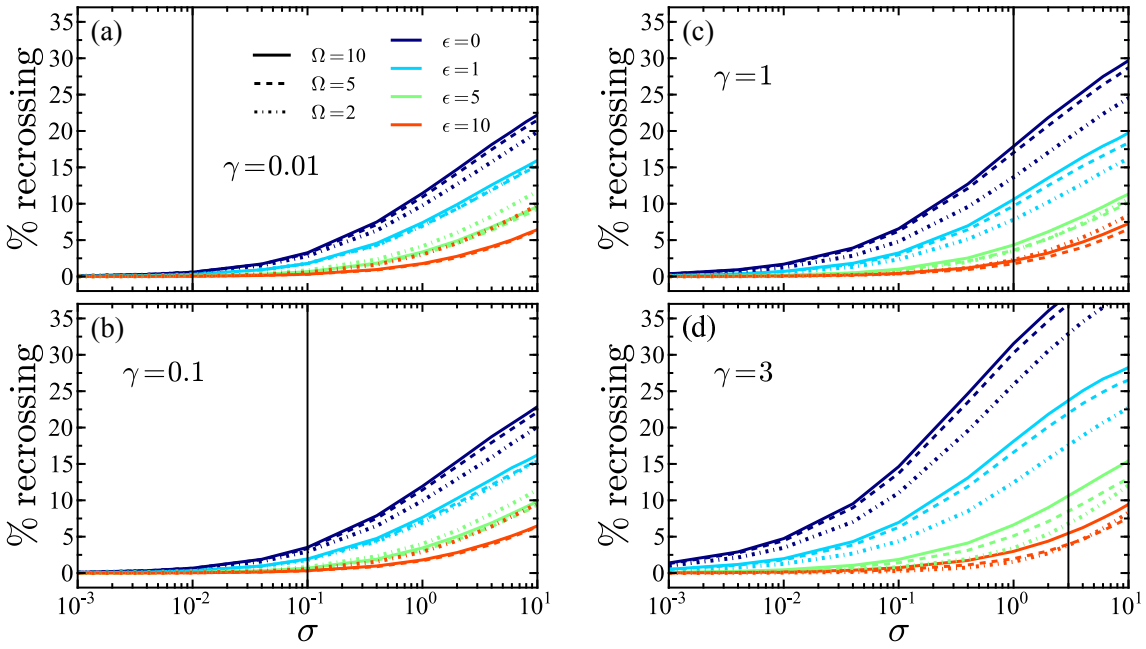

Figure 46: The percentage of trajectories that recross the moving dividing surface attached to the DTS trajectory as a function of noise strength σ with (a) $\gamma = 0.01$, (b) $\gamma = 0.1$, (c) $\gamma = 1$, and (d) $\gamma = 3$ for single-frequency ($\mathbf{\Omega}_1$) driving and various values of ϵ and Ω. The black vertical line (solid) denotes the noise strength where the fluctuation-dissipation theorem is obeyed.

of trajectories ($n = 10^9$) were integrated to extend this region to longer times. Increasing the number of trajectories by an order of magnitude resulted in a longer time window for sampling and as shown in Fig. 45(e), for $\Omega = 1$, marginally better agreement between the compared methodologies. In Fig. 45(d), the results for $\mathbf{\Omega}_2$ with a smaller, non-unity, driving amplitude are shown. The agreement between the two methods persists and, as expected, the decreased driving amplitude leads to a decrease in the reaction rate.

5.6 Characterizing Noisy Reactions with the Noise-Free Geometry

In systems in which the strength of an external driving force dominates over that of the thermal driving, statistical quantities can be approximated by those of a corresponding purely deterministically driven system. For thermally induced reactions, Lehmann, Hängii, and Reimann [104, 105, 103] have shown that in the overdamped (large-γ) regime, when a chemical reaction is forced by a periodic field the reaction rate is determined in part by the geometry of periodic trajectories in the purely deterministic phase space. This work was later extended to cases with different scaling behaviors between the strength of thermal activation and the strength of the external field.[119, 39, 40]

Our goal here is to develop a minimalist theory, applicable at the limit where the magnitude $\sqrt{2\sigma}$ of a noise sequence $\xi_\alpha(t)$ is a small enough perturbation to the periodic driving $E(t)$ that the TS trajectory of the noiseless system (the periodic orbit) gives rise to a DS with minimal recrossings. This deterministic TS trajectory (DTS trajectory) does not solve the equations of motion (118) with a non-zero value of σ. We therefore distinguish the DTS trajectory from the true TS trajectory of the noisy system (that we do not compute in this work).

A principal assumption for the use of the noise-free geometry is that the phase space density of the thermal system, and its time-dependence, is approximately that of the deterministic system, i.e., $p_t(\Delta x_\alpha, \Delta v_\alpha) \approx p_t(\Delta x, \Delta v)$. As shown in Fig. 35, for small values of σ the geometry of the thermal system is similar to that of its deterministic counterpart. The rate theory developed in Sec. 5.4.3 for the deterministic system can therefore be applied. This is advantageous in applications such as in comparisons with experiments in which the

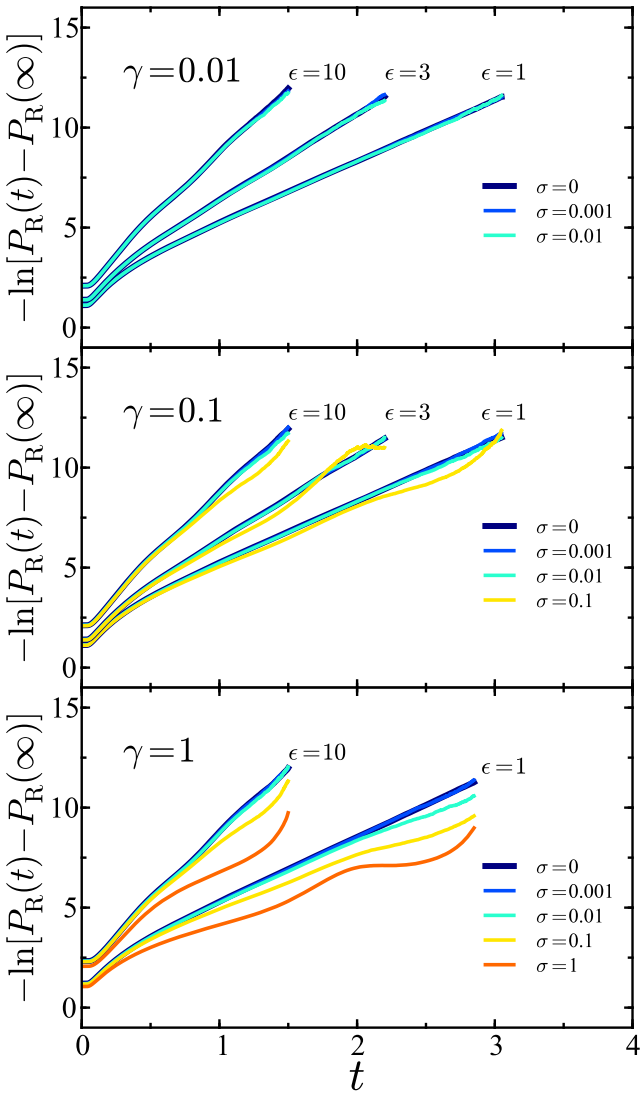

Figure 47: Time dependence of the scaled logarithm of the reactant population for systems with single-frequency ($\mathbf{\Omega}_1$) periodic and thermal driving for $\gamma = 0.01$ (top), $\gamma = 0.1$ (middle), and $\gamma = 1$ (bottom). The color of each line corresponds to a specific σ value. The decay for systems with various anharmonicites $\epsilon \in \{1, 3, 10\}$ are shown and denoted in each panel. The fundamental driving frequency is $\Omega_f = 5$ for all panels. For visual clarity, each curve is truncated at a point where the data became noisy.

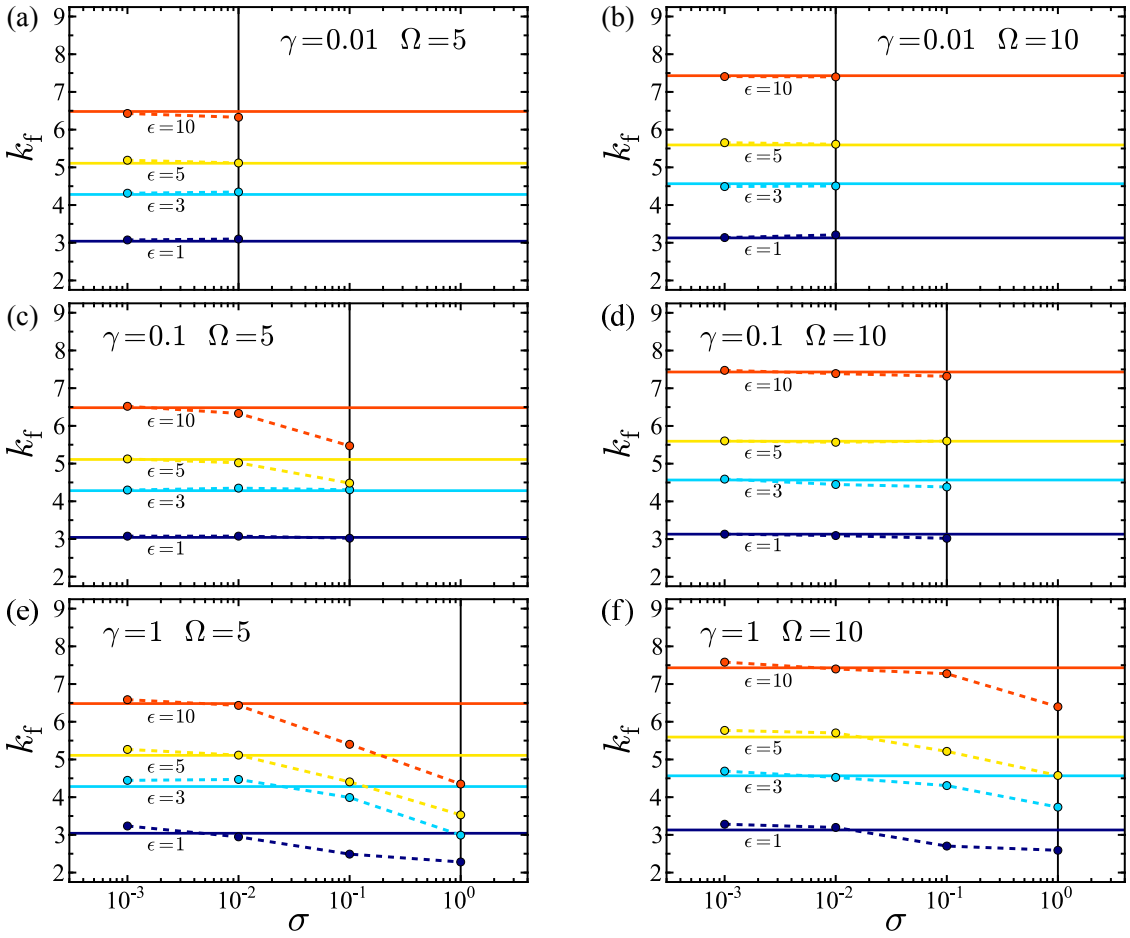

Figure 48: The barrier crossing rates of systems following the equations of motion (118) as a function noise strength σ. The rates calculated using the DS attached to the DTS trajectory for single-frequency ($\mathbf{\Omega}_1$) driving and various values of ϵ, γ, and Ω are shown as circles. The horizontal lines (solid) denote the the rates given by the the Floquet exponents of the corresponding DTS trajectory and are colored according to a respective ϵ value. The black vertical lines (solid) denote the noise strength where the fluctuation-dissipation theorem is obeyed.

exact noise sequence is not known.

Thermal systems in which the fluctuation-dissipation theorem (FDR) is not obeyed due to energy dissipation constitute non-equilibrium processes. Formal treatments of fluctuation-response in periodically forced systems by Teramoto, Harada, and Sasa [67, 179] provide insight into the rate of energy dissipation in such systems. Green *et al.*[62] have shown that the rate of energy dissipation is directly related to the dynamical entropy of the system. To realize non-equilibrium conditions in the present model reaction, the damping constant γ is held constant and the strength of the thermal fluctuations σ is increased up to the point where the FDR is satisfied. If the initial velocities are drawn from a Boltzmann ensemble with $k_{\mathrm{B}}T = 1$ (in dimensionless units), this is the case at $\sigma = \gamma$. If $\sigma < \gamma$ the thermal bath is at a lower temperature than that of the distribution of initial velocities.

The percentage of thermal trajectories that recross the DS attached to the DTS trajectory is shown in Fig. 46 for varying noise strengths σ and constant dissipation rates. As shown in Figs. 46(a) and 46(b), a minimal number of recrossings occur below and up to the FDR threshold for small values of γ. For the $\gamma = 1$ case, shown in Fig. 46(c), trajectories persist around the BT for long times, leading to a larger number of recrossings than observed for smaller dissipation rates. For the overdamped dynamics ($\gamma = 3$), shown in Fig. 46(d), the deterministic DS identifies reactive trajectories adequately only for weak thermal driving (small σ) and strong anharmonicity. As the harmonic limit is approached or in equilibrium systems the superimposed DS becomes very poor.

The decay of the scaled logarithm of the normalized reactant population, as calculated with the superimposed deterministic DS, is shown in Fig. 47 for various parameter values. Over all friction regimes, the population decay of the systems with additional thermal driving follows that of its deterministic counterpart if the noise strength σ is sufficiently low. For $\gamma = 1$, when the strength of the thermal driving approaches that of the FDR, a decrease in the reaction rate is observed. The data presented in Fig. 47 becomes highly oscillatory at long times due to recrossings of the DS. For visual clarity each data series has been truncated to remove this noisy tail.

The thermal rates calculated using the DTS trajectory are shown in Fig. 48. As expected by the minimal number of recrossings shown in Fig. 46, stability analysis of the DTS can produce an excellent approximation to the rate in thermal environments. Through calculation of the error between the numerically calculated rate with included noise and the rate given by the Floquet exponents of the DTS trajectory, the extent of applicability of the noise-free geometry can be quantified. This error is $< 3\%$ at $\gamma = 0.01$ over all parameter values. It is $< 1\%$ for $\epsilon \in \{5, 10\}$. Increasing the dissipation by an order of magnitude ($\gamma = 0.1$) results in the same general trends, with all errors generally less than 5%. The exceptions occur at the noise strength where the FDR is obeyed ($\sigma = 0.1$) at $\epsilon \in \{1, 3\}$ and $\Omega = 5$ for which the error $\approx 20\%$. For $\gamma = 1.0$ and $\Omega = 10$, all calculated errors are less than or on the order of 20%, increasing monotonically as a function of σ. As illustrated in Fig. 48(e), at lower-frequency driving ($\Omega = 5$) and large noise ($\sigma = 1$), the error is between $30\% - 50\%$. This suggests a practical upper bound to the applicability of the noise-free geometry in estimating the reaction rates in the presence of noise. Although not shown, for overdamped dynamics, stability analysis of the DTS gives an accurate approximation to the rate only in non-equilibrium small noise regimes.

The calculated errors are on the order of the error expected from application of variational transition state theory (VTST).[188] The presented methodology is advantageous over VTST as it does not require the integration of large numbers of trajectories or a flux minimization procedure. Thus, stability analysis of the DTS trajectory offers a simple rate calculation methodology that can be readily applied, in weak thermal environments, to driven chemical reactions with only prerequisite knowledge of the geometry of the energy surface and the functional shape of the driving waveform.

5.7 Conclusions

We have shown that in a model chemical reaction subjected to the influence of forcing from a temporally periodic external field, a recrossing-free dividing surface can be constructed over an unstable periodic orbit in the region of a moving energetic barrier top. This no-recrossings surface has been shown to persist for strongly anharmonic barriers subjected to

single-mode, and multi-mode, driving waveforms. A formally exact rate theory has been developed based on the flux of reactive trajectories through this recrossing-free surface, rectifying the principal criterion of transition state theory for periodically driven chemical reactions.

To circumvent computationally taxing numerical calculations of the reactive flux through this surface, a rate theory has been developed based on the stability of the dividing surface. Strong agreement was observed between the rate predicted by the Floquet exponents of a trajectory defining the phase space evolution the dividing surface and rate calculated from simulation of a large ensemble of trajectories. Thus, in a periodically driven chemical reaction the asymptotic decay rate of an initial distribution of reactants can be extracted directly from the stability of the time-varying dividing surface irrespective of the dynamics of the reactive population.

Use of the noise-free geometry to approximate the corresponding structure of a driven thermal system has been shown to give an excellent approximation to the optimal dividing surface if the magnitude of the oscillating force is large compared with that from the thermal environment. For thermally activated processes, the stability exponents of the purely periodically driven system can thus be used to predict the reaction rates without an explicit treatment of the thermal dynamics. The extension of the this work to include an explicit treatment of the noise, including systems with structured solvents environments [31, 30] and systems displaying fluctuating rates [53] are possible next steps, and ones which we are currently pursuing.

CHAPTER VI

CONCLUSIONS

6.1 Structure of a Stochastic Mimic of Soft Particles

In this thesis, we have developed a new model to simulate the dynamics of soft penetrable systems through the use of a stochastic penetration algorithm (SPA). This stochastic algorithm allows the simulation of pseudo-soft matter where particles can overlap despite being governed by potentials that are unbounded at the origin. Molecular dynamics simulations of several SPA systems have been performed using stochastic collision rules. The results of these simulations have been used to measure the occupied volume of systems of overlapping soft particles. While a theoretical prediction of the occupied volume is a fundamental question, the application of theories previously developed for analogous permeable systems fails to give agreement with the simulation results. This has necessitated the derivation of new analytical expressions for the occupied volume fraction for permeable particles satisfying the SPA. We found these to be in excellent agreement with results obtained from dynamical simulations of penetrable homogeneous systems.

A quadrature of the penetrative region of the pair correlation function is found to be of principal importance in predicting the overlapped particle ratios and thus structural knowledge of overlap probabilities is necessary to predict the occupied volume due to the non-negligible contribution of multi-body effects at high densities. In some cases closed form solutions for the structural properties of stochastically penetrable models are known. As such, stochastic potentials could provide a methodological framework to acquire analytic solutions to problems that are otherwise intractable when framed deterministically.

The models developed in this Chapter are analogous to event-driven hard-body algorithms and present a significant computational acceleration when compared to deterministic (time-driven) algorithms. While this acceleration is enticing for computational studies, the advantage of the presented models is not purely of concern for computational science.

Through simplification of the underlying dynamical rules, the stochastic collision models allow probing of the interactions that govern soft matter and provide a route to better understanding of these fundamental properties. The use of stochastic collision models in simulation could be extended to include multiple repulsive regions. Cluster forming crystals have been shown to exhibit exotic phase behavior, including quasi-crystalline structures, when the underlying interactions are governed by potentials with two length scales. Additionally, the presented methods allow probing of soft matter structures at non-zero temperatures and a possible extension of this work would be to study the persistence of structural distributions in the liquid state.

6.2 Effective Surface Coverage of Coarse-Grained Soft Matter

The surface coverage of coarse-grained macromolecules bound to a solid substrate is not simply proportional to the two-dimensional number density because macromolecules can overlap. As a function of the overlap probability δ, we have developed analytical formulas and computational models capable of characterizing this non-linear relationship. The interactions between macromolecules have been modeled using a finite bounded potential which allows multiple macromolecules to occupy the same binding site. The softness of the bounded potential is thereby reduced to the single parameter δ. Through variation of this parameter, completely hard ($\delta = 0$) and completely soft ($\delta = 1$) behavior can be bridged. For soft macromolecular interactions ($\delta > 0$), multiple occupancy reduces the fraction of sites ϕ occupied on the substrate. We have derived the exact transition probability between sequential configurations and use this probability to predict ϕ and the distribution of occupied sites. Due to the complexity of the exact ϕ expressions and their analytical intractability at the thermodynamic limit, we have applied a simplified mean-field (MF) expression for ϕ. The MF model has been shown to be in excellent agreement with the exact result. Both the exact and MF models were applied to an example dynamical system with multi-body interactions governed by a stochastic bounded potential. Both models show agreement with results measured from simulation.

Kinetic analysis and the inclusion of nearest neighbor interactions are possible next

steps of the presented work. The rate of adsorption of soft structures is of importance for applicative purposes, such as the coating of colloidal structures with polymeric motifs. Our current research focuses on these areas through the development of modified Becker-Döring nucleation equations. Additionally, the inclusion of site-site interactions in the presented model could further elucidate the anomalous phase behaviors that are observed in cluster-forming soft matter.

6.3 Transport Properties of Penetrable Rods

The dynamical properties of a system of soft particles governed by stochastic intermolecular interactions have been studied over varying ranges of penetrability and softness. We have measured various dynamical observables from simulation and compared these results to developed theoretical values. We find that while the spatial structures of stochastic soft-matter systems are highly complex, the dynamical properties can adequately approximated using modified hard-core arguments with Enskog corrections. The results presented in this chapter elucidate the transport properties of soft matter with varying stochastic porosity and show that the underlying softness of the governing interactions is directly dictated by the degree of correlation in the particle collision process.

Open questions remain as to the best methodology for mapping the kinetic distributions of coarse-grained structures to the dynamics of the decimated all-atom systems. While it is well-known that coarse-graining can indeed reproduce the spatial distributions of all-atom systems, understanding the dynamical mapping of coarse-graining has been elusive. A derivation of the mapping operator that reproduces the all-atom Hamiltonian dynamics in the coarse-grained space would almost certainly be celebrated, having large implications for computational science as well as for our understanding of the hierarchy of length scales when moving from the microscopic to the macroscopic. Extending the model developed in this Chapter to higher dimensionalities (disks, spheres) provides another possible path forward. Our preliminary results show that the expressions derived in this Chapter can easily be scaled with dimensionality. A rigorous comparison with simulation results could provide insight into the dynamical properties of coarse-grained systems in dimensionalities

of more realistic interest.

6.4 Chemical Reactions Induced by Oscillating External Fields

We have studied the dynamics of a reactant particle surmounting an oscillating energy barrier. A dividing surface attached to a bounded transition state (TS) trajectory has been constructed that is rigorously free from recrossing, even when the dynamics is strongly anharmonic, strongly dissipative, or strongly driven. In addition, whether a trajectory is reactive or not is determined by its location relative to the stable manifold of the TS trajectory. The knowledge of the stable manifold therefore allows prediction of the fate (reactive or nonreactive) of any trajectory, without having to carry out a simulation. The validity of these results has been confirmed by a numerical simulation of ensembles of trajectories. The construction of this dividing surface allows for a formally exact transition state theory rate calculations in periodically driven chemical reactions. Additionally, the rates calculated from numerical simulation and rates predicted by the Floquet exponents of the TS trajectory are in excellent agreement. This result opens the possibility that when chemical reactions are forced by periodic external fields in weak thermal environments the reaction rates can be extracted from knowledge of the stability of governing invariant objects.

The question of how to control selectivity and reactivity in chemical reactions is of principal importance in a myriad of applicative areas. This Chapter provides qualitative evidence that optimal control can be achieved through forcing from tailored external fields. Biasing reaction pathways toward targeted structures can be achieved through field-induced deformation of the manifolds that dictate the rate of a reaction and also the reaction mechanism. Further work with optimization procedures, such as genetic algorithms, could be performed to elucidate the functional driving forms that lead to predefined reaction products. The results of field-assisted synthesis could open mechanistic routes to previously energetically-forbidden organic structures.

REFERENCES

[1] Agarwal, V. and Peters, B., "Nucleation near the eutectic point in a Potts-lattice gas model," *J. Chem. Phys.*, vol. 140, no. 8, p. 084111, 2014.

[2] Allahem, A. and Bartsch, T., "Chaotic dynamics in multidimensional transition states," *J. Chem. Phys.*, vol. 137, no. 21, p. 214310, 2012.

[3] Allen, M. P. and Tildesley, D. J., *Computer Simulations of Liquids*. New York: Oxford, 1987.

[4] Archer, A. J., Rucklidge, A. M., and Knobloch, E., "Quasicrystalline order and a crystal-liquid state in a soft-core fluid," *Phys. Rev. Lett.*, vol. 111, p. 165501, 2013.

[5] Ballauff, M. and Likos, C. N., "Dendrimers in solution: Insight from theory and simulation," *Angew. Chem., Ind. Ed.*, vol. 43, no. 23, pp. 2998–3020, 2004.

[6] Balzani, V., Credi, A., and Venturi, M., "Molecular devices and machines," *NanoToday*, vol. 2, no. 2, pp. 18–25, 2007.

[7] Barkai, E. and Fleurov, V., "Stochastic one-dimensional Lorentz gas on a lattice," *J. Stat. Phys.*, vol. 96, no. 1, pp. 325–359, 1999.

[8] Barkai, E., Fleurov, V., and Klafter, J., "One-dimensional stochastic Lévy-Lorentz gas," *Phys. Rev. E*, vol. 61, pp. 1164–1169, Feb 2000.

[9] Barkan, K., Engel, M., and Lifshitz, R., "Controlled self-assembly of periodic and aperiodic cluster crystals," *Phys. Rev. Lett.*, vol. 113, p. 098304, 2014.

[10] Bartsch, T., Hernandez, R., and Uzer, T., "Transition state in a noisy environment," *Phys. Rev. Lett.*, vol. 95, pp. 058301–01–04, 2005.

[11] Bartsch, T., Revuelta, F., Benito, R. M., and Borondo, F., "Reaction rate calculation with time-dependent invariant manifolds," *J. Chem. Phys.*, vol. 136, no. 22, p. 224510, 2012.

[12] Bartsch, T., Uzer, T., Moix, J. M., and Hernandez, R., "Identifying reactive trajectories using a moving transition state," *J. Chem. Phys.*, vol. 124, pp. 244310(01)–244310(13), 2006.

[13] Bartsch, T., Uzer, T., and Hernandez, R., "Stochastic transition states: Reaction geometry amidst noise," *J. Chem. Phys.*, vol. 123, p. 204102, 2005.

[14] Bishop, M. and Berne, B., "Molecular dynamics of one-dimensional hard rods," *J. Chem. Phys.*, vol. 60, pp. 893–897, 1974.

[15] Blum, L. and Stell, G., "Polydisperse systems. I. Scattering function for polydisperse fluids of hard or permeable spheres," *J. Chem. Phys.*, vol. 71, pp. 42–46, 1979.

[16] Boland, R. P., Galla, T., and McKane, A. J., "Limit cycles, complex Floquet multipliers, and intrinsic noise," *Phys. Rev. E*, vol. 79, p. 051131, 2009.

[17] Brodatzki, U. and Mecke, K., "Simulating stochastic geometries: morphology of overlapping grains," *Comp. Phys. Comm.*, vol. 147, no. 1, pp. 218–221, 2002.

[18] Browne, W. R. and Feringa, B. L., "Making molecular machines work," *Nature Nanotech.*, vol. 1, no. 1, pp. 25–35, 2006.

[19] Brunauer, S., Emmett, P. H., and Teller, E., "Adsorption of gases in multimolecular layers," *J. Am. Chem. Soc.*, vol. 60, no. 2, pp. 309–319, 1938.

[20] Chandler, D., Weeks, J., and Andersen, H., "Van der waals picture of liquids, solids, and phase transformations," *Science*, vol. 220, no. 4599, pp. 787–794, 1983.

[21] Chiew, Y. and Glandt, E., "Interfacial surface area in dispersions and porous media," *J. Colloid Interface Sci.*, vol. 99, no. 1, pp. 86–96, 1984.

[22] Choudhury, N. and Ghosh, S., "Integral equation theory of penetrable sphere fluids: A modified verlet bridge function approach," *J. Chem. Phys.*, vol. 119, no. 9, pp. 4827–4832, 2003.

[23] Cieśla, M., "Continuum random sequential adsorption of polymer on a flat and homogeneous surface," *Phys. Rev. E*, vol. 87, p. 052401, 2013.

[24] Cieśla, M., "Random sequential adsorption of tetramers," *J. Stat. Mech.*, vol. 2013, no. 07, p. P07011, 2013.

[25] Corrales, M., González-Vázquez, J., Balerdi, G., Solá, I., de Nalda, R., and Bañares, L., "Control of ultrafast molecular photodissociation by laser-field-induced potentials," *Nature Chem.*, vol. 6, no. 9, pp. 785–790, 2014.

[26] Coskun, A., Banaszak, M., Astumian, R. D., Stoddart, J. F., and Grzybowski, B. A., "Great expectations: can artificial molecular machines deliver on their promise?," *Chem. Soc. Rev.*, vol. 41, pp. 19–30, 2012.

[27] Coslovich, D. and Ikeda, A., "Cluster and reentrant anomalies of nearly Gaussian core particles," *Soft Matter*, vol. 9, pp. 6786–6795, 2013.

[28] Craven, G. T., Bartsch, T., and Hernandez, R., "Communication: Transition state trajectory stability determines barrier crossing rates in chemical reactions induced by time-dependent oscillating fields," *J. Chem. Phys.*, vol. 141, p. 041106, 2014.

[29] Craven, G. T., Bartsch, T., and Hernandez, R., "Persistence of transition state structure in chemical reactions driven by fields oscillating in time," *Phys. Rev. E*, vol. 89, p. 040801(R), 2014.

[30] Craven, G. T., Popov, A. V., and Hernandez, R., "Structure of a tractable stochastic mimic of soft particles," *Soft Matter*, vol. 10, pp. 5350–5361, 2014.

[31] Craven, G. T., Popov, A. V., and Hernandez, R., "Stochastic dynamics of penetrable rods in one dimension: Occupied volume and spatial order," *J. Chem. Phys.*, vol. 138, p. 244901, 2013.

[32] Craven, G. T., Popov, A. V., and Hernandez, R., "Effective surface coverage of coarse-grained soft matter," *J. Phys. Chem. B*, vol. XX, p. XXXX, 2014. published online, doi:10.1021/jp505207h.

[33] Cvitanović, P., Artuso, R., Mainieri, R., Tanner, G., and Vattay, G., *Chaos: Classical and Quantum*. Niels Bohr Institute, Copenhagen: ChaosBook.org, 2012.

[34] Dama, J. F., Sinitskiy, A. V., McCullagh, M., Weare, J., Roux, B., Dinner, A. R., and Voth, G. A., "The theory of ultra-coarse-graining. 1. general principles," *J. Chem. Theory Comput.*, vol. 9, no. 5, pp. 2466–2480, 2013.

[35] De Leon, N., Mehta, M. A., and Topper, R. Q., "Cylindrical manifolds in phase space as mediators of chemical reaction dynamics and kinetics. I. Theory," *J. Chem. Phys.*, vol. 94, pp. 8310–8328, June 1991.

[36] Dorfman, J., Ernst, M., and Jacobs, D., "Dynamical chaos in the Lorentz lattice gas," *J. Stat. Phys.*, vol. 81, no. 1, pp. 497–513, 1995.

[37] Dotera, T., Oshiro, T., and Ziherl, P., "Mosaic two-lengthscale quasicrystals," *Nature*, vol. 506, no. 7487, pp. 208–211, 2014.

[38] Duff, N. and Peters, B., "Nucleation in a potts lattice gas model of crystallization from solution," *J. Chem. Phys.*, vol. 131, no. 18, p. 184101, 2009.

[39] Dykman, M. I., Golding, B., and Ryvkine, D., "Critical exponent crossovers in escape near a bifurcation point," *Phys. Rev. Lett.*, vol. 92, p. 080602, 2004.

[40] Dykman, M. I. and Ryvkine, D., "Activated escape of periodically modulated systems," *Phys. Rev. Lett.*, vol. 94, p. 070602, Feb 2005.

[41] Elsner, A., Wagner, A., Aste, T., Hermann, H., and Stoyan, D., "Specific surface area and volume fraction of the cherry-pit model with packed pits," *J. Phys. Chem. B*, vol. 113, no. 22, pp. 7780–7784, 2009.

[42] Elsner, N., Royall, C. P., Vincent, B., and Snoswell, D. R. E., "Simple models for two-dimensional tunable colloidal crystals in rotating ac electric fields," *J. Chem. Phys.*, vol. 130, no. 15, p. 154901, 2009.

[43] Ernst, M. and Binder, P., "Lorentz lattice gases: Basic theory," *J. Stat. Phys.*, vol. 51, no. 5, pp. 981–990, 1988.

[44] Ezra, G. S., Waalkens, H., and Wiggins, S., "Microcanonical rates, gap times, and phase space dividing surfaces," *J. Chem. Phys.*, vol. 130, no. 16, p. 164118, 2009.

[45] Ezra, G. S. and Wiggins, S., "Phase-space geometry and reaction dynamics near index 2 saddles," *J. Phys. A: Math. Theor.*, vol. 42, p. 205101, 2009.

[46] Fantoni, R., Giacometti, A., Malijevskỳ, A., and Santos, A., "Penetrable-square-well fluids: Analytical study and Monte Carlo simulations," *J. Chem. Phys.*, vol. 131, no. 12, p. 124106, 2009.

[47] Fantoni, R., Malijevsk, A., Santos, A., and Giacometti, A., "The penetrable square-well model: Extensive versus non-extensive phases," *Mol. Phys.*, vol. 109, no. 23-24, pp. 2723–2736, 2011.

[48] Feder, J., "Random sequential adsorption," *J. Theor. Biol.*, vol. 87, no. 2, pp. 237 – 254, 1980.

[49] Feringa, B. L., "Nanotechnology: In control of molecular motion," *Nature*, vol. 408, no. 6809, pp. 151–154, 2000.

[50] Fernaud, M.-J., Lomba, E., and Lee, L. L., "A self-consistent integral equation study of the structure and thermodynamics of the penetrable sphere fluid," *J. Chem. Phys.*, vol. 112, no. 2, pp. 810–816, 2000.

[51] Finken, R., Hansen, J.-P., and Louis, A. A., "Phase separation of a multiple occupancy lattice gas," *J. Phys. A*, vol. 37, no. 3, p. 577, 2004.

[52] Fletcher, S. P., Dumur, F., Pollard, M. M., and Feringa, B. L., "A reversible, unidirectional molecular rotary motor driven by chemical energy," *Science*, vol. 310, no. 5745, pp. 80–82, 2005.

[53] Flynn, S. W., Zhao, H. C., and Green, J. R., "Measuring disorder in irreversible decay processes," *J. Chem. Phys.*, vol. 141, no. 10, p. 104107, 2014.

[54] Frenkel, D. and Smit, B., *Understanding Molecular Simulation: From Algorithms to Application*. NY: Academic Press, 1996.

[55] Garcia-Garibay, M. A., "Crystalline molecular machines: Encoding supramolecular dynamics into molecular structure," *Proc. Natl. Acad. Sci. U.S.A.*, vol. 102, no. 31, pp. 10771–10776, 2005.

[56] Gaspard, P., *Chaos, scattering and statistical mechanics*, vol. 9. Cambridge University Press, 1998.

[57] Georgiadis, C., Moultos, O., Gergidis, L. N., and Vlahos, C., "Brownian dynamics simulations on the self-assembly behavior of ab hybrid dendriticstar copolymers," *Langmuir*, vol. 27, no. 2, pp. 835–842, 2011.

[58] Glotzer, S. C., "Some assembly required," *Science*, vol. 306, no. 5695, p. 419, 2004.

[59] Glotzer, S. C. and Solomon, M. J., "Anisotropy of building blocks and their assembly into complex structures," *Nature Mater.*, vol. 6, no. 8, pp. 557–562, 2007.

[60] Gotoh, K., Nakagawa, M., Furuuchi, M., and Yoshigi, A., "Pore size distributions in random assemblies of equal spheres," *J. Chem. Phys.*, vol. 85, pp. 3078–3080, 1986.

[61] Graf, H. and Löwen, H., "Density jumps across phase transitions in soft-matter systems," *Phys. Rev. E*, vol. 57, no. 5, pp. 5744–5753, 1998.

[62] Green, J. R., Costa, A. B., Grzybowski, B. A., and Szleifer, I., "Relationship between dynamical entropy and energy dissipation far from thermodynamic equilibrium," *Proc. Natl. Acad. Sci. U.S.A.*, vol. 110, no. 41, pp. 16339–16343, 2013.

[63] Green, J. R., Hofer, T. S., Berry, R. S., and Wales, D. J., "Characterizing molecular motion in H_2O and H_3O+ with dynamical instability statistics," *J. Chem. Phys.*, vol. 135, no. 18, p. 184307, 2011.

[64] Grünwald, M. and Geissler, P. L., "Patterns without patches: Hierarchical self-assembly of complex structures from simple building blocks," *ACS Nano*, vol. 8, no. 6, pp. 5891–5897, 2014.

[65] Hagy, M. C. and Hernandez, R., "Dynamical simulation of electrostatic striped colloidal particles," *J. Chem. Phys.*, vol. 140, p. 034701, 2014.

[66] Hagy, M. C. and Hernandez, R., "Dynamical simulation of dipolar Janus colloids: Equilibrium structure and thermodynamics," *J. Chem. Phys.*, vol. 137, p. 044505, 2012.

[67] Harada, T. and Sasa, S., "Equality connecting energy dissipation with a violation of the fluctuation-response relation," *Phys. Rev. Lett.*, vol. 95, p. 130602, 2005.

[68] Hardy, G. H. and Ramanujan, S., "Asymptotic formulaæ in combinatory analysis," *Proc. London Math. Soc.*, vol. 2, no. 1, pp. 75–115, 1918.

[69] Haus, J. and Raveché, H., "Computer studies of dynamics in one dimension: Hard rods," *J. Chem. Phys.*, vol. 68, pp. 4969–4976, 1978.

[70] Hernandez, R. and Popov, A., "Molecular dynamics out of equilibrium: Mechanics and measurables," *WIREs Comput. Mol. Sci,*, vol. XX, p. XXXX, 2014. doi:10.1002/wcms.1190.

[71] Hernandez, R., "A combined use of perturbation theory and diagonalization: Application to bound energy levels and semiclassical rate theory," *J. Chem. Phys.*, vol. 101, pp. 9534–9547, 1994.

[72] Hernandez, R., Bartsch, T., and Uzer, T., "Transition state theory in liquids beyond planar dividing surfaces," *Chem. Phys.*, vol. 370, pp. 270–276, 2010.

[73] Hernandez, R. and Miller, W. H., "Semiclassical transition state theory. A new perspective," *Chem. Phys. Lett.*, vol. 214, pp. 129–136, 1993.

[74] Hoover, W. G. and Ree, F. H., "Melting transition and communal entropy for hard spheres," *J. Chem. Phys.*, vol. 49, no. 8, pp. 3609–3617, 1968.

[75] Horinek, D. and Michl, J., "Surface-mounted altitudinal molecular rotors in alternating electric field: Single-molecule parametric oscillator molecular dynamics," *Proc. Natl. Acad. Sci. U.S.A.*, vol. 102, no. 40, pp. 14175–14180, 2005.

[76] Hynes, J. T., "Chemical reaction dynamics in solution," *Annu. Rev. Phys. Chem.*, vol. 36, pp. 573–597, 1985.

[77] Iñarrea, M., Palacián, J. F., Pascual, A. I., and Salas, J. P., "Bifurcations of dividing surfaces in chemical reactions," *J. Chem. Phys.*, vol. 135, no. 1, p. 014110, 2011.

[78] Çiftçi, U. and Waalkens, H., "Reaction dynamics through kinetic transition states," *Phys. Rev. Lett.*, vol. 110, p. 233201, 2013.

[79] Ikeda, A. and Miyazaki, K., "Glass transition of the monodisperse Gaussian core model," *Phys. Rev. Lett.*, vol. 106, no. 1, p. 015701, 2011.

[80] Jäger, S. and Klapp, S. H. L., "Pattern formation of dipolar colloids in rotating fields: layering and synchronization," *Soft Matter*, vol. 7, p. 6606, 2011.

[81] Jaster, A., "The hexatic phase of the two-dimensional hard disk system," *Phys. Lett. A*, vol. 330, no. 12, pp. 120 – 125, 2004.

[82] Jepsen, D., "Dynamics of a simple many-body system of hard rods," *Journal of Mathematical Physics*, vol. 6, p. 405, 1965.

[83] Jin, X., Wang, N. H. L., Tarjus, G., and Talbot, J., "Irreversible adsorption on nonuniform surfaces: The random site model," *J. Phys. Chem.*, vol. 97, no. 17, pp. 4256–4258, 1993.

[84] Kadanoff, L. P. and Tang, C., "Escape from strange repellers," *Proc. Natl. Acad. Sci. U.S.A.*, vol. 81, no. 4, pp. 1276–1279, 1984.

[85] Kasperkovitz, P. and Reisenberger, J., "Finite hard rod systems and their thermodynamic limit. iii. collision frequency, no-collision probability, and velocity autocorrelation function," *Journal of mathematical Physics*, vol. 26, p. 2617, 1985.

[86] Kawai, S., Bandrauk, A. D., Jaffé, C., Bartsch, T., Palacián, J., and Uzer, T., "Transition state theory for laser-driven reactions," *J. Chem. Phys.*, vol. 126, p. 164306, Apr. 2007.

[87] Kawai, S. and Komatsuzaki, T., "Quantum reaction boundary to mediate reactions in laser fields," *J. Chem. Phys.*, vol. 134, no. 2, p. 024317, 2011.

[88] Kay, E. R., Leigh, D. A., and Zerbetto, F., "Synthetic molecular motors and mechanical machines," *Angew. Chem., Ind. Ed.*, vol. 46, no. 1-2, pp. 72–191, 2007.

[89] Khuong, T.-A. V., Zepeda, G., Ruiz, R., Khan, S. I., and Garcia-Garibay, M. A., "Molecular compasses and gyroscopes: engineering molecular crystals with fast internal rotation," *Cryst. Growth Des.*, vol. 4, no. 1, pp. 15–18, 2004.

[90] Kim, S. and Suh, S., "Inhomogeneous structure of penetrable spheres with bounded interactions," *J. Chem. Phys.*, vol. 117, no. 21, pp. 9880–9886, 2002.

[91] Kindt, J. T., "Accounting for finite-number effects on cluster size distributions in simulations of equilibrium aggregation," *J. Chem. Theory Comput.*, vol. 9, no. 1, pp. 147–152, 2013.

[92] Kirkwood, J., "Statistical mechanics of fluid mixtures," *J. Chem. Phys.*, vol. 3, pp. 300–313, 1935.

[93] Klok, M., Boyle, N., Pryce, M. T., Meetsma, A., Browne, W. R., and Feringa, B. L., "Mhz unidirectional rotation of molecular rotary motors," *J. Am. Chem. Soc.*, vol. 130, no. 32, pp. 10484–10485, 2008.

[94] Koumakis, N., Pamvouxoglou, A., Poulos, A. S., and Petekidis, G., "Direct comparison of the rheology of model hard and soft particle glasses," *Soft Matter*, vol. 8, pp. 4271–4284, 2012.

[95] Krekelberg, W. P., Kumar, T., Mittal, J., Errington, J., and Truskett, T. M., "Anomalous structure and dynamics of the Gaussian-core fluid," *Phys. Rev. E*, vol. 79, no. 3, p. 031203, 2009.

[96] Krekelberg, W. P., Mittal, J., Ganesan, V., and Truskett, T. M., "How short-range attractions impact the structural order, self-diffusivity, and viscosity of a fluid," *J. Chem. Phys.*, vol. 127, no. 4, p. 044502, 2007.

[97] Kromer, J. A., Schmiedeberg, M., Roth, J., and Stark, H., "What phasons look like: Particle trajectories in a quasicrystalline potential," *Phys. Rev. Lett.*, vol. 108, p. 218301, 2012.

[98] Langmuir, I., "The constitution and fundamental properties of solids and liquids. Part I. Solids.," *J. Am. Chem. Soc.*, vol. 38, no. 11, pp. 2221–2295, 1916.

[99] Lebowitz, J. and Percus, J., "Kinetic equations and density expansions: Exactly solvable one-dimensional system," *Physical Review*, vol. 155, no. 1, p. 122, 1967.

[100] Lebowitz, J., Percus, J., and Sykes, J., "Time evolution of the total distribution function of a one-dimensional system of hard rods," *Physical Review*, vol. 171, no. 1, p. 224, 1968.

[101] Lebowitz, J. and Sykes, J., "The velocity autocorrelation function of a finite model system," *J. Stat. Phys.*, vol. 6, no. 2, pp. 157–171, 1972.

[102] Lee, S. and Torquato, S., "Porosity for the penetrable-concentric-shell model of two-phase disordered media: Computer simulation results," *J. Chem. Phys.*, vol. 89, pp. 3258–3263, 1988.

[103] Lehmann, J., Reimann, P., and Hänggi, P., "Activated escape over oscillating barriers: The case of many dimensions," *Phys. Status Solidi B*, vol. 237, pp. 53–71, Apr. 2003.

[104] Lehmann, J., Reimann, P., and Hänggi, P., "Surmounting oscillating barriers," *Phys. Rev. Lett.*, vol. 84, pp. 1639–1642, Feb. 2000.

[105] Lehmann, J., Reimann, P., and Hänggi, P., "Surmounting oscillating barriers: Path-integral approach for weak noise," *Phys. Rev. E*, vol. 62, pp. 6282–6303, Nov. 2000.

[106] Leigh, D. A., Wong, J. K., Dehez, F., and Zerbetto, F., "Unidirectional rotation in a mechanically interlocked molecular rotor," *Nature*, vol. 424, no. 6945, pp. 174–179, 2003.

[107] Li, C., Shoujiguchi, A., Toda, M., and Komatsuzaki, T., "Definability of no-return transition states in the high-energy regime above the reaction threshold," *Phys. Rev. Lett.*, vol. 97, p. 028302, 2006.

[108] Li, H., Qian, C.-J., Wang, C., and Luo, M.-B., "Critical adsorption of a flexible polymer confined between two parallel interacting surfaces," *Phys. Rev. E*, vol. 87, p. 012602, 2013.

[109] Lidström, P., Tierney, J., Wathey, B., and Westman, J., "Microwave assisted organic synthesis–a review," *Tetrahedron*, vol. 57, no. 45, pp. 9225 – 9283, 2001.

[110] Likos, C. N., Rosenfeldt, S., Dingenouts, N., Ballauff, M., Lindner, P., Werner, N., and Vogtle, F., "Gaussian effective interaction between flexible dendrimers of fourth generation: A theoretical and experimental study," *J. Chem. Phys.*, vol. 117, no. 4, pp. 1869–1877, 2002.

[111] Likos, C. N., "Effective interactions in soft condensed matter physics," *Phys. Rep.*, vol. 348, no. 4 - 5, pp. 267 – 439, 2001.

[112] Likos, C. N., "Soft matter with soft particles," *Soft Matter*, vol. 2, pp. 478–498, 2006.

[113] Likos, C., Watzlawek, M., and Löwen, H., "Freezing and clustering transitions for penetrable spheres," *Phys. Rev. E*, vol. 58, no. 3, pp. 3135–3144, 1998.

[114] Lin, C.-C. and Anseth, K. S., "Cell-cell communication mimicry with poly(ethylene glycol) hydrogels for enhancing β-cell function," *Proc. Natl. Acad. Sci. U.S.A.*, vol. 108, no. 16, pp. 6380–6385, 2011.

[115] Loget, G. and Kuhn, A., "Electric field-induced chemical locomotion of conducting objects," *Nat. Commun.*, vol. 2, p. 535, 2011.

[116] Lyubimov, I. and Guenza, M. G., "First-principle approach to rescale the dynamics of simulated coarse-grained macromolecular liquids," *Phys. Rev. E*, vol. 84, no. 3, p. 031801, 2011.

[117] Ma, F., Wu, D. T., and Wu, N., "Formation of colloidal molecules induced by alternating-current electric fields," *J. Am. Chem. Soc.*, vol. 135, no. 21, pp. 7839–7842, 2013.

[118] MacKay, R. S. and Strub, D. C., "Bifurcations of transition states: Morse bifurcations," *Nonlinearity*, vol. 27, no. 5, p. 859, 2014.

[119] Maier, R. S. and Stein, D. L., "Noise-activated escape from a sloshing potential well," *Phys. Rev. Lett.*, vol. 86, pp. 3942–3945, 2001.

[120] Mak, C. H., "Large-scale simulations of the two-dimensional melting of hard disks," *Phys. Rev. E*, vol. 73, p. 065104, 2006.

[121] Malescio, G., "Phase stability of the penetrable-square-well model: an integral equation approach," *Mol. Phys.*, p. doi:10.1080/00268976.2013.860246, 2013.

[122] Malijevskỳ, A., Yuste, S., and Santos, A., "Low-temperature and high-temperature approximations for penetrable-sphere fluids: Comparison with Monte Carlo simulations and integral equation theories," *Phys. Rev. E*, vol. 76, no. 2, p. 021504, 2007.

[123] Malijevsky, A. and Santos, A., "Structure of penetrable-rod fluids: Exact properties and comparison between Monte Carlo simulations and two analytic theories," *J. Chem. Phys.*, vol. 124, no. 7, p. 074508, 2006.

[124] Marquest, C. and Witten, T., "Simple cubic structure in copolymer mesophases," *Journal de Physique*, vol. 50, no. 10, pp. 1267–1277, 1989.

[125] Marrink, S. J., Risselada, H. J., Yefimov, S., Tieleman, D. P., and de Vries, A. H., "The martini force field: coarse grained model for biomolecular simulations," *J. Phys. Chem. B*, vol. 111, no. 27, pp. 7812–7824, 2007.

[126] Masel, R. I., *Principles of Adsorption and Reaction on Solid Surfaces*. New York: John Wiley & Sons, 1996.

[127] Mattsson, J., Wyss, H. M., Fernandez-Nieves, A., Miyazaki, K., Hu, Z., Reichman, D. R., and Weitz, D. A., "Soft colloids make strong glasses," *Nature*, vol. 462, no. 7269, pp. 83–86, 2009.

[128] Meng, H. and Li, G., "Reversible switching transitions of stimuli-responsive shape changing polymers," *J. Mater. Chem. A*, vol. 1, pp. 7838–7865, 2013.

[129] Metropolis, N., Rosenbluth, A. W., Rosenbluth, M. N., Teller, A. H., and Teller, E., "Equation of state calculations by fast computing machines," *J. Chem. Phys.*, vol. 21, no. 6, pp. 1087–1092, 1953.

[130] Michl, J. and Sykes, E. C. H., "Molecular rotors and motors: Recent advances and future challenges," *ACS Nano*, vol. 3, no. 5, pp. 1042–1048, 2009.

[131] Milchev, A., Egorov, S. A., and Binder, K., "Critical adsorption of a single macromolecule in polymer brushes," *Soft Matter*, pp. –, 2014.

[132] Miller, J. B., Usselman, A. C. P., Anthony, R. J., Kortshagen, U. R., Wagner, A. J., Denton, A. R., and Hobbie, E. K., "Phase separation and the 'coffee-ring' effect in polymer-nanocrystal mixtures," *Soft Matter*, vol. 10, pp. 1665–1675, 2014.

[133] Miller, W. H., "Beyond transition-state theory: A rigorous quantum theory of chemical reaction rates," *Acc. Chem. Res.*, vol. 26, p. 174, 1993.

[134] Mladek, B. M., Charbonneau, P., Likos, C. N., Frenkel, D., and Kahl, G., "Multiple occupancy crystals formed by purely repulsive soft particles," *J. Phys.: Condens. Matter*, vol. 20, no. 49, p. 494245, 2008.

[135] Mladek, B. M., Gottwald, D., Kahl, G., Neumann, M., and Likos, C. N., "Formation of polymorphic cluster phases for a class of models of purely repulsive soft spheres," *Phys. Rev. Lett.*, vol. 96, p. 045701, 2006.

[136] Mladek, B. M., Kahl, G., and Neumann, M., "Thermodynamically self-consistent liquid state theories for systems with bounded potentials," *J. Chem. Phys.*, vol. 124, no. 6, p. 064503, 2006.

[137] Mladek, B., Fernaud, M., Kahl, G., and Neumann, M., "On the thermodynamic properties of the generalized Gaussian core model," *Condens. Matter Phys.*, vol. 8, no. 1, pp. 135–148, 2005.

[138] Mullen, R. G., Shea, J.-E., and Peters, B., "Communication: An existence test for dividing surfaces without recrossing," *J. Chem. Phys.*, vol. 140, no. 4, p. 041104, 2014.

[139] Mullen, R. G., Shea, J.-E., and Peters, B., "Transmission coefficients, committors, and solvent coordinates in ion-pair dissociation," *J. Chem. Theory Comput.*, vol. 10, no. 2, pp. 659–667, 2014.

[140] Naess, A. and Moe, V., "Efficient path integration methods for nonlinear dynamic systems," *Probab. Eng. Mech.*, vol. 15, no. 2, pp. 221 – 231, 2000.

[141] Ni, R., Cohen Stuart, M. A., Dijkstra, M., and Bolhuis, P. G., "Crystallizing hard-sphere glasses by doping with active particles," *Soft Matter*, vol. 10, pp. 6609–6613, 2014.

[142] Noid, W. G., "Perspective: Coarse-grained models for biomolecular systems," *J. Chem. Phys.*, vol. 139, no. 9, p. 090901, 2013.

[143] Noya, E. G., Vega, C., and de Miguel, E., "Determination of the melting point of hard spheres from direct coexistence simulation methods," *J. Chem. Phys.*, vol. 128, no. 15, p. 154507, 2008.

[144] Orel, A. E. and Miller, W. H., "Collision induced absorption spectra for gas phase chemical reactions in a high power IR laser field," *J. Chem. Phys.*, vol. 72, no. 9, pp. 5139–5144, 1980.

[145] Pamies, J. C., Cacciuto, A., and Frenkel, D., "Phase diagram of Hertzian spheres," *J. Chem. Phys.*, vol. 131, no. 4, p. 044514, 2009.

[146] Pechukas, P. and Pollak, E., "Classical transition state theory is exact if the transition state is unique," *J. Chem. Phys.*, vol. 71, p. 2062, 1979.

[147] Platkov, M. and Gruebele, M., "Periodic and stochastic thermal modulation of protein folding kinetics," *J. Chem. Phys.*, vol. 141, no. 3, p. 035103, 2014.

[148] Pollak, E., "Variational transition state theory for activated rate processes," *J. Chem. Phys.*, vol. 93, pp. 1116–1124, 1990.

[149] Pollak, E., Child, M. S., and Pechukas, P., "Classical transition state theory: A lower bound to the reaction probability," *J. Chem. Phys.*, vol. 72, p. 1669, 1980.

[150] Pollak, E. and Pechukas, P., "Transition states, trapped trajectories, and classical bound states embedded in the continuum," *J. Chem. Phys.*, vol. 69, p. 1218, 1978.

[151] Pollak, E. and Pechukas, P., "Unified statistical model for "complex" and "direct" reaction mechanisms: A test on the collinear $H + H_2$ exchange reaction," *J. Chem. Phys.*, vol. 70, pp. 325–333, Jan. 1979.

[152] Pollak, E. and Talkner, P., "Reaction rate theory: What it was, where it is today, and where is it going?," *Chaos*, vol. 15, pp. 026116–1–11, 2005.

[153] Poon, G. G. and Peters, B., "A stochastic model for nucleation in the boundary layer during solvent freeze-concentration," *Cryst. Growth Des.*, vol. 13, no. 11, pp. 4642–4647, 2013.

[154] Popov, A. V., Melvin, J., and Hernandez, R., "Dynamics of swelling hard spheres surmised by an irreversible Langevin equation," *J. Phys. Chem. A*, vol. 110, pp. 1635–1644, 2006.

[155] Pötschke, D., Ballauff, M., Lindner, P., Fischer, M., and Vögtle, F., "The structure of dendritic molecules in solution as investigated by small-angle neutron scattering," *Macromol. Chem. Phys.*, vol. 201, no. 3, pp. 330–339, 2000.

[156] Prokop, A., Vacek, J., and Michl, J., "Friction in carborane-based molecular rotors driven by gas flow or electric field: Classical molecular dynamics," *ACS Nano*, vol. 6, no. 3, pp. 1901–1914, 2012.

[157] Quintanilla, J. and Torquato, S., "Clustering properties of d-dimensional overlapping spheres," *Phys. Rev. E*, vol. 54, no. 5, pp. 5331–5339, 1996.

[158] Quintanilla, J. and Torquato, S., "Lineal measures of clustering in overlapping particle systems," *Phys. Rev. E*, vol. 54, no. 4, pp. 4027–4036, 1996.

[159] Revuelta, F., Bartsch, T., Benito, R. M., and Borondo, F., "Communication: Transition state theory for dissipative systems without a dividing surface," *J. Chem. Phys.*, vol. 136, no. 9, p. 091102, 2012.

[160] Rikvold, P. and Stell, G., "d-dimensional interpenetrable-sphere models of random two-phase media: Microstructure and an application to chromatography," *J. Colloid Interface Sci.*, vol. 108, no. 1, pp. 158–173, 1985.

[161] Rikvold, P. and Stell, G., "Porosity and specific surface for interpenetrable-sphere models of two-phase random media," *J. Chem. Phys.*, vol. 82, no. 2, pp. 1014–1020, 1985.

[162] Rottgermann, P. J. F., Alberola, A. P., and Radler, J. O., "Cellular self-organization on micro-structured surfaces," *Soft Matter*, pp. –, 2014.

[163] Saha, S. and Stoddart, J. F., "Photo-driven molecular devices," *Chem. Soc. Rev.*, vol. 36, pp. 77–92, 2007.

[164] Salsburg, Z., Zwanzig, R., and Kirkwood, J., "Molecular distribution functions in a one-dimensional fluid," *J. Chem. Phys.*, vol. 21, pp. 1098–1107, 1953.

[165] Sanders, S. A. and Panagiotopoulos, A. Z., "Micellization behavior of coarse grained surfactant models," *J. Chem. Phys.*, vol. 132, no. 11, p. 114902, 2010.

[166] Santos, A. and Malijevskỳ, A., "Radial distribution function of penetrable sphere fluids to the second order in density," *Phys. Rev. E*, vol. 75, no. 2, p. 021201, 2007.

[167] Santos, A., "Class of consistent fundamental-measure free energies for hard-sphere mixtures," *Phys. Rev. E*, vol. 86, p. 040102(R), 2012.

[168] Santos, A., Fantoni, R., and Giacometti, A., "Penetrable square-well fluids: Exact results in one dimension," *Phys. Rev. E*, vol. 77, p. 051206, 2008.

[169] Saunders, M. G. and Voth, G. A., "Coarse-graining methods for computational biology," *Annu. Rev. Biophys.*, vol. 42, no. 1, pp. 73–93, 2013.

[170] Schmidt, M. and Fuchs, M., "Penetrability in model colloid–polymer mixtures," *J. Chem. Phys.*, vol. 117, pp. 6308–6312, 2002.

[171] Skodje, R. T. and Davis, M. J., "Statistical rate theory for transient chemical species: classical lifetimes from periodic orbits," *Chem. Phys. Lett.*, vol. 175, no. 1, pp. 92 – 100, 1990.

[172] Skokos, C., "On the stability of periodic orbits of high dimensional autonomous Hamiltonian systems," *Physica D*, vol. 159, pp. 155 – 179, 2001.

[173] Stillinger, F., "Phase transitions in the Gaussian core system," *J. Chem. Phys.*, vol. 65, pp. 3968–3974, 1976.

[174] Stubbs, J. M. and Siepmann, J. I., "Aggregation in dilute solutions of 1-hexanol in n-hexane: a monte carlo simulation study," *J. Phys. Chem. B*, vol. 106, no. 15, pp. 3968–3978, 2002.

[175] Suh, S., Kim, C., Kim, S., and Santos, A., "Molecular dynamics simulation study of self-diffusion for penetrable-sphere model fluids," *Phys. Rev. E*, vol. 82, no. 5, p. 051202, 2010.

[176] Suh, S., Min, W., and MacElroy, J., "Simulation studies for porosity and specific surface area in the penetrable-concentric-shell model pore," *Bull. Korean Chem. Soc.*, vol. 20, no. 12, pp. 1521–1523, 1999.

[177] Sussman, B. J., Townsend, D., Ivanov, M. Y., and Stolow, A., "Dynamic stark control of photochemical processes," *Science*, vol. 314, no. 5797, pp. 278–281, 2006.

[178] Talbot, J., Tarjus, G., and Viot, P., "Equilibrium adsorption on a random site surface," *J. Phys. Chem. B*, vol. 112, no. 41, pp. 13051–13058, 2008.

[179] Teramoto, H. and Sasa, S., "Microscopic description of the equality between violation of fluctuation-dissipation relation and energy dissipation," *Phys. Rev. E*, vol. 72, p. 060102, 2005.

[180] Teramoto, H., Toda, M., and Komatsuzaki, T., "Dynamical switching of a reaction coordinate to carry the system through to a different product state at high energies," *Phys. Rev. Lett.*, vol. 106, p. 054101, 2011.

[181] Tonks, L., "The complete equation of state of one, two and three-dimensional gases of hard elastic spheres," *Phys. Rev.*, vol. 50, no. 10, pp. 955–963, 1936.

[182] Torquato, S., Lu, B., and Rubinstein, J., "Nearest-neighbor distribution functions in many-body systems," *Phys. Rev. A*, vol. 41, no. 4, pp. 2059–2075, 1990.

[183] Torquato, S. and Stell, G., "Microstructure of two-phase random media. III. The n-point matrix probability functions for fully penetrable spheres," *J. Chem. Phys.*, vol. 79, pp. 1505–1510, 1983.

[184] Torquato, S. and Stell, G., "Microstructure of two-phase random media. IV. Expected surface area of a dispersion of penetrable spheres and its characteristic function," *J. Chem. Phys.*, vol. 80, pp. 878–880, 1984.

[185] Torquato, S., Uche, O. U., and Stillinger, F. H., "Random sequential addition of hard spheres in high euclidean dimensions," *Phys. Rev. E*, vol. 74, p. 061308, 2006.

[186] Torquato, S., *Random Heterogenous Materials: Microstructure and Macroscopic Properties*. New York: Springer-Verlag, 2002.

[187] Traversa, F. L., Di Ventra, M., and Bonani, F., "Generalized Floquet theory: Application to dynamical systems with memory and Bloch's theorem for nonlocal potentials," *Phys. Rev. Lett.*, vol. 110, p. 170602, 2013.

[188] Truhlar, D. G. and Garrett, B. C., "Variational transition state theory," *Annu. Rev. Phys. Chem.*, vol. 35, pp. 159–189, 1984.

[189] Truhlar, D. G., Hase, W. L., and Hynes, J. T., "Current status of transition–state theory," *J. Phys. Chem.*, vol. 87, pp. 2664–2682, 1983.

[190] Truhlar, D. G. and Garrett, B. C., "Multidimensional transition state theory and the validity of grotehynes theory," *J. Phys. Chem. B*, vol. 104, no. 5, pp. 1069–1072, 2000.

[191] Truhlar, D. G., Garrett, B. C., and Klippenstein, S. J., "Current status of transition-state theory," *J. Phys. Chem.*, vol. 100, pp. 12771–12800, 1996.

[192] Tucker, A. K. and Hernandez, R., "Diffusion of a spherical probe through static nematogens: Effect of increasing geometric anisotropy and long-range structure," *J. Phys. Chem. B*, vol. 116, pp. 1328–1334, 2012.

[193] Uzer, T., Jaffé, C., Palacián, J., Yanguas, P., and Wiggins, S., "The geometry of reaction dynamics," *Nonlinearity*, vol. 15, no. 4, p. 957, 2002.

[194] Van Hove, L., "Sur l'integrale de configuration pour les systemes de particules a une dimension," *Physica*, vol. 16, no. 2, pp. 137–143, 1950.

[195] Vavro, J., "Exact solution for the lattice gas model in one dimension," *Phys. Rev. E*, vol. 63, p. 057104, 2001.

[196] Vega, C. and Noya, E. G., "Revisiting the Frenkel-Ladd method to compute the free energy of solids: The Einstein molecule approach," *J. Chem. Phys.*, vol. 127, no. 15, p. 154113, 2007.

[197] Vicario, J., Eelkema, R., Browne, W. R., Meetsma, A., La Crois, R. M., and Feringa, B. L., "Catalytic molecular motors: fuelling autonomous movement by a surface bound synthetic manganese catalase," *Chem. Comm.*, pp. 3936–3938, 2005.

[198] Viererblová, L., Kolafa, J., Labík, S., and Malijevskỳ, A., "Virial coefficients and equation of state of the penetrable sphere model," *Phys. Chem. Chem. Phys.*, vol. 12, no. 1, pp. 254–262, 2010.

[199] Waalkens, H. and Wiggins, S., "Direct construction of a dividing surface of minimal flux for multi-degree-of-freedom systems that cannot be recrossed," *J. Phys. A*, vol. 37, no. 35, pp. L435–L445, 2004.

[200] Waalkens, H., Schubert, R., and Wiggins, S., "Wigner's dynamical transition state theory in phase space: classical and quantum," *Nonlinearity*, vol. 21, no. 1, p. R1, 2008.

[201] Wang, Q., "Studying soft matter with "soft" potentials: Fast lattice monte carlo simulations and corresponding lattice self-consistent field calculations," *Soft Matter*, vol. 5, pp. 4564–4567, 2009.

[202] Wang, Q., "Theory and simulation of the self-assembly of rod-coil block copolymer melts: Recent progress," *Soft Matter*, vol. 7, pp. 3711–3716, 2011.

[203] Widom, B., "Random sequential addition of hard spheres to a volume," *J. Chem. Phys.*, vol. 44, no. 10, pp. 3888–3894, 1966.

[204] Widom, B., "Geometrical aspects of the penetrable-sphere model," *J. Chem. Phys.*, vol. 54, pp. 3950–3957, 1971.

[205] Wilding, N. B. and Sollich, P., "Demixing cascades in cluster crystals," *J. Chem. Phys.*, vol. 141, no. 9, p. 094903, 2014.

[206] Yamanouchi, K., "The next frontier," *Science*, vol. 295, no. 5560, pp. 1659–1660, 2002.

[207] Yilmaz, M. B. and Zimmermann, F. M., "Exact cluster size distribution in the one-dimensional Ising model," *Phys. Rev. E*, vol. 71, p. 026127, 2005.

[208] Zachary, C., Stillinger, F., and Torquato, S., "Gaussian core model phase diagram and pair correlations in high Euclidean dimensions," *J. Chem. Phys.*, vol. 128, p. 224505, 2008.

[209] Zazza, C., Mancini, G., Brancato, G., and Barone, V., "In silico study of molecular-engineered nanodevices: A lockable light-driven motor in dichloromethane solution," *J. Phys. Chem. Lett.*, vol. 4, no. 22, pp. 3885–3890, 2013.

[210] Zhang, K. and Charbonneau, P., "[N]pT Monte Carlo simulations of the cluster-crystal-forming penetrable sphere model," *J. Chem. Phys.*, vol. 136, no. 21, p. 214106, 2012.